

Test experiments for the indirect determination of the
oxygen-15 and alpha radiative capture reaction rate in Type I
X-ray bursts.

Philip Adsley

Thesis submitted for the degree of Doctor of Philosophy

University of York

Department of Physics

September 2013

Abstract

This thesis discusses three test experiments for the indirect determination of the $^{15}\text{O}(\alpha,\gamma)^{19}\text{Ne}$ reaction rate, which influences the behaviour of Type I X-ray bursts.

The first experiment is a study of using silicon and germanium arrays to perform coincidence studies of the $^{15}\text{O}(^6\text{Li},d)^{19}\text{Ne}$ reaction in order to calculate the unknown α branching ratios or widths of the astrophysically important states. The test experiment uncovered serious problems with the data acquisition system which must be remedied before the experiment can be performed, as well as problems with the design of the experiment, for which mitigating changes have been proposed.

The second experiment was a study of the feasibility of using neon-implanted targets to deduce unknown spins of states in ^{19}Ne . Based on the results from this study, this experiment is not feasible due to the reactions from the target host material for the implanted targets.

Finally, a $^{27}\text{Al}(p,p')^{27}\text{Al}$ experiment has been performed using the Orsay Enge magnetic spectrometer with silicon detectors mounted in the target chamber. A preliminary analysis of the data which were taken during the experiment suggest that this system can be used for measuring the unknown α branching ratios for the astrophysically important states in ^{19}Ne using the $^{19}\text{F}(^3\text{He},t)^{19}\text{Ne}(\alpha)^{15}\text{O}$ reaction.

Contents

1	Astrophysical Motivation	2
1.1	Introduction	2
1.2	Stellar evolution	2
1.2.1	Protostar formation	3
1.2.2	Hydrostatic hydrogen burning	3
1.2.3	The end of hydrogen burning, helium burning and red giant formation	7
1.2.4	The 3α process	8
1.2.5	Supernovae and neutron stars	8
1.3	The X-Ray burst binary system	9
1.4	Thermonuclear burning in X-ray bursts	9
1.4.1	Pre-burst burning	9
1.4.2	Breakout from the CNO cycles	10
1.4.3	Post-breakout behaviour	11
1.5	Observation of X-ray bursts and connection to nuclear physics input	12
1.6	The present work	14
2	Theory	16
2.1	Introduction	16
2.2	Cross sections	16
2.3	Resonances	17
2.4	Thermonuclear reaction rates	18
2.4.1	Penetrability	20
2.4.2	The Gamow Window and direct measurements	22
2.4.3	Resonant reactions	22
2.5	Nuclear reactions	26
2.5.1	Direct reactions and the DWBA	26
2.5.2	Relating the spectroscopic factor and the DWBA cross section	27
3	The $^{15}\text{O}(\alpha,\gamma)^{19}\text{Ne}$ Reaction and Indirect Studies	29
3.1	Introduction	29

3.2	States in ^{19}Ne relevant to the $^{15}\text{O}(\alpha,\gamma)^{19}\text{Ne}$ reaction rate	30
3.3	Structural information	30
3.4	Evaluating previous studies and prior information	33
3.4.1	Total widths	33
3.4.2	Spin-parities	34
3.4.3	α -particle spectroscopic factors	34
3.4.4	α -particle branching ratios	34
3.4.5	Relative influence of the astrophysical states	37
3.5	The planned $^{15}\text{O}(^6\text{Li},d)^{19}\text{Ne}$ study with SHARC/TIGRESS	38
3.6	Studying the J^π s of resonances in ^{19}Ne using the $^{20}\text{Ne}(d,t)^{19}\text{Ne}$ reaction	39
3.7	Direct measurement of the α -particle branching ratios	39
4	The SHARC/TIGRESS Setup	41
4.1	Introduction	41
4.2	TRIUMF-ISAC and radioactive ion beam production	41
4.3	Semiconductors as detectors	43
4.4	Scintillators as detectors	44
4.5	SHARC	45
4.5.1	Silicon detectors	45
4.5.2	The array	49
4.5.3	Instrumentation: preamplifiers and DAQ modules	53
4.5.4	Particle identification using differential energy loss	53
4.6	γ -ray interactions	54
4.7	TIGRESS	56
4.7.1	TIGRESS detectors	58
4.7.2	Add-back	59
4.7.3	Suppressors	59
4.7.4	Instrumentation: preamplifiers and DAQ modules	60
4.8	The TIGRESS DAQ	60
4.8.1	Constant fraction discrimination	61
4.8.2	Output MIDAS files	62
5	Data analysis of the $^{20}\text{Na} + ^6\text{Li}$ experiment	65
5.1	Introduction	65
5.2	MIDAS to ROOT conversion	66
5.3	‘Event’ to ‘Particle’ conversion	66
5.3.1	SHARC events	67
5.3.2	TIGRESS events	67

5.4	Calibration	68
5.4.1	SHARC	68
5.4.2	TIGRESS	70
5.5	Timing information	70
5.5.1	SHARC timing information	72
5.5.2	TIGRESS timing information	73
5.6	Testing the reconstruction: writing the analysis code and identifying reac- tion channels	77
5.6.1	Effective thickness correction	78
5.6.2	Doppler correction	80
5.7	Fusion evaporation products	81
5.8	$^{20}\text{Na}(p,p')^{20}\text{Na}^*$	84
5.9	$^{20}\text{Na}(^6\text{Li},d)^{24}\text{Al}^*(p)^{23}\text{Mg}$	85
6	Readiness for the $^{15}\text{O}(^6\text{Li},d)^{19}\text{Ne}$ experiment	89
6.1	Reconstruction of event fragments, construction of a sort code and future requirements	89
6.2	Pad calibration	90
6.3	Technical problems - preamplifiers and timing	90
6.4	Fusion-evaporation	90
7	A test study of the $^{20}\text{Ne}(d,t)^{19}\text{Ne}$ reaction at the Munich Q3D spectrom- eter facility	94
7.1	Introduction	94
7.2	The targets	95
7.3	Beam production	96
7.4	The Munich Q3D	96
7.4.1	Magnetic spectrometers	96
7.4.2	Focal-plane detectors	97
7.5	Taking data	98
7.5.1	Data acquisition	100
7.6	Processing the data	102
7.6.1	Calibrating the focal plane	102
7.6.2	Identifying Reaction Products and States	103
8	Discussion of the Munich tests	108
8.1	Introduction	108
8.2	Contaminant peaks	108
8.3	Neon leakage from the target	109
8.4	Possible solutions	109

8.4.1	Targets	110
8.4.2	(d,t) vs. $({}^3\text{He},{}^4\text{He})$	110
9	Measuring branching ratios using coincidences between the Orsay Enge spectrometer and silicon detectors	112
9.1	Introduction	112
9.2	Astrophysical Background	113
9.3	Experimental outline and apparatus	114
9.3.1	The Orsay Enge magnetic spectrometer	114
9.3.2	Focal plane detectors	116
9.3.3	Silicon detectors	118
9.3.4	Data acquisition	118
9.4	Data Analysis	120
9.4.1	Focal plane singles spectrum	120
9.4.2	Spectrometer-silicon coincidence spectra	121
9.4.3	Preliminary results	123
9.5	Summary and applicability to ${}^{19}\text{F}({}^3\text{He},t){}^{19}\text{Ne}^*(\alpha){}^{15}\text{O}$	125
10	Conclusions	131
A	Evaluation of the Gamow Factor integral	133
B	The Orsay system efficiency	135
B.1	Angular distribution of reaction products	135
B.2	Reaction products and impact on silicon detectors	136

List of Figures

1.1	The pp chains. Stable nuclides are shaded.	4
1.2	The CNO cycles.	5
1.3	The HCNO cycles.	6
1.4	Breakout Path 1, $^{15}\text{O}(\alpha,\gamma)^{19}\text{Ne}(p,\gamma)^{20}\text{Na}$	10
1.5	Breakout Path 2, $^{14}\text{O}(\alpha,p)^{17}\text{F}(p,\gamma)^{18}\text{Ne}(\alpha,p)^{21}\text{Na}$	11
2.1	Probability distribution for energy at $T_9 = 1$	23
2.2	Penetration through a potential barrier.	24
2.3	The Gamow Window for $^{15}\text{O}(\alpha,\gamma)^{19}\text{Ne}$ at $T_9 = 1$	25
2.4	Plot of qR to demonstrate the effect of bombarding particle on the ℓ -values	28
3.1	^{19}Ne level scheme above the α -threshold.	31
3.2	Simplified shell-model configurations for $^{19}\text{Ne}(4033 \text{ keV})$ and $^{15}\text{O}(\text{ground state})$	32
4.1	Schematic of TRIUMF-ISAC	42
4.2	A diagram of a MSX-35 detector	48
4.3	A diagram of a BB11 detector	48
4.4	A diagram of a QQQ1 detector	49
4.5	A diagram showing four QQQ2 detectors	50
4.6	SHARC schematic	51
4.7	Compton Scattering	55
4.8	The North hemisphere of TIGRESS in high-efficiency mode.	56
4.9	Close-up of the North hemisphere of TIGRESS in high-efficiency mode.	57
4.10	A TIGRESS Clover	58
4.11	DAQ setup diagram	62
4.12	Schematic diagrams of CFD algorithms	63
5.1	Ribbon cable pin arrangement on BB11 detectors	69
5.2	BB11 calibration - crosstalk correction	71
5.3	δCFD spectrum for one pixel	73
5.4	Plots showing systematic effects in silicon timing values	74

5.5	CFD values for all TIGRESS cores	75
5.6	CFD values for a single TIGRESS core	75
5.7	CFD values for all BGO suppressors	76
5.8	CFD values for SHARC detector upstream box 2, front strip 12.	76
5.9	$dE - E$ UBx2 Uncorrected with strip detector energy cut-off at 6 MeV	79
5.10	$dE - E$ UBx2 with a proton correction and strip energy detector cut-off at 6 MeV	79
5.11	Diagram showing the geometry for the Doppler correction	80
5.12	Doppler-correction γ -ray spectrum for mass 38 a.m.u	82
5.13	Doppler-correction γ -ray spectrum for mass 37 a.m.u	82
5.14	Doppler-correction γ -ray spectrum for mass 35 a.m.u	83
5.15	Doppler-correction γ -ray spectrum for mass 34 a.m.u	83
5.16	Doppler-correction γ -ray spectrum for mass 31 a.m.u	84
5.17	Doppler-corrected γ -ray spectrum gated on protons in the downstream box	85
5.18	Doppler-corrected γ -ray spectrum gated on protons in the downstream box and the 600-keV transition.	86
5.19	Figures showing the effect of gating on the 600-keV γ -ray transition on the particle spectrum.	87
5.20	γ -ray spectrum gated on deuterons in the upstream box detector	88
6.1	Raw γ -ray spectrum from beam data.	91
6.2	Deuteron angle vs. recoil angle for $^{15}\text{O}(^6\text{Li},d)^{19}\text{Ne}$ at 5 MeV/u	92
6.3	Diagram of the suggested new SHARC/TIGRESS experiment	93
7.1	Schematic of the Munich Q3D	97
7.2	Q3D focal plane detectors	98
7.3	Q3D MWPC Diagram	99
7.4	Q3D focal plane mode of operation	99
7.5	Rigidities for various states at various angles. The relative movement of the states from reactions involving different mass nuclides can clearly be seen.	101
7.6	First anode charge against second anode charge for particle identification.	103
7.7	Anode charge against plastic scintillator charge for particle identification.	104
7.8	10° focal plane spectrum	104
7.9	12° focal plane spectrum	105
7.10	15° focal plane spectrum	105
7.11	25° focal plane spectrum	106
7.12	35° focal plane spectrum	106
7.13	Position against anode charge for 12° showing leakage through particle identification gates.	107

8.1	DWBA angular distributions of $7/2^-$ and $9/2^-$ states in ^{19}Ne	109
8.2	Plot of qR to demonstrate the effect of bombarding particle on the ℓ -values	111
9.1	Energy levels for the $^{27}\text{Al}(p,p')^{27}\text{Al}$ experiment.	115
9.2	The Orsay experimental setup.	116
9.3	An Enge magnetic spectrometer	117
9.4	Orsay laboratory angle coverage.	119
9.5	Plots of $B\rho$ from the Orsay Enge spectrometer.	122
9.6	δTDC for focal plane plus silicon coincidence events.	123
9.7	Silicon energy against $B\rho$ for coincidence events.	124
9.8	Focal plane spectra for gates on coincidence events	125
9.9	The effect of detector thickness on background	128

List of Tables

1.1	The pp chains.	4
1.2	The CNO Cycles.	5
1.3	The Hot CNO Cycles.	6
3.1	Lifetimes of states in ^{19}Ne	34
3.2	Transition strengths and branching ratios of the doublet states in ^{19}F and ^{19}Ne	35
3.3	Previous measurements of α -particle branching ratios in ^{19}Ne	37
4.1	SHARC Detector Particulars	46
4.2	SHARC Detectors used. The upstream CD was a single layer of segmented QQQ2s so there are no corresponding pads to these detectors.	52
5.1	α -decay energies and intensities	69
7.1	^{20}Ne -implanted targets available during the experiment. All target backings were ^{12}C apart from the Seattle target which was $^{\text{nat}}\text{C}$	95
7.2	Energies, J^π and ℓ -values for relevant states in ^{19}Ne , ^{15}O and ^{11}C	100
9.1	Peak positions and heights for the Orsay data	126

Acknowledgements

With your permission, the author will use the first-person personal pronoun for the rest of these acknowledgements. We did consider the majestic plural but we felt that that was grandiloquent.

There is a danger that the acknowledgements in a thesis can expand to about the same length as the rest of the thesis. I shall endeavour to avoid that. Expect no profound sentiment or eloquent language, I've saved that for the analysis chapters.

Professor Brian Fulton and Dr. Christian Diget have provided me over the course of my Ph.D. with much sage advice (including informing me, repeatedly, of those subjects and occasions where I was entirely wrong). If I have managed to retain even a small fraction of what they have taught me during my Ph.D., then I am a lucky man.

A number of other physicists from various facilities have also been generous with their time explaining data acquisition systems, analysis techniques, experimental apparatuses and physics to me. My 'darling' 'wife' Kelly Chipps, Simon Fox, Alison Laird, Paul Davies, Anuj Parikh, Greg Hackman, Adam Garnsworthy, Scott Williams, Nicolas de Sereville and Iulian Stefan are all owed a huge 'thank you' and a few pints. In particular, I would thank Ben Kay for the time he spent working with me on analysing the data from Munich, and for pushing me towards applying for postdoc positions and giving me assistance in doing so.

Ulrike Hager wrote the TigSort code used for the SHARC/TIGRESS event reconstruction and was patient enough with my flailing around to enable me to diagnose the problems with the TIGRESS DAQ. If it weren't for her, I would probably still be trying to write the reconstruction code now. Seriously, now. If you're reading this (unlikely) in 2025, I'd still be there plugging away.

Fellow students at York and elsewhere, both graduate and undergraduate, have kept me (relatively) sane at various points. I owe a great debt to James Smallcombe for not murdering me when I managed to reduce the office to a total pigsty and then for putting up with that for four years, as well as his numerous enforced breaks when I was losing my mind. His contributions to my work over the years have been numerous and insightful. Matt and Su have spent the last year of my Ph.D. making sure that I ate properly (like I had obviously been doing during my first three years...) while proof reading every document

thrust in their direction and giving me a place to sleep when I was just finishing. Jack and Tom (pub?) have put up with a large amount of complaining about my thesis with remarkable fortitude; even beyond that, their willingness to talk passionately about their own work made the process of writing this thesis much easier to bear. I should, at this point, also thank Anna for allowing me to steal her boyfriend so frequently for pub trips. Lianne has put up with numerous tasteless jokes (sorry...) and has provided much practical support which has often taken the form of telling me to shut up and get on with my work. Nic and Maryja deserve special thanks for gin and good conversation.

Special thanks go to Dr. Gemma Wilson who also wrote a thesis on SHARC/TIGRESS. Though a recent arrival at York, her advice, good taste in beer and proof reading skills arrived at an opportune time.

Thanks also to Miss Elizabeth Bennett for requesting to be in my thesis because she was 'sure the astronauts would LOVE it.'

The various clergy around York, Fathers Glyn, Rowan, David and Tony amongst others, have provided spiritual support during my time here. Their calm reminders that there are more important things than work have been vital during the last few years. The friendship of those whom I have met through the Minster has been greatly appreciated. In addition, I am thankful for the warm welcome I received at Christchurch Cathedral, Vancouver, when on placement at TRIUMF.

I'm writing this sitting in my bedroom back in Didcot on my parent's 40th wedding anniversary. Without them I would not be here at all, let alone finishing my thesis. To them, and my amazing sister Dr. Rosie Adsley, go much greater thanks than I could ever express. So I won't try.

We now return you to your regularly scheduled programme.

Declaration

This thesis is the work of Philip Adsley alone, apart from where private communications are noted in the text. None of the material in this thesis has been presented for examination previously.

Chapter 1

Astrophysical Motivation

Brevis esse laboro, obscurus fio.

In striving for brevity, I am
made obscure.

Horace - *Ars Poetica*

1.1 Introduction

This thesis discusses the determination of the $^{15}\text{O}(\alpha,\gamma)^{19}\text{Ne}$ reaction rate which is an important reaction in the energy production in Type-I X-ray bursts. Type I¹ X-ray bursts are characterised by large increases in the X-ray flux from neutron star binary systems. Grindlay *et al.* [2] and Belian *et al.* [3] both reported observations of these X-ray flashes in 1976; in the same year, Woosley and Taam [4] suggested that the bursts are caused by thermonuclear runaway in the layer of matter accreted from the companion star. Bursts typically last between tens and hundreds of seconds with temperatures ranging from 1 to 1.5 GK. It is unlikely, though not impossible [5], that X-ray bursts contribute to observed galactic isotopic abundances by ejecting matter during bursts as the gravitational fields from neutron stars are very strong. This leaves the lightcurve as the only realistic observable to probe the behaviour of the X-ray burst.

1.2 Stellar evolution

In order to discuss the behaviour of X-ray bursts, it is first necessary to briefly discuss the chain of events that lead up to the formation of neutron star binary systems, along with the

¹For completeness, Type I X-ray bursts are the astrophysical underpinning for this thesis. There are Type II X-ray bursts which are caused by a different mechanism: instabilities in the accretion disk in neutron star binary systems [1]. They are not a nuclear process and will be discussed no further.

thermonuclear processes which are responsible for energy generation and nucleosynthesis in stars.

Stellar evolution depends strongly on the initial mass of the star. For stars with $0.4M_{\odot} < M < 11M_{\odot}$, the end result of the stellar evolution is a red giant.² This occurs when the available hydrogen fuel in the core has been consumed. In this case, the onset of hydrogen burning in a shell around the helium-burning core causes a large increase in the radius of the star. This is described in section 1.2.3.

For stars of $M > 11M_{\odot}$, the end of stellar evolution is through a supernova. In this case, the compact object remnant can be a neutron star - an object supported by neutron degeneracy pressure. This process is described in more detail in section 1.2.5.

The main hydrogen burning processes are also discussed along with the 3α process which is responsible for the formation of ^{12}C in stars.

1.2.1 Protostar formation

The formation of stars starts with collapsing gas clouds, mainly formed of hydrogen and helium, in the interstellar medium. The gravitational potential energy liberated as the gas falls inwards is converted into kinetic motion of the gas (heat) and into radiation. When the clouds become dense enough, energy radiated away can no longer escape and is absorbed by the cloud, increasing the temperature of the gas. This process continues until the temperature becomes high enough to start deuterium burning ($^2\text{H}(p,\gamma)^3\text{He}$). This burning process generates more energy within the gas cloud. Between these processes and the gravitational potential energy released by the collapse, the temperature can eventually become high enough to start fusing hydrogen into helium. Energy generated by hydrogen burning will eventually cause the collapse of the gas cloud to stop, leaving the newly-formed star in hydrostatic equilibrium.

1.2.2 Hydrostatic hydrogen burning

The evolution of the star depends strongly on its mass and chemical composition. In the case of the X-ray burst binary system, only two scenarios are of direct interest: those which form red giants and those which form neutron stars.

For most of the life of stars, they burn protons into ^4He in their cores via the pp chains or the CNO cycles. The energy released in these processes allows the star to resist gravitational collapse.

The pp chains

Each conversion of four protons to a ^4He nucleus releases 26.731 MeV. There are no stable nuclei of mass 5 or 8, which prevents the pp chains from synthesising heavier nuclei. For

² M_{\odot} is the solar mass.

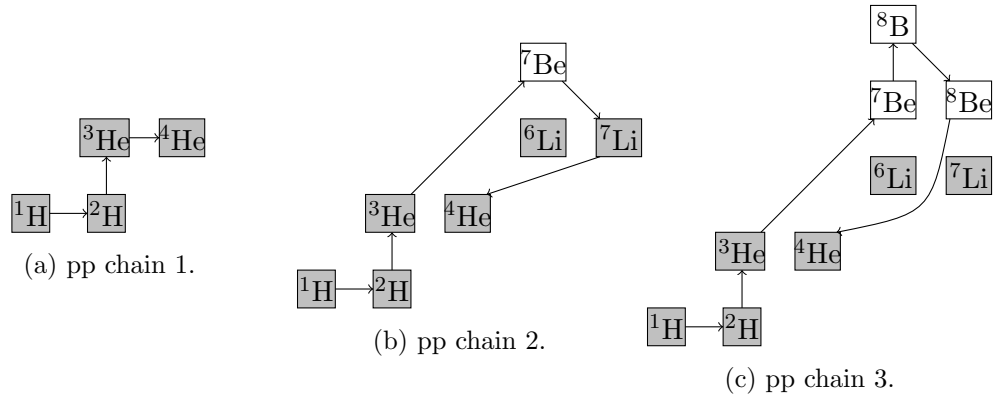


Figure 1.1: The pp chains. Stable nuclides are shaded.

lower mass stars, or ones without the heavier CNO seed required for the CNO cycles, the pp chains are the only possible hydrogen burning method. The reactions involved are slow meaning that the hydrogen fuel is only slowly consumed enabling stars to burn for millions of years or more, giving time for nucleosynthesis of heavier elements to take place leading to the possibility of life. The pp chains are shown in fig. 1.1 and the reaction sequences are set out in table 1.1.

pp1	pp2	pp3
$p(p, \beta^+ \nu)d$	$p(p, \beta^+ \nu)d$	$p(p, \beta^+ \nu)d$
$d(p, \gamma)^3\text{He}$	$d(p, \gamma)^3\text{He}$	$d(p, \gamma)^3\text{He}$
$^3\text{He}(^3\text{He}, 2p)\alpha$	$^3\text{He}(\alpha, \gamma)^7\text{Be}$	$^3\text{He}(\alpha, \gamma)^7\text{Be}$
	$^7\text{Be}(\beta^-, \nu)^7\text{Li}$	$^7\text{Be}(p, \gamma)^8\text{B}$
	$^7\text{Li}(p, \alpha)\alpha$	$^8\text{B}(\beta^+ \nu)^8\text{Be}$
		$^8\text{Be}(\alpha)\alpha$

Table 1.1: The pp chains.

The CNO cycles

The CNO cycles also convert hydrogen into helium. This is a catalytic process; in the simplest of the CNO cycles, the pre-existing ^{12}C seed produced in the 3α process (see section 1.2.4) is used as a seed in a series of proton captures and β^+ decays with the ^{12}C recovered in the final reaction in the cycle, $^{15}\text{N}(p, \alpha)^{12}\text{C}$. There are a number of different CNO cycles which are grouped into two main sets of reactions. These are the (Cold) CNO cycles and the Hot CNO (HCNO) cycles. The HCNO cycles, as their name would suggest, operate at higher temperatures ($T > 100$ MK compared to 10s of MK for the cold CNO

cycles), when proton capture reactions on certain nuclides become more likely than the β^+ decays of those nuclei. The CNO and HCNO cycles are shown in figs. 1.2 and 1.3 and in tables 1.2 and 1.3.

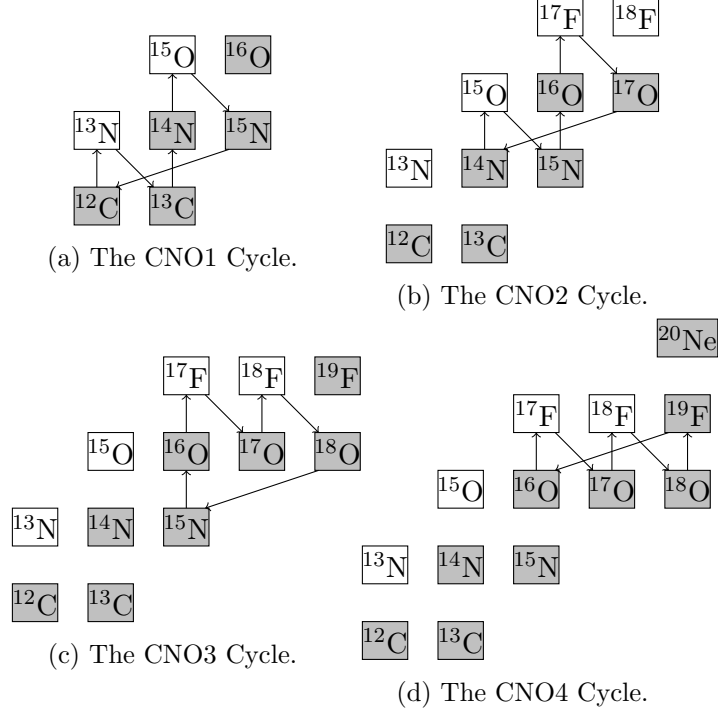


Figure 1.2: The CNO cycles. Stable nuclides are shaded.

CNO1	CNO2	CNO3	CNO4
$^{12}\text{C}(p, \gamma)^{13}\text{N}$	$^{14}\text{N}(p, \gamma)^{15}\text{O}$	$^{15}\text{N}(p, \gamma)^{16}\text{O}$	$^{16}\text{O}(p, \gamma)^{17}\text{F}$
$^{13}\text{N}(\beta^+ \nu)^{13}\text{C}$	$^{15}\text{O}(\beta^+ \nu)^{15}\text{N}$	$^{16}\text{O}(p, \gamma)^{17}\text{F}$	$^{17}\text{F}(\beta^+ \nu)^{17}\text{O}$
$^{13}\text{C}(p, \gamma)^{14}\text{N}$	$^{15}\text{N}(p, \gamma)^{16}\text{O}$	$^{17}\text{F}(\beta^+ \nu)^{17}\text{O}$	$^{17}\text{O}(p, \gamma)^{18}\text{F}$
$^{14}\text{N}(p, \gamma)^{15}\text{O}$	$^{16}\text{O}(p, \gamma)^{17}\text{F}$	$^{17}\text{O}(p, \gamma)^{18}\text{F}$	$^{18}\text{F}(\beta^+ \nu)^{18}\text{O}$
$^{15}\text{O}(\beta^+ \nu)^{15}\text{N}$	$^{17}\text{F}(\beta^+ \nu)^{17}\text{O}$	$^{18}\text{F}(\beta^+ \nu)^{18}\text{O}$	$^{18}\text{O}(p, \gamma)^{19}\text{F}$
$^{15}\text{N}(p, \alpha)^{12}\text{C}$	$^{17}\text{O}(p, \alpha)^{14}\text{N}$	$^{18}\text{O}(p, \alpha)^{15}\text{N}$	$^{19}\text{F}(p, \alpha)^{16}\text{O}$

Table 1.2: The CNO Cycles.

In reality, the CNO cycles form a network where material can move between cycles at branching points. For example, the $^{15}\text{N}(p, \gamma)^{16}\text{O}$ reaction, leading into the second CNO cycle, competes with the $^{15}\text{N}(p, \alpha)^{12}\text{C}$ reaction, feeding back into the first CNO cycle.

The overall rate of the cycle is determined by the rate of the slowest step. Matter involved in stellar reaction networks tends to become concentrated at those nuclides

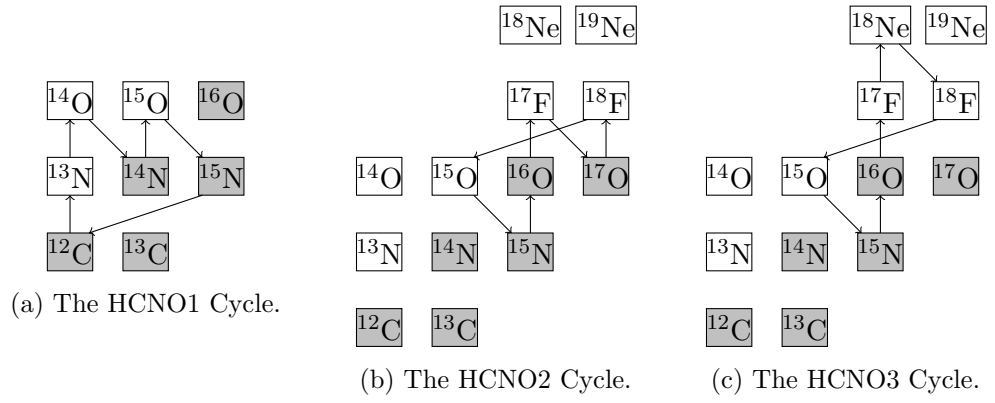
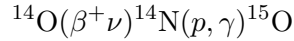


Figure 1.3: The HCNO cycles. Stable nuclides are shaded.

HCNO1	HCNO2	HCNO3
$^{12}\text{C}(p, \gamma)^{13}\text{N}$	$^{15}\text{O}(\beta^+ \nu)^{15}\text{N}$	$^{15}\text{O}(\beta^+ \nu)^{15}\text{N}$
$^{13}\text{N}(p, \gamma)^{14}\text{O}$	$^{15}\text{N}(p, \gamma)^{16}\text{O}$	$^{15}\text{N}(p, \gamma)^{16}\text{O}$
$^{14}\text{O}(\beta^+ \nu)^{14}\text{N}$	$^{16}\text{O}(p, \gamma)^{17}\text{F}$	$^{16}\text{O}(p, \gamma)^{17}\text{F}$
$^{14}\text{N}(p, \gamma)^{15}\text{O}$	$^{17}\text{F}(\beta^+ \nu)^{17}\text{O}$	$^{17}\text{F}(p, \gamma)^{18}\text{Ne}$
$^{15}\text{O}(\beta^+ \nu)^{15}\text{N}$	$^{17}\text{O}(p, \gamma)^{18}\text{F}$	$^{18}\text{Ne}(\beta^+ \nu)^{18}\text{F}$
$^{15}\text{N}(p, \alpha)^{12}\text{C}$	$^{18}\text{F}(p, \alpha)^{15}\text{O}$	$^{18}\text{F}(p, \alpha)^{15}\text{O}$

Table 1.3: The Hot CNO Cycles.

for which the destructive reactions are slowest, these nuclides are known as the ‘waiting points’. Taking ^{14}O ($t_{1/2} = 70.6$ s) as an example, the relatively slow β -decay means that it takes a long time for ^{14}O to convert to ^{15}O via:



Meanwhile the $^{14}\text{O}(p,\gamma)^{15}\text{F}$ reaction is blocked as the ground state of ^{15}F is unbound [6]. Therefore, until the $^{14}\text{O}(\alpha,p)^{17}\text{F}$ reaction becomes significant, which requires much higher temperatures to offset the larger Coulomb barrier (see section 1.4.2), the only route out of the ^{14}O waiting point is via β -decay.

An important distinction between the CNO and HCNO cycles exists: the CNO cycles are limited by the rates of some proton-induced reactions while the HCNO cycles are limited by β -decay lifetimes. This means that, while the CNO cycles show strong temperature dependence, the HCNO cycles do not. Increases in temperature can increase proton-induced reaction rates (and thus energy generation from the CNO cycles) while leaving β -decay lifetimes unchanged (leaving HCNO energy generation unchanged). At higher temperatures, the energy generation from the HCNO cycles cannot increase with increasing temperature - this suggests that any explosive behaviour which requires a large increase in the energy generation requires other processes outside the HCNO cycles.³

1.2.3 The end of hydrogen burning, helium burning and red giant formation

Once the hydrogen in the core has been consumed, hydrogen burning continues in a shell around the core. The core starts to contract as the energy source resisting gravity has been removed; this contraction causes a rise in the temperature of the hydrogen burning shell around the core, increasing the energy generation from this shell. The extra energy produced causes the surface to expand, transforming the star into a red giant. The outer layers of this star will be rich in hydrogen and helium. The core of the star mainly consists of helium; depending on the mass of the star, the core may collapse to an electron degenerate state until the onset of helium burning in the core, which lifts the degeneracy in a thermonuclear runaway event. More massive stars ($2M_{\odot} < M < 4M_{\odot}$) will have helium ignite quiescently in the core, preventing electron degeneracy occurring. After this point there is a complex series of burning stages and dredge-ups which cause mass loss via stellar winds resulting in a CO or ONe white dwarf remnant, depending on the initial mass of the star.

³This is somewhat simplistic - it is possible to increase energy generation when a new HCNO begins to operate and when the $^{14}\text{O}(\alpha,p)^{17}\text{F}$ reaction begins to operate and bypass the decay of ^{14}O . However, in these cases, the maximum energy generation without leaving the HCNO cycles is still limited.

1.2.4 The 3α process

The pp chains cannot synthesise heavier elements; in order to explain the production of heavier elements, therefore, new mechanisms of nucleosynthesis must be proposed. The 3α process represents one of the greatest triumphs of nuclear astrophysics. Hoyle suggested a production mechanism for ^{12}C which involves a small equilibrium abundance of the unbound ^8Be nucleus being formed by two ^4He nuclei colliding in stars [7]. A third ^4He nucleus could then collide with the ^8Be and form an excited state of ^{12}C [8]. Hoyle suggested that this would require a wide s -wave or d -wave resonance at around 7 MeV in ^{12}C . This predicted state, called for obvious reasons the ‘Hoyle State’, was then observed [9, 10]. The 3α reaction, though slow, represents a vital stage in the formation of all elements more massive than carbon. The Hoyle State is at a low excitation energy relative to the $^8\text{Be}+\alpha$ system and will dominate the reaction rate at most temperatures. While the Hoyle state is thought to dominate the 3α process at lower temperatures, higher-lying resonances could have a large influence on the reaction rate. For example, if there exists a 2^+ rotational state built on the 0^+ Hoyle state (the attempted observation of which has been the subject of much effort, see Refs. [11, 12] and references therein) then the 3α reaction rate could be increased by a large amount at higher temperatures; a factor of 10 is suggested by Fynbo *et al.* [13].

1.2.5 Supernovae and neutron stars

For massive stars ($M > 11M_{\odot}$), helium burning is not the final thermonuclear process in the evolution of the star as it was for the red giants in section 1.2.3. Rather, after helium burning has finished, carbon, neon, oxygen and silicon burning can take place. These convert the CNO material in the star into iron peak nuclei. Once the core is composed mainly of iron peak nuclides, no more energy can be produced in it from thermonuclear processes.

The core of the massive star is, as was the case for the red giant after the onset of carbon burning, supported in part by electron degeneracy pressure. However, the core is too massive ($M > 1.4M_{\odot}$ [14]) to be fully supported by electron degeneracy pressure; this results in the core collapsing. At this point, electron-capture reactions start on the iron peak nuclei in the core. These electron-capture reactions can take place because the degeneracy energy for the electrons is higher than the mass difference between neutrons and protons, making the inverse β -decay process energetically favourable. Neutron decay is then blocked as the electrons have filled up all of the available states leaving no free states for the electron formed in the decay. Core collapse continues until the core reaches nuclear densities at which point the infalling matter ‘bounces’. The shockwave which results removes the outer layers of the massive star leaving a remnant core supported by neutron degeneracy pressure - a neutron star.

1.3 The X-Ray burst binary system

X-ray bursts take place in a binary system consisting of a red giant star and a neutron star. The red giants discussed in section 1.2.3 are large stars with loosely-bound H/He-rich outer layers. For systems where the neutron star and the red giant are close, the intense gravitational field of the neutron star can result in matter transfer from the red giant. If the neutron star has strong magnetic fields, the matter is channelled along the field lines onto the magnetic poles. This results in hotspots on the surface of the neutron star which give a constant X-ray flux from specific points on the neutron star, observable as a pulsar. For neutron stars with weak magnetic fields, the infalling matter is not longer channelled along the field lines. In this case, it forms an accretion disk from which matter slowly accretes onto the surface. A constant flux of X-rays is also created in this case; however, as the infalling matter is no longer being channelled along magnetic field lines, there are no hotspots of X-ray flux as in the case of highly-magnetised neutron stars. The infalling matter is rich in hydrogen and helium and forms an electron-degenerate atmosphere on the surface of the neutron star. Thermonuclear reactions in the atmosphere cause the temperature of the atmosphere to rise until reaction rates rise high enough to cause thermonuclear runaway. The processes causing this bursting behaviour are described in detail in the next section.

1.4 Thermonuclear burning in X-ray bursts

In section 2.4, the theory of thermonuclear reactions is discussed. In this section, the nuclear reactions of importance at the different stages of X-ray bursts are introduced. There are three distinct phases in the X-ray burst. The first is the operation of the CNO cycles in the atmosphere of the neutron star that starts energy production; the second is the breakout from the CNO cycles which enables a large increase in the energy production rate; and the third is a series of rapid proton captures that consumes the hydrogen available in the burst.

1.4.1 Pre-burst burning

The H- and He-rich matter falling onto the neutron star from the companion star forms an electron-degenerate atmosphere. The temperature and density of the atmosphere is high enough for CNO burning cycles to take place (see section 1.2.2). The energy generated causes the atmosphere to heat; usually this would cause expansion of the atmosphere and cooling but as the matter is electron degenerate this mechanism, which usually limits the thermonuclear energy generation rate, does not occur. At this point, the atmosphere is composed of around 73% ^1H , 25% ^4He with small amounts of the waiting point nuclei ^{14}O and ^{15}O .

The infalling matter will not necessarily be rich in the CNO seed required for this burning process to take place. However, the high densities and temperatures in the atmosphere of the neutron star can cause the 3α process to start, converting ^4He into ^{12}C . The energy generation rate is sensitive to the mass fraction of CNO seed nuclei [15]. Therefore, the initial abundance of the infalling matter from the low-mass companion can strongly influence the subsequent behaviour of the burst. The initial abundance can be modified by the inclusion of the ashes of previous bursts.

1.4.2 Breakout from the CNO cycles

The X-ray burst has by this point established CNO burning; the energy produced causes the temperature to rise. In order to achieve the large increase in energy generation seen in X-ray bursts, the system must break out of the CNO cycles and into some new burning regime. Breakout from the Hot CNO cycles is limited; the waiting points of ^{14}O , ^{15}O and ^{18}Ne exist because the proton radiative captures onto these nuclei are to ^{15}F [6], ^{16}F [16] and ^{19}Na [17] respectively which are all unbound to proton decay.⁴ Therefore, in order to break out of the CNO cycles, these nuclides must be bypassed. α -induced reactions provide a mechanism for doing this. The Coulomb barrier for these reactions is obviously much higher than the barrier for proton-induced reactions and the reactions will only take place at higher temperatures. The first sequence for breaking out of the CNO cycles is shown in fig. 1.4.

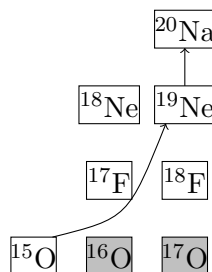


Figure 1.4: Breakout Path 1, $^{15}\text{O}(\alpha,\gamma)^{19}\text{Ne}(p,\gamma)^{20}\text{Na}$

The first reaction in the breakout path, $^{15}\text{O}(\alpha,\gamma)^{19}\text{Ne}$, will be the slower of the two stages and will control the rate at which material is processed through this breakout path. Iliadis [15] compares the β^+ -decay half-life of ^{15}O (122.24 s) to the half-life of ^{15}O from the $^{15}\text{O}(\alpha,\gamma)^{19}\text{Ne}$ reaction at a density of 10^4 g/cm³, finding that at $T \approx 0.5$ GK the half-life to α radiative capture becomes shorter than the positron decay half-life. If the rate used is correct, it can be assumed that above this temperature the α -capture reaction dominates over the decay, and most ^{15}O is processed out of the CNO cycles. However, the $^{15}\text{O}(\alpha,\gamma)^{19}\text{Ne}$ reaction has never been experimentally measured; there have

⁴Two-proton capture reactions have been considered and largely discounted as alternative breakout paths.

been a number of estimated rates based on known nuclear parameters. There remain considerable uncertainties in the reaction rate due to the large uncertainties in some of the important resonance parameters. This will be discussed in more detail in chapter 3.

The other main breakout path is shown in fig. 1.5:

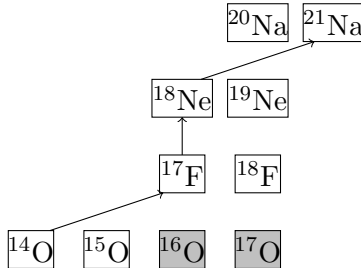


Figure 1.5: Breakout Path 2, $^{14}\text{O}(\alpha,p)^{17}\text{F}(p,\gamma)^{18}\text{Ne}(\alpha,p)^{21}\text{Na}$

In this reaction, the $^{14}\text{O}(\alpha,p)^{17}\text{F}$ reaction dominates over β^+ -decay from $T \approx 0.4$ GK, but the $^{18}\text{Ne}(\alpha,p)^{21}\text{Na}$ reaction does not dominate over β^+ -decay until $T \approx 0.8$ GK. However, the additional processing of material by the $^{14}\text{O}(\alpha,p)^{17}\text{F}$ reaction results in a higher abundance of ^{15}O , increasing the probability of breakout via the $^{15}\text{O}(\alpha,\gamma)^{19}\text{Ne}$ reaction. Once the $^{14}\text{O}(\alpha,p)^{17}\text{F}$ becomes strong, the ^{18}Ne abundance would be expected to rise until the temperature is high enough for it to be destroyed. Neither of the three α -induced reaction rates has been directly measured and, as in the case for $^{15}\text{O}(\alpha,\gamma)^{19}\text{Ne}$, calculated rates are used with the associated uncertainties due to this.⁵

1.4.3 Post-breakout behaviour

Once material has left the CNO cycles, explosive nucleosynthesis continues via a series of (p,γ) reactions (the rp-process), (α,p) reactions (the αp -process) and β^+ -decays. From the binding energy curve of nuclei it can be surmised that the effect of a series of rapid capture reactions from around $A=20$ towards the iron peak will be a large increase in energy generation. This is the cause of the burst. Once material has passed the iron peak, the high temperature in the system can continue to drive (p,γ) reactions up towards the ^{100}Sn region. It should be noted that the behaviour of the nuclear network following breakout strongly varies along with the thermodynamic profile of the burst and so the following discussion mentioning important reactions comes with the caveat that some reactions are only important for larger bursts.

For higher temperature bursts, there is still a strong chance that α -induced reactions can take place on nuclei where the β^+ -decay lifetime is quite long and the (p,γ) reaction is not strong. For many neutron-deficient nuclei, the proton separation energy is very small leading to (γ,p) photodisintegration reactions caused by high-energy photons. These α -induced reactions will influence the lightcurve of the burst as they can bypass some of

⁵There have been inverse measurements of some of the reactions. See, for example, Salter *et al.* [18].

the β^+ -decays that slow the rp-process down. Some of the waiting point nuclei in this region that are thought to have astrophysically significant (α,p) channels include ^{22}Mg , ^{26}Si , ^{30}S , ^{34}Ar [19–21].⁶

Above around calcium, these α -induced reaction decrease in importance as the penetrability through the Coulomb barrier drops too low to allow them to proceed. From here a combination of (p,γ) reactions and β^+ -decays drive the network. Many of the (p,γ) reaction rates have not been experimentally determined but are calculated from statistical models. Of particular note are the waiting points near the proton dripline: ^{56}Ni , the long-lived doubly-magic nucleus has a weak (p,γ) channel as ^{57}Cu has a weakly-bound proton and other $N=Z$ nuclei ^{64}Ge , ^{68}Se , ^{72}Kr and ^{76}Sr that all have low (or negative) Q -values for (p,γ) reactions and long β -decay lifetimes.

The termination of nucleosynthesis in X-ray bursts is still unclear. The SnSbTe cycles were previously considered as the likely termination [22] but new mass measurements of nuclides in this region have cast some doubt on this [23].

The end of the X-ray burst occurs when the hydrogen fuel is consumed. Depending on the initial amount of hydrogen (and other nuclides), and the thermodynamic profile of the burst, this can occur at different regions of the nuclear chart. It is believed that insufficient energy is generated in X-ray bursts to overcome the gravitational attraction of the neutron star so the lifting of degeneracy is not an important process in the termination of the burst.

1.5 Observation of X-ray bursts and connection to nuclear physics input

Earth’s atmosphere is opaque to X-rays, observation of X-ray bursts must therefore take place using space-based telescopes [24]. One of the main satellites used for observation of X-ray bursts is the *Rossi X-ray Timing Explorer* which uses three different systems to measure X-rays in different energy regions: a set of three shadow cameras [25], position-sensitive proportional counters viewing X-ray sources through a slit mask which use the shadow pattern created to infer the strength and direction of X-ray sources in a photon energy range of 1.5 to 12 keV; a set of NaI/CsI scintillators which measure X-ray photons in the energy region from 15 to 250 keV [26], and a set of proportional counters which can measure from 2 to 60 keV [27]. This covers the range of appropriate energies for X-ray bursts (2-3 keV) and higher.

The nuclear physics input to X-ray burst models is only one part of the overall model. Astrophysical inputs are also extremely important. These include the hydrodynamics of the burst, mixing between layers in the atmosphere of the neutron star, burning fronts

⁶There are other nuclei which might have strong (α,p) channels but they are likely to be of less importance and have thus been omitted - Ref. [20] contains a full list.

in the atmosphere, multiple ignition points, accretion rate and strong magnetic fields. In massive stars, for example, nucleosynthetic processes such as the s-process which produce heavier nuclei can be decoupled from the energy-producing processes [28]. In these cases the thermodynamic history for the system can be calculated from a stellar model and used to drive a post-processing model to investigate nucleosynthesis. In the case of X-ray bursts, this is not possible or useful: the nuclear reactions involving more massive nuclei in X-ray bursts are also the reactions that produce the energy which cause the burst to take place.

It is unlikely that matter is ejected from X-ray bursts so observation is the only available tool to test models. There are, however, a number of factors which may be derived from observation. These include: whether bursts occur at all, how frequently bursts repeat, how long bursts last and the characteristic timescale of bursts (defined as the total energy produced per unit area over the peak flux of the burst), and the decay timescale of the burst. A number of these factors depend strongly on the composition of the accreted matter (the relative hydrogen and helium abundances effect burst dynamics strongly, for example). However, the most useful test of astrophysical models is the dependence of bursting behaviour on the accretion rate as observations suggest that very high accretion rates (above about 30% of the Eddington limit) suppress bursting behaviour. A number of studies have suggested that high accretion rates should change bursting behaviour due to stable burning to hydrogen to helium between bursts [29–31]. In Ref. [29] the lower limit of the $^{15}\text{O}(\alpha,\gamma)^{19}\text{Ne}$ reaction rate coupled with very high accretion rates lead to stable helium-burning and exhaustion of fuel before bursting conditions are met, resulting in bursting behaviour being totally suppressed. This behaviour is matched by observation. However, the lower limit on the reaction rate recommended by Ref. [31] and used in Ref. [30] (Ref. [30] is an updated study using the same model as Ref. [29] but using the updated upper and lower limits to the $^{15}\text{O}(\alpha,\gamma)^{19}\text{Ne}$ reaction rate from Ref. [31]) suggests that the lower limit of the rate is high enough that this bursting suppression does not take place until accretion rates near the Eddington Limit [24]. Other authors [32] have expressed concerns over the α -particle branching ratios from Ref. [31] while performing calculations that suggest that the remaining uncertainties on the $^{15}\text{O}(\alpha,\gamma)^{19}\text{Ne}$ do not change the burst behaviour. However, it should be noted that the Monte Carlo calculation of a recommended rate in Ref. [32] uses an upper limit for the branching ratio of the 4033-keV state in ^{19}Ne which is, by definition, consistent with zero. However, the fractional reaction rate (how much of the total rate is through that resonance) calculated in Ref. [32], shown in Fig. 8 of the same, does not have some fraction of events which have a fractional reaction rate of zero for the 4033-keV state. This is inconsistent with the statements earlier in the paper and leads to some concerns over the estimation of the lower limit on the reaction rate in Ref. [32].

In summary, there are a number of astrophysical models which predict different burst-

ing behaviours based on the precise value of the $^{15}\text{O}(\alpha,\gamma)^{19}\text{Ne}$ reaction rate and the accretion rate while other models suggest that the bursting behaviour does not depend on the remaining uncertainties in the reaction rate. However, due to the issues identified with the results in Ref. [31], which will be discussed later in this thesis, and with the calculations in Ref. [32], further study of the $^{15}\text{O}(\alpha,\gamma)^{19}\text{Ne}$ reaction is required. Future investigations should endeavour to place a robust lower limit on the $^{15}\text{O}(\alpha,\gamma)^{19}\text{Ne}$ reaction rate, and thus to act as a test of astrophysical models by answering the following question: ‘using a new calculated recommended rate, is it possible to reproduce the observed suppression of bursting behaviour at high accretion rates?’

1.6 The present work

In this thesis are presented three test experiments for studies to determine the $^{15}\text{O}(\alpha,\gamma)^{19}\text{Ne}$ reaction rate; as was discussed in section 1.4.2, this reaction is one of the breakout reactions from the CNO cycles in X-ray bursts. Direct measurement of the reaction rate is extremely difficult as the cross section for the reaction is very small at astrophysical energies, and the beam intensities available are too low for a successful experiment to be carried out in the near future. Lacking a direct measurement, calculations must be used to derive the rate provided the nuclear properties of the nuclei involved in the reaction are known, in this case the spins, parities, widths and branching ratios of states in ^{19}Ne around the α -threshold. Not all of these properties are currently known.

In order to measure the missing α -widths, it is proposed to measure α -cluster transfer reactions onto ^{15}O to determine the α spectroscopic factor for the relevant resonant states. A proposal to do this has been approved at the ISAC radioactive ion beam facility at TRIUMF in Vancouver, Canada. The α width can be determined from this spectroscopic factor. It is hoped that the use of LiF compound targets will allow α -cluster transfer reactions to be probed using $(^6\text{Li},d)$ or $(^7\text{Li},t)$; the first experiment has been carried out as a test of this reaction mechanism. There are a large number of (α,p) reactions relevant to X-ray bursts (mentioned in section 1.4.2 and section 1.4.3) so if the α -cluster transfer can be shown to work, the Γ_α partial widths (see section 2.3) of astrophysically relevant states can be derived for a large number of reactions. A test measurement has been carried out using the SHARC and TIGRESS arrays using a ^{20}Na beam on a ^6LiF target. These arrays underwent extensive upgrades before the experiment, including new DAQ modules and data structure in order to cope with the higher data rates associated with this experiment. The experiment was, in addition to exploring the capability of the array for the measurement, a test for the new DAQ readout modes.

The second experiment was a test of the use of neon-implanted carbon targets which it is hoped could be used in a measurement of the $^{20}\text{Ne}(d,t)^{19}\text{Ne}$ reaction to probe the spins of some key ^{19}Ne resonances. Neon is a noble gas and so it cannot be formed into

solid targets. The alternative option to implanted targets, gas cells, have entrance and exit windows which impair the energy resolution possible in the experiment. There is concern that these neon-implanted targets will not withstand the high beam intensities required for transfer reactions and that this will result in the neon migrating out of the target. The $^{20}\text{Ne}(d,t)^{19}\text{Ne}$ reaction was probed using the Q3D magnetic spectrometer at the Maier-Liebnitz Laboratory at the Technical University of Munich.

The third experiment discussed in this thesis is a test of using an Enge magnetic spectrometer with silicon detectors in the reaction chamber to measure branching ratios of unbound states. This experiment was carried out at the tandem accelerator facility ALTO at Institut de Physique Nucléaire d'Orsay (Orsay). The experiment in this case is a study of the proton- and α -branching ratios for states above the neutron-threshold in ^{27}Al to quantify the destruction of the radioisotope ^{26}Al in massive stars by the neutron-induced reactions $^{26}\text{Al}(n,p)^{26}\text{Mg}$ and $^{26}\text{Al}(n,\alpha)^{23}\text{Na}$. For the purpose of this thesis, the applicability of this system to the $^{19}\text{F}(^3\text{He},t)^{19}\text{Ne}^*(\alpha)^{15}\text{O}$ reaction will be discussed. A measurement of the branching ratio for the α -unbound states in ^{19}Ne allows the Γ_α of these states to be calculated.

In order to present these test experiments and the associated tests of the SHARC/TIGRESS data acquisition system, thermonuclear reaction rates will be introduced in chapter 2 along with their connection to nuclear structure and methods for the extraction of resonance parameters from experiments, a more detailed discussion of the $^{15}\text{O}(\alpha,\gamma)^{19}\text{Ne}$ reaction follows in chapter 3 with particular focus on the properties of the 4033-, 4140- and 4197-keV states. The experimental setup, analysis techniques and discussion of results from the SHARC/TIGRESS data may be found in chapters 4 to 6, while the equivalent information from the Munich Q3D experiment are found in chapters 7 and 8. The Orsay experiment is discussed in chapter 9. Finally, conclusions and suggestions for further work are given in chapter 10.

Chapter 2

Theory

Why is my verse so barren of new pride,
So far from variation or quick change?
Why with the time do I not glance aside
To new-found methods, and to compounds strange?

William Shakespeare - *Sonnet 76*

2.1 Introduction

Thermonuclear reactions are responsible for the energy generation and nucleosynthesis in many stellar environments. Reaction rates are strongly dependent on temperature and the properties of the nuclei involved in the reaction. In this chapter, the cross section is briefly defined before some basic nuclear structure properties are introduced. Resonances are then discussed and the connection between the properties of resonances and the resonant thermonuclear reaction rate is laid out. Finally, basic nuclear reaction mechanisms are introduced along with how the properties of nuclei may be extracted from these experiments.

2.2 Cross sections

The probability that two colliding particles react is represented by the cross section, σ . This is defined as:

$$\sigma = \frac{\text{Interactions in time } t}{\text{Number of beam particles in time } t \text{ per unit area} \times \text{Number of target particles}} . \quad (2.1)$$

This cross section has units of area and can most simply be pictured classically by comparison with the geometric cross section, the physical area covered by each nucleus

from the point of view of a beam incident upon a target. However, as the cross section for a reaction can deviate from the geometrical cross section of the target nucleus by a large amount; it is better to describe the cross section as a probability of interaction.

The differential cross section $\frac{d\sigma}{d\Omega}$ is the probability that a flux of reactants goes into solid angle $d\Omega$. The shape of the differential cross section gives information about the mechanism of the reaction, such as the amount of angular momentum transferred from the relative motion of the projectile and target into internal angular momentum of the reacting nuclei.

2.3 Resonances

Resonances are ‘nearly bound’ states. They are characterised by a number of different properties: a resonance energy (E_r), a spin-parity (J^π), a lifetime (τ), and branching ratios for each open channel (B_i). The lifetime is related to the total width of the resonance (Γ ; this is a measure of the decay rate of the resonance) by $\Gamma = \frac{\hbar}{\tau}$, \hbar being the reduced Planck constant; the partial widths (decay rates into each open channel, i) are then given by $\Gamma_i = B_i\Gamma$.

Widths depend on a number of different factors. First of all, Coulomb and angular momentum potential barriers can result in energetically forbidden regions through which a particle which is being emitted must tunnel. This is the penetrability P_ℓ , where ℓ is the orbital angular momentum, and can be calculated using the approximations laid out in section 2.4.1.

The width also depends on the spectroscopic factor, S . This is a measure of the probability that, in the initial state, all of the nucleons except those which are to be emitted are arranged in the final state of the system [33]. The factor serves as a measurement of the component of the compound state that can be described by the core plus a single-particle state; if a resonance is well-described as a core plus a nucleon or a cluster of nucleons (for example, ^{17}O being composed of a doubly-magic ^{16}O core and a $d_{5/2}$ neutron), then the spectroscopic factor will be large.

Finally, the width depends on the dimensionless single-particle reduced width, θ_{sp} . This is the probability that the emitted particle appears at the boundary of the nucleus. This can be computed using an appropriate nuclear potential [34, 35].

Combining these factors, it is possible to compute the partial width for a channel:

$$\Gamma_i = \frac{2\hbar^2}{\mu R^2} P_\ell C^2 S_i \theta_{sp}^2, \quad (2.2)$$

where R is the interaction radius used for calculating θ_{sp} and P_ℓ , μ is the reduced mass given by: $\mu = \frac{m_1 m_2}{m_1 + m_2}$ and C is the isospin Clebsch-Gordon coefficient, which represents the different vectorial additions for isospin which can combine to give the final isospin.

This equation may also be expressed as:

$$\Gamma_i = C^2 S \Gamma_{i,sp} , \quad (2.3)$$

where $\Gamma_{i,sp}$ is the single-particle width as defined by:

$$\Gamma_{i,sp} = \frac{2\hbar}{R} \sqrt{\frac{2E}{\mu}} \frac{1}{F_\ell(\eta, kR)^2 + G_\ell(\eta, kR)^2} , \quad (2.4)$$

where E is the energy in the centre-of-mass frame, μ is the reduced mass, R is the interaction radius and k is the wave-number in the centre of mass frame ($k = \sqrt{\frac{2\mu E}{\hbar^2}}$) and F_ℓ and G_ℓ are the regular and irregular Coulomb functions respectively. The previously defined penetrability is found in eq. (2.4) as:

$$P_\ell = \frac{1}{F_\ell(\eta, kR)^2 + G_\ell(\eta, kR)^2} . \quad (2.5)$$

The cross section for resonant reactions proceeding through a resonance in the compound nucleus via the incoming channel, i , and the outgoing channel, f is given by the Breit-Wigner equation:

$$\sigma_{if}(E) = \frac{\lambda^2}{4\pi} \frac{2J+1}{(2j_a+1)(2j_b+1)} (1 + \delta_{ab}) \frac{\Gamma_i \Gamma_f}{(E - E_r)^2 + \frac{\Gamma^2}{4}} , \quad (2.6)$$

where λ is the de Broglie wavelength, the various $(2j+1)$ factors account for averaging over the incoming spin projections and summing over the outgoing, and the $(1 + \delta_{ab})$ factor applies when the reactions are between identical particles, a and b denoting the reactants in this equation.

The resonance strength is proportional to the maximum cross section and the total width of the resonance, this quantity can often be useful when discussing reaction rates and is defined as:

$$\omega\gamma_{ij} = \frac{2J+1}{(2j_a+1)(2j_b+1)} \frac{\Gamma_i \Gamma_j}{\Gamma} . \quad (2.7)$$

If the resonance parameters for all resonances are known, then the cross section at all incident energies can be computed and used to calculate the reaction rate for an astrophysical reaction. The theory behind this is laid out in the section below.

2.4 Thermonuclear reaction rates

Using the definition for the cross section in Equation 2.1, an expression for the reaction rate can be derived. Reaction rates are defined in terms of reactions per unit volume per unit time. It is useful to consider the simplistic example of a particle beam of speed v

hitting a target. In this case, the total number of reactions per unit volume per unit time can be expressed as:

$$\frac{N_r}{Vt} = \sigma(v) \frac{N_{target}}{V} \frac{N_{beam}}{At} , \quad (2.8)$$

where N_r is the number of reactions, V is an arbitrary unit volume, A is an arbitrary cross sectional area and t an arbitrary unit time, $\sigma(v)$ the cross section as a function of the beam velocity, N_{target} is the number of target ions, and N_{beam} is the number of beam ions. Equation (2.8) can be interpreted to be a probability of interaction, σ , multiplied by the number density of both reactants. However, the target nuclei are stationary and the beam ions are moving

The beam current density, the number of incident beam ions per time per area is given by $\frac{N_{beam}}{At}$. However, given a beam velocity of v , this quantity can be expressed as: $\frac{vN_{beam}}{V}$. Using this, eq. (2.8) becomes:

$$\frac{N_r}{Vt} = \sigma(v) \frac{N_{target}}{V} \frac{vN_{beam}}{V} . \quad (2.9)$$

Defining the number densities of the reactants as: $n_{target} = \frac{N_{target}}{V}$ and $n_{beam} = \frac{N_{beam}}{V}$, Equation (2.9) can be rewritten as:

$$H = \sigma(v)vn_{target}n_{beam} , \quad (2.10)$$

where H is the reaction rate.

This definition of the reaction rate is still written in the form of a beam-like particle hitting a target-like particle. However, the quantity v is just the relative velocity between target and beam particles. This means eq. (2.10) can be used to calculate the total rate in a plasma without variation.

Unlike a monoenergetic beam, particles in astrophysical environments have a range of energies, depending on the temperature. The relative velocity of the reactants will not be a single value but will take a large range of values, described by the Maxwell-Boltzmann distribution. Equation (2.10) is usually written as:

$$H = n_{target}n_{beam}\langle\sigma v\rangle , \quad (2.11)$$

where

$$\langle\sigma v\rangle = \int P(v)v\sigma(v)dv , \quad (2.12)$$

and the Maxwell-Boltzmann distribution in the relative velocity is:

$$P(v)dv = 4\pi v^2 \left(\frac{\mu}{2\pi kT}\right)^{\frac{3}{2}} e^{-\frac{\mu v^2}{2kT}} dv , \quad (2.13)$$

where $\mu = \frac{m_1 m_2}{m_1 + m_2}$ is the reduced mass where m_1 and m_2 are the masses of the species

involved in the reaction, k is the Boltzmann constant, and T is the temperature in Kelvin. Equation (2.11) is the ‘weighted sum’ of σv , weighted by the distribution of velocities for the reactants.

Finally, velocity can be converted to energy using the non-relativistic relationship between energy and velocity, $E = \frac{1}{2}\mu v^2$. The Maxwell-Boltzmann distribution becomes:

$$P(E)dE = \frac{2}{\sqrt{\pi}} \frac{1}{(kT)^{\frac{3}{2}}} \sqrt{E} e^{-\frac{E}{kT}} dE , \quad (2.14)$$

which is plotted in fig. 2.1.

Using eq. (2.14) in eq. (2.12) gives:

$$\langle \sigma v \rangle = \left(\frac{8}{\pi \mu} \right) \left(\frac{1}{kT} \right) \int \sigma(E) E e^{-\left(\frac{E}{kT}\right)} dE . \quad (2.15)$$

This allows the reaction rate to be calculated from the cross section. The cross section consists of two parts; a non-resonant direct-capture contribution which tends to be very small, and a resonant contribution due to capture into resonances in the compound nucleus. The resonant contribution to the rate is discussed in section 2.4.3.

The thermal energy scale from the Maxwell-Boltzmann distribution is $\sim kT$, or $86.3T_9$ keV, where T_9 is the temperature in GK. However, the Coulomb barrier between two nuclei of proton numbers Z_1 and Z_2 is [15]:

$$\begin{aligned} B_{Coulomb} &= \frac{1}{4\pi\epsilon_0} \frac{Z_1 Z_2 e^2}{R_0} \\ &= 1.44 \frac{Z_1 Z_2}{R_0} \text{MeV} , \end{aligned} \quad (2.16)$$

where R_0 is the radius at which the nuclear surfaces can interact, given in fm.

Temperatures in stellar environments are usually in the range of 10s of MK to a few GK. Comparing the energy scale of thermal interactions to the Coulomb barrier that must be overcome, it is obvious that the only way for the nuclear surfaces to come close is via quantum-mechanical tunnelling through the barrier. It is therefore necessary to calculate the penetrability through the barrier of particles.

2.4.1 Penetrability

The penetrability can be calculated by considering the transmission probability, Θ , through a square potential barrier of height V_0 .¹ For a low energy incident particle of energy E , and a wide barrier of thickness δr , this quantity is [15]:

¹This penetrability, *Theta* is the same as the *s*-wave penetrability P_0 as defined in section 2.3

$$\Theta \approx \exp\left(-\frac{2}{\hbar}\sqrt{2m(V_0 - E)}\delta r\right). \quad (2.17)$$

Considering the limit where $\delta r \rightarrow 0$, a limit which is equivalent to considering the transmission through an infinitesimally-thin square potential barrier and modelling the Coulomb potential as comprised of a series of these barriers, it is possible to write down the transmission through one of these barriers as:

$$\Theta_i = \exp\left(-\frac{2}{\hbar}\sqrt{2m(V_i - E)}(r_{i+1} - r_i)\right), \quad (2.18)$$

where $V_i = \frac{1}{4\pi\epsilon_0}\frac{Z_1Z_2e^2}{r_i}$ and $r_{i+1} = r_i + \delta r$.

The total probability of transmission through the barrier will be given by the product of the transmissions through each infinitesimal barrier:

$$\Theta_{total} = \prod_i \Theta_i. \quad (2.19)$$

It is possible to express this equation as:

$$\Theta_{total} = \exp\left(-\frac{2}{\hbar}\sum_i \sqrt{2m(V_i - E)}(r_{i+1} - r_i)\right). \quad (2.20)$$

Letting $\delta r \rightarrow 0$ leads to:

$$\Theta_{total} = \exp\left(-\frac{2}{\hbar}\int_{R_0}^{R_c} \sqrt{2m(V(r) - E)}dr\right). \quad (2.21)$$

where R_c is the classical turning point, that radius where the energy of the incoming particle is equal to the potential barrier ($R_c = \frac{1}{4\pi\epsilon_0}\frac{Z_1Z_2e^2}{E}$), and R_0 is nuclear radius. A useful quantity to define is the barrier height at point where the nuclear surfaces touch which is given in eq. (2.16). Evaluation of this integral (see appendix A) leads to the Gamow factor [15]:

$$\Theta_{total} \approx \exp\left(-\frac{2\pi}{\hbar}\sqrt{\frac{m}{2E}}\frac{Z_1Z_2e^2}{4\pi\epsilon_0}\right). \quad (2.22)$$

which is usually expressed as $e^{-2\pi\eta}$, where η is the Sommerfeld parameter.

Using this Coulomb penetrability definition, the cross section at any given energy can be re-expressed in terms of an astrophysical S-factor. This avoids the variation over many orders of magnitude which results from the strong variation of the penetrability on energy. The S-factor is defined as:

$$\sigma(E) = \frac{1}{E}e^{-2\pi\eta}S(E). \quad (2.23)$$

where the dependence of the s -wave Coulomb penetrability has been absorbed into the

factor of $e^{-2\pi\eta}$.

2.4.2 The Gamow Window and direct measurements

Figure 2.1 shows the Maxwell-Boltzmann distribution (which is given in eq. (2.14)); it is obvious that the proportion of particles with a high energy is very low. Figure 2.2 shows that particles with low energies do not have a high chance of penetrating far enough through the Coulomb barrier to allow for interaction between the nuclear surfaces. The interplay between these two factors can be seen in fig. 2.3: there is a region with a much higher probability of a successful reaction, this is the Gamow window. It is obvious from fig. 2.3 that the astrophysically relevant energies are very low and that the penetrability, and thus the cross section, will be very small at these energies. This leads to one of the primary problems in nuclear astrophysics. Direct measurements of the cross section in the astrophysically relevant Gamow window have such low cross sections that they are often impossible to measure. This is especially true in the case of α -induced reactions on radioactive nuclei; the intensity of the radioactive ion beam required coupled with the need for a gas target, which will have a low density of target ^4He nuclei, and the low cross section results in such a low reaction yield that often only upper limits of cross sections are possible.

The Gamow window is usually approximated as Gaussian with a centroid of $0.122(Z_1 Z_2 \mu)^{\frac{1}{3}} T_9^{\frac{2}{3}}$ MeV and a width of $0.2368(Z_1 Z_2 \mu)^{\frac{1}{6}} T_9^{\frac{5}{6}}$ MeV where $Z_{1,2}$ are the charges of the species involved, $\mu = \frac{A_1 A_2}{A_1 + A_2}$ is the reduced mass and T_9 is the temperature in GK.

2.4.3 Resonant reactions

Resonant reactions are those which proceed via a resonance in the compound nucleus. These resonances cause large deviations in the S-factor and can increase the cross section by orders of magnitude in a particular energy region. Resonances which fall within the Gamow window dominate the reaction rate and the rate ‘through’ each resonance depends upon the properties of that resonance.

Putting the Breit-Wigner cross section, eq. (2.6), into eq. (2.15), it is possible to calculate a reaction rate from an isolated narrow resonance [15], given by:

$$N_A \langle \sigma v \rangle = \frac{1.5396 \times 10^5}{\mu^{\frac{3}{2}} T_9^{\frac{3}{2}}} \sum_i (\omega \gamma)_i e^{(-11.605 E_{ri}/T_9)} \text{cm}^3 / \text{mol/s} , \quad (2.24)$$

where T_9 is the temperature in GK, E_{ri} (in MeV) is the resonance energy of the i th resonance and $(\omega \gamma)_i$ (in MeV) is the resonance strength of the i th resonance, as previously defined in eq. (2.7). A narrow resonance is one for which the Maxwell-Boltzmann factor and partial widths remain approximately constant over the total resonance width. An isolated resonance is one which does not overlap with another.

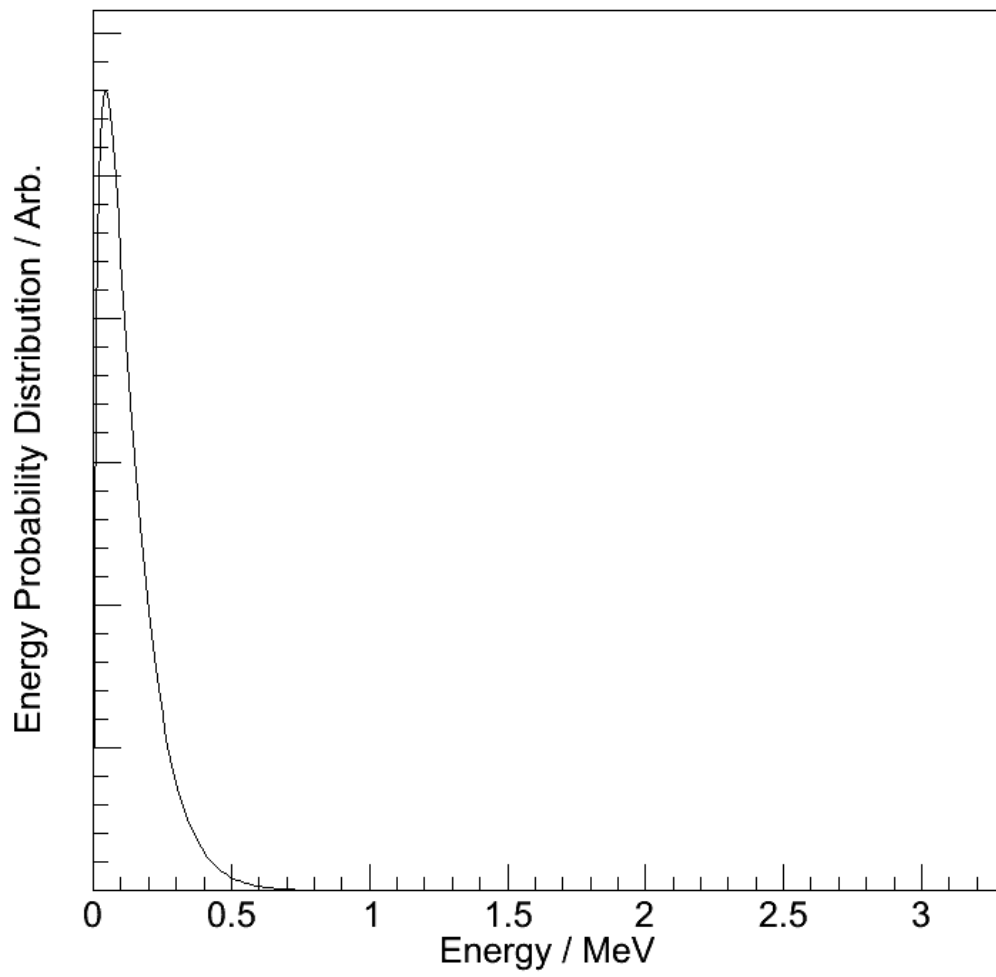


Figure 2.1: Probability distribution for energy at $T_9 = 1$.

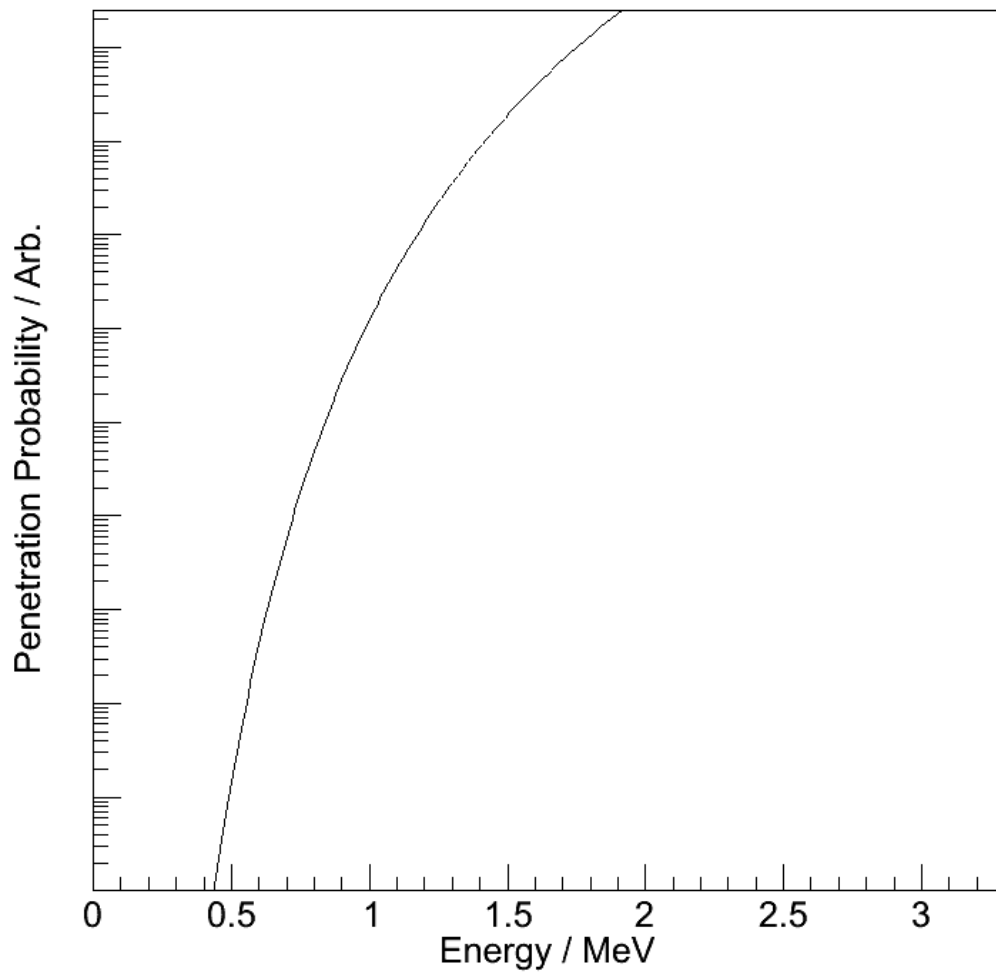


Figure 2.2: Penetration through a potential barrier for the example of $^{15}\text{O}(\alpha,\gamma)^{19}\text{Ne}$.

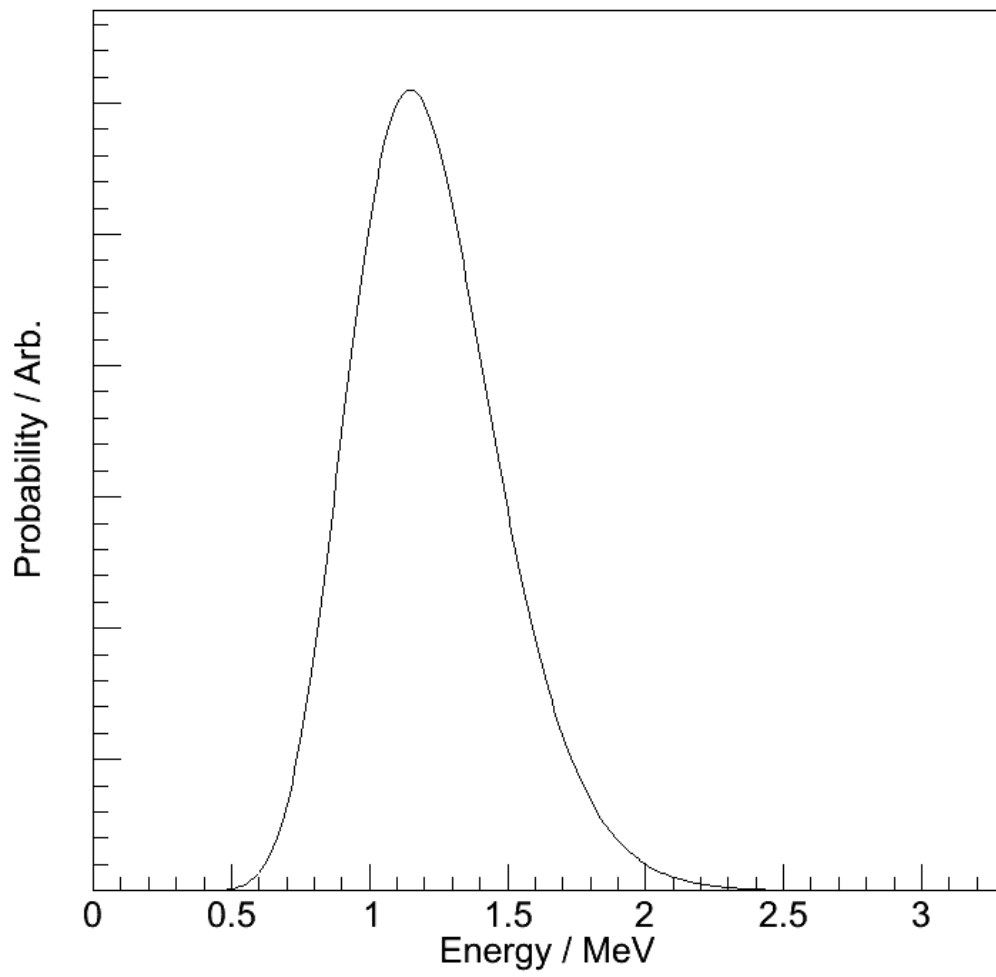


Figure 2.3: The Gamow Window for $^{15}\text{O}(\alpha,\gamma)^{19}\text{Ne}$ at $T_9 = 1$.

From this, it is obvious that the resonant reaction rate from isolated narrow resonances will be governed by the resonance energy, the partial widths and the spin-parities. Determination of these parameters for each resonance, therefore, should allow the resonant reaction rate from isolated narrow resonances to be calculated.

For wider resonances, it is necessary to account for the variation in the Maxwell-Boltzmann factor and the partial widths over the width of the resonance. In this case, numerical integration over the relevant energy range is required.

2.5 Nuclear reactions

In the previous section, the reaction rate was introduced along with an account of how the rate can be calculated using information about resonances in the compound nucleus. Nuclear reaction studies allow these parameters to be measured; the energies of the reaction products can be used to find the resonance energies and angular momentum transfers and spectroscopic factors can be found by comparing the angular distributions to the results of Distorted Wave Born Approximation (DWBA) calculations. In this section, DWBA is briefly outlined along with the relation between DWBA cross sections and the spectroscopic factor.

Timescales can be used to conveniently describe the form of the nuclear reaction that has taken place. Compound nucleus reactions involve nuclei which have fused for long enough for many nucleon-nucleon interactions to take place. Direct transfer reactions are ‘glancing blows’ on nuclei where the reaction is fast enough that, at the most, a few nucleon-nucleon interactions may take place. Different mechanisms lead to very different behaviours of outgoing nuclei, both of which can be useful when investigating resonance properties.

2.5.1 Direct reactions and the DWBA

Direct reactions occur over short timescales and involve few nucleon-nucleon interactions. In this case, the projectile retains information from before the interaction and the angular distribution is strongly peaked at low scattering angles. Direct reactions are more probable at higher energies as the de Broglie wavelength is shorter, probing individual nucleon behaviours in the nucleus.

Transfer reactions are a common tool in nuclear physics. Angular distributions from transfer reactions differ markedly depending on the ℓ -value transferred, allowing the J^π of states to be derived. In order to have an angular distribution to compare to, however, one must be calculated using some sort of reaction theory. In this case, the Distorted-Wave Born Approximation was used. The Born Approximation is that, if the interaction strength is small in comparison to the interaction energy of the bound system, it can be treated as a perturbation. If this assumption is made it is possible to consider, instead

of a complete interaction theory which includes many intermediate steps to give a final angular distribution, a process which is limited to a finite number of steps. The Born Approximation usually refers to the first-order Born Approximation, that which limits the number of steps considered in the interaction to one.

In the case of transfer reactions which involve charged particles, the incoming and outgoing waves must be expressed in terms of the Coulomb functions, the distorted waves of DWBA. The Born approximation in this case involves splitting the potential into two parts [36]. If the larger potential is well-known, such as the Coulomb potential then the wavefunctions of the system can be expressed in terms of the Coulomb functions which solve the Schrodinger equation for the Coulomb potential.

Comparison between the differential cross section of the outgoing species and DWBA calculations allows the ℓ -value of the reaction to be assigned. Note that, if other spins are involved in the reaction, the J^π might not be fully defined. For example, in a (d,t) reaction involving the transfer of a spin- $\frac{1}{2}$ neutron, the possible final spins are $\ell \pm \frac{1}{2}$.

Transfer reaction cross sections strongly depend on the momentum transfer. In order to understand the angular distribution and ℓ -values populated in transfer reactions, a simple semi-classical model can be evaluated. Considering the case of an incident particle with momentum \underline{p}_i and an outgoing particle with momentum \underline{p}_j . The residual nucleus recoils with momentum $\underline{q} = \underline{p}_i - \underline{p}_j$. For a surface interaction, the transferred nucleon with the recoil momentum will be placed into an orbit of angular momentum $\ell = R|\underline{q}|$. $|\underline{q}|$ may be found using $|\underline{q}|^2 = (|\underline{p}_i| - |\underline{p}_j|)^2 + 2|\underline{p}_i||\underline{p}_j|(1 - \cos\theta)$. This shows the angular dependence of the transferred momentum (not only explicitly in θ but also in \underline{p}_j). The angular distribution is expected to peak at the angle at which the matching condition, $\ell = R|\underline{q}|$, is best satisfied.

The beam and number of nucleons transferred in a transfer reaction also influence the angular momentum transferred. Larger changes in linear momentum are possible with heavier beams. For example, the neutron-stripping reactions (d,p) and $(\alpha,^3\text{He})$ are both used to probe neutron spectroscopic factors; the former populates states which require lower ℓ -values while the latter populates states requiring higher ℓ -values [37]. This ℓ -value effect is demonstrated in fig. 2.4 for the $^{20}\text{Ne}(d,t)^{19}\text{Ne}(4.033 \text{ MeV})$ and $^{20}\text{Ne}(^3\text{He},^4\text{He})^{19}\text{Ne}(4.033 \text{ MeV})$ reactions; the ℓ -values populated in the latter reaction are much higher than those for the former reaction.

2.5.2 Relating the spectroscopic factor and the DWBA cross section

The strength of the transfer reaction depends on the spectroscopic factor. The spectroscopic factor is a “*reduced cross section*” [37] with DWBA handling the kinematic aspects of the reaction. The experimentally measured cross section is related to the DWBA cross section and the spectroscopic factor by:

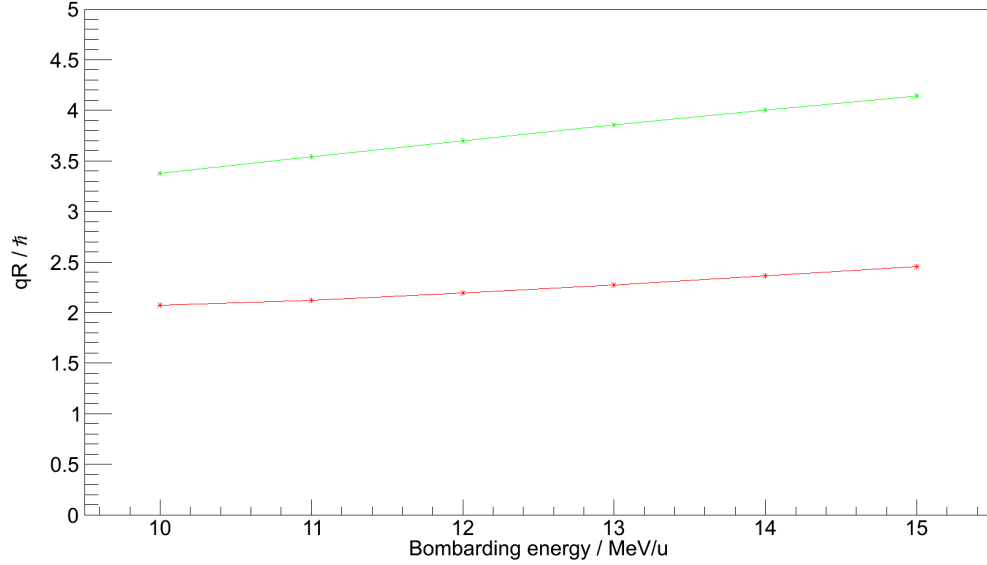


Figure 2.4: Plot of qR as a function of bombarding energy for $^{20}\text{Ne}(d,t)^{19}\text{Ne}(4.033\text{ MeV})$ (red) and $^{20}\text{Ne}(^3\text{He}, ^4\text{He})^{19}\text{Ne}(4.033\text{ MeV})$ (green).

$$\left(\frac{d\sigma}{d\Omega}\right)_{\text{experiment}} = C^2 S \left(\frac{d\sigma}{d\Omega}\right)_{DWBA} . \quad (2.25)$$

To extract spectroscopic factors, the experimental cross section is compared to the DWBA cross section. The nucleus strongly absorbs nucleons; if the nucleus is assumed to be an opaque disk, then the scattering of nucleons is not dissimilar to the diffraction of light [38]. This results, as in the case for diffraction, in a series of intensity fringes in the differential cross section. The differential cross section should not be used to extract spectroscopic factors beyond the first minimum [39,40], in some cases spectroscopic factors are extracted only at the first peak in the differential cross section as this is the point at which the Born approximation is best satisfied [37]. The first maximum corresponds to the impact parameter where the projectile grazes the surface; reactions at higher angles have smaller impact parameters and are more likely to contain multiple interactions, violating the central assumption of the first-order Born approximation.

Chapter 3

The $^{15}\text{O}(\alpha,\gamma)^{19}\text{Ne}$ Reaction and Indirect Studies

Now what is the message there? The message is that there are no “knowns.” There are things we know that we know. There are known unknowns. That is to say there are things that we now know we don’t know. But there are also unknown unknowns. There are things we do not know we don’t know.

Donald Rumsfeld, US Secretary of Defense

3.1 Introduction

Before talking about the tests for future experiments looking at the $^{15}\text{O}(\alpha,\gamma)^{19}\text{Ne}$ reaction rate, a brief summary of the currently available experimental information is provided.

The $^{15}\text{O}(\alpha,\gamma)^{19}\text{Ne}$ reaction rate has never been experimentally determined and, given the high beam intensity required for a direct measurement, it is unlikely that a direct measurement will be made soon. It is therefore necessary to rely on calculations of the total rate. However, there is incomplete information on spins and α -branching ratios for the states within the Gamow window in ^{19}Ne . The known information and remaining uncertainties are laid out in this chapter along with a brief discussion of the relative impact of the various states. In addition, the connection between the as-yet undetermined parameters and the experimental tests which have been carried out are also described in this chapter. However, discussion of the apparatus used for these experiments is left until later chapters.

In order to calculate the contribution of each resonance to the $^{15}\text{O}(\alpha,\gamma)^{19}\text{Ne}$ reaction rate, there are a number of pieces of information that are required. The resonance energy, E_r , the spin-parity of the resonance, J^π , the total width of the resonance, Γ , and the α -particle width (or the branching ratio). In the following sections are set out the known

information on ^{19}Ne resonances along with discussions of previous measurements. First of all, the known structural information on the resonance is set out, followed by discussions of previous experiments which give the resonance energies, total widths, spin-parities and finally the α -particle widths through the α -particle spectroscopic factor and the α -particle branching ratio.

3.2 States in ^{19}Ne relevant to the $^{15}\text{O}(\alpha,\gamma)^{19}\text{Ne}$ reaction rate

The α threshold in ^{19}Ne lies at 3529 keV, while the proton threshold is at 6411 keV. Therefore, for the states in the Gamow window (which at 0.5 GK is from 4153 keV to 4593 keV excitation in ^{19}Ne), only two modes of decay are possible, α and γ emission. Due to the large Coulomb barrier for α -particle emission, γ decay dominates the total decay. The rate can be calculated from certain properties of the states that fall within the Gamow window: the resonance energies, the spin-parities, the total widths and the α partial width or branching ratio.

For reference, a level scheme of ^{19}Ne in the region above the α -threshold is reproduced in fig. 3.1 with excitation energies, resonance energies, J^π and ℓ -values marked.

In this thesis, the lowest three resonances above the α -particle threshold are of interest, and so discussion will be limited to these resonances.

3.3 Structural information

There is some structural information available on the relevant resonances. The $^{21}\text{Ne}(p,t)^{19}\text{Ne}$ was used to investigate states in ^{19}Ne [42]. The high cross section to the 4033-keV state leads to an interpretation of this state as a 5 particle-2 hole state, as shown in fig. 3.2a, a particle configuration of ^{21}Ne with a hole structure of ^{14}O . This would suggest that the α -particle spectroscopic factor for this state will be small; a simplistic comparison is that, in the dominant configuration, there is no $p_{1/2}$ neutron, whilst the ^{15}O ground state from which the $^{15}\text{O}(\alpha,\gamma)^{19}\text{Ne}$ reaction would proceed, is well-described by an unpaired neutron in the $p_{1/2}$ orbital.

The 4140/4197-keV doublet has frequently been described in terms of a $p_{1/2}$ hole coupled with an α -particle or equivalently the rotational band built on the deformed ground state of ^{20}Ne coupled with the $p_{1/2}$ ground state configuration of ^{15}O [43,44]. In the $A = 19$ doublet, there is a rotational band built upon the low-lying $1/2^-$ state. This configuration causes a $3/2^-/5/2^-$ doublet and a $7/2^-/9/2^-$ doublet. For the mirror states in ^{19}F , the large cross section in the $^{15}\text{N}(^6\text{Li},d)^{19}\text{F}$ reaction confirms this structure [43–45].

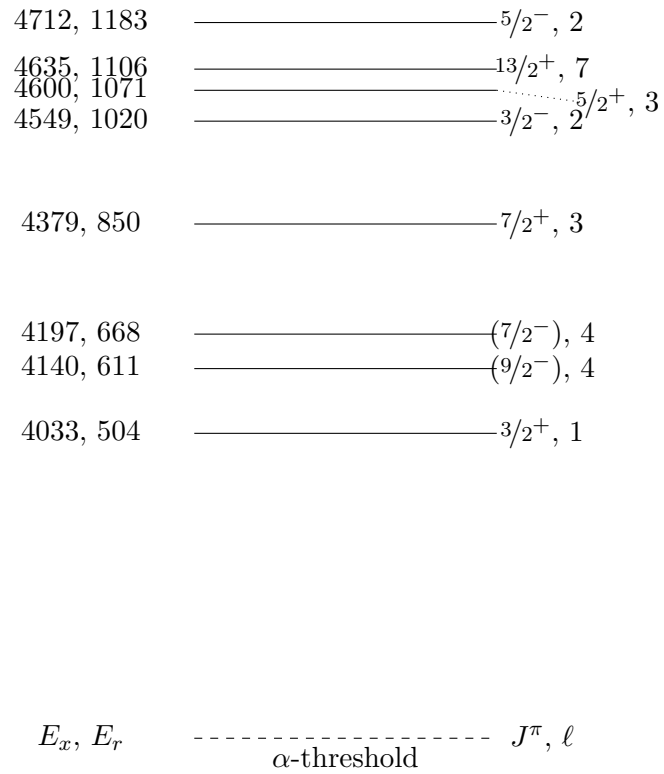


Figure 3.1: ^{19}Ne level scheme above the α -threshold. Energies of the levels above the ground state and above the α -threshold are both marked, as are the J^π of each state and the ℓ -value required to populate the state from the ground state of ^{15}O . Information is taken from the compilation of Tilley *et al.* [41].

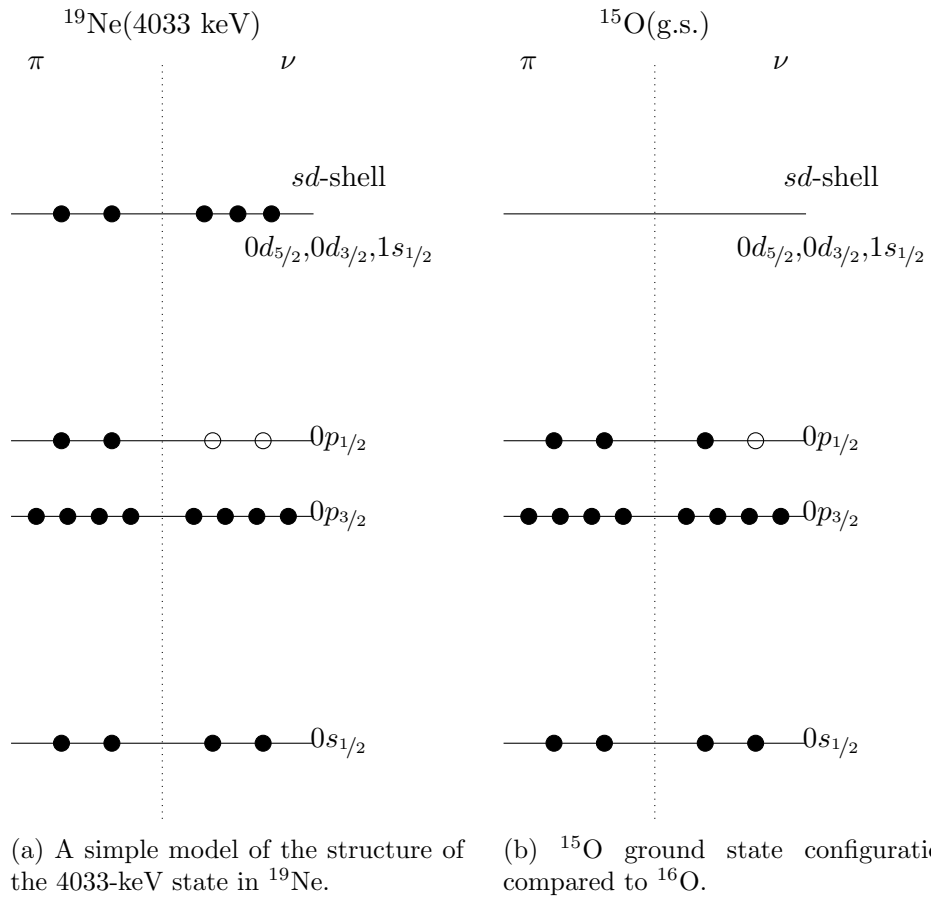


Figure 3.2: Simplified shell-model configurations for the 4033-keV state in ^{19}Ne and the ground state of ^{15}O . The $p_{1/2}$ in the ground state of ^{15}O has no equivalent nucleon in the 4033-keV state in ^{19}Ne . Filled circles represent nucleons while empty circles represent holes.

3.4 Evaluating previous studies and prior information

Before discussing the available experimental information, it is worth considering the relative merits of different experimental approaches. There are two main considerations with studies of the type covered in this thesis: knowledge of the state populated in the reaction, requiring a good energy resolution, and detection of the particle emitted from that state, which requires a high efficiency. Normal and inverse kinematics both have relative merits in this context and choice of the reaction kinematics has therefore an important effect on the efficacy of the experiment.

A strong consideration with the choice of reaction kinematics is the availability of beam and target. If a reaction requires a radioactive beam, then the experiment must be performed in inverse kinematics (with the exception of when the target is a long-lived species which may be formed into a target such as ^{26}Al). In addition, for many experiments involving inverse kinematics, the efficiency of the experiment is higher [46]. On the other hand, inverse kinematics has a detrimental effect on the energy resolution in an experiment due to kinematic compression and, frequently, higher energy loss through the target. In cases where the energy resolution is poor, separating out the contribution of each state to the total reaction rate can be difficult. This is especially true if some of the states have a large branching ratio as the overlapping sections of the distribution can obscure counts from states with weaker distributions.

Particular issues regarding experimental design which are relevant to the experiments in this thesis are discussed at the end of this chapter.

For completeness: information on resonance energies can be found in Tilley *et al.* [41]. The uncertainties in the resonance energies are small and do not dominate the uncertainty in the reaction rate. The largest uncertainty in the $^{15}\text{O}(\alpha,\gamma)^{19}\text{Ne}$ reaction rate lies in the α -particle branching ratios. Discussion will therefore be focussed on these properties.

3.4.1 Total widths

The total width is related to the lifetime of a state by $\Gamma = \frac{\hbar}{\tau}$. Therefore, the total width can be determined if the lifetime can be measured. This has been done by using Doppler-Shift Attenuation Measurements (DSAM) [47–49]. In Ref. [47], the $^{17}\text{O}({}^3\text{He},n\gamma)^{19}\text{Ne}$ reaction was used whilst in Refs. [48, 49] a ${}^3\text{He}$ -impanted gold foil was used along with a ^{20}Ne beam to populate states via the $^{20}\text{Ne}({}^3\text{He},\alpha)^{19}\text{Ne}$ reaction. The recoiling ^{19}Ne slows down in the target after the interaction has taken place, resulting in a range of different recoil velocities when the decay occurs, and thus a broadened energy spectrum. From the lineshape of the energy spectra, the lifetimes of the states are determined. Results are given in table 3.1.

Energy / keV	τ / fs [47]	τ / fs [48]	τ / fs [49]
4033	13_{-6}^{+9}	11_{-3}^{+4}	$6.9_{-1.5}^{+1.5} \pm 0.7$
4140	18_{-3}^{+2}		$14_{-4.0}^{+4.2} \pm 1.2$
4197	43_{-9}^{+12}		$38_{-10}^{+20} \pm 2$

Table 3.1: Lifetimes of states in ^{19}Ne from Refs. [32, 47–49]. N.B. that the values from Ref. [32] are from

3.4.2 Spin-parities

The spin-parity of the 4033-keV state is well-known: from the $\ell = 0$ shape of the angular distribution of the $^{21}\text{Ne}(p,t)^{19}\text{Ne}$ reaction, the spin-parity is $3/2^+$ as the spin-parity of this state must be the same as the ground state of ^{21}Ne .

For the 4140- and 4197-keV doublet, some uncertainty remains about the spin-parities. One state must be a $7/2^-$ and the other must be $9/2^-$. Assignment of spin-parities ($9/2^-/7/2^-$) have been made based on the DWBA angular distributions from the $^{16}\text{O}(^6\text{Li},t)^{19}\text{Ne}$ reaction [41, 50]. Davids *et al.* suggest that the γ -ray reduced transition probabilities of these states favour the assignments being reversed but note that the branching ratios favour the existing assignment. Resolving this issue is part of the focus of this work. The details of the transition rates and the branching ratios are given in table 3.2.

3.4.3 α -particle spectroscopic factors

There have been a number of attempts to determine the α -particle partial width using α -particle transfer reactions to populate the mirror states in ^{19}Ne [43, 45, 52]. Whilst there are concerns about the applicability of mirror symmetry in the case of weak spectroscopic factors [51], these results suggest that the α -particle width for the 4033-keV state in ^{19}Ne should be $9.9 \pm 1.5 \mu\text{eV}$. It should be noted that Refs. [52] and [45] cannot resolve the mirror doublet (the 3999- and 4033-keV states in ^{19}F) meaning that extraction of the α -particle widths for these states is subject to larger uncertainties.

3.4.4 α -particle branching ratios

There have been a number of direct attempts to measure the α -particle branching ratios directly. In this section, previous experiments will be summarised along with a discussion of potential issues with each measurement. All of these studies use the same basic principle: population of a state in ^{19}Ne , the energy of which is known from the detection of the reaction products followed by the attempted detection of a coincident α -particle or ^{15}O heavy recoil to quantify the proportion of events which decay by α -particle emission.

Magnus *et al.* used the QDDD spectrometer (tritons for excitation energy) at Princeton

Nuclide	Initial state / keV, J^π	Final state / keV, J^π	Branching ratio	Transition strength
^{19}F	3999, $7/2^-$	1346, $5/2^-$	70%	$B(\text{M1}) = 0.0017^{+0.0010}_{-0.0005} \text{ MeV fm}^3$
^{19}F	4033, $9/2^-$	1346, $5/2^-$	100%	$B(\text{E2}) = 90 \pm 20 \text{ MeV fm}^5$
^{19}Ne	4140, $7/2^-$	1508, $5/2^-$	100%	$B(\text{M1}) = 0.0024^{+0.0010}_{-0.0009} \text{ MeV fm}^3$
^{19}Ne	4140, $9/2^-$	1508, $5/2^-$	100%	$B(\text{E2}) = 460^{+180}_{-100} \text{ MeV fm}^5$
^{19}Ne	4197, $7/2^-$	1508, $5/2^-$	80%	$B(\text{M1}) = 0.0008^{+0.0003}_{-0.0003} \text{ MeV fm}^3$
^{19}Ne	4197, $9/2^-$	1508, $5/2^-$	80%	$B(\text{E2}) = 150^{+60}_{-50} \text{ MeV fm}^5$

Table 3.2: Branching ratios and transition strengths for the doublet states in ^{19}F and ^{19}Ne [32]. The branching ratios clearly favour a $9/2^-$ - $7/2^-$ ordering of the levels. However, the $B(\text{E2})$ transition strength calculated assuming the 4140-keV state is $9/2^-$ is very large in comparison to that of the $9/2^-$, 4033-keV state in ^{19}F . The reader should note that concerns have been raised over the veracity of $B(\text{M1})$ mirror symmetry; there is a discussion in Ref. [51] on the use of $B(\text{M1})$ mirror symmetry in the ^{19}F - ^{19}Ne system for the purpose of calculating the influence of higher-lying resonances in ^{19}Ne on the $^{15}\text{O}(\alpha,\gamma)^{19}\text{Ne}$ reaction rate at higher temperatures.

along with silicon surface barrier detectors (subsequent α -particles) and the $^{19}\text{F}(^3\text{He},t)^{19}\text{Ne}$ reaction in normal kinematics to measure the α -particle branching ratios [53]. This experiment is similar to that proposed later on in this thesis. There is one major difference, however. In this experiment, silicon surface barrier detectors were used, as opposed to the double-sided silicon strip detector (DSSSD) setup proposed. This resulted in a higher experimental background due to scattered beam which can be suppressed somewhat with the use of DSSSDs. This means that α -particle branching ratios cannot be extracted for the 4033-, 4140- and 4197-keV states.¹ This is, however, the only previous experiment which can be considered robust (see notes below on Ref. [54] which is able to separate the 4140-keV and 4197-keV states.

Visser *et al.* used the $^{19}\text{F}(^3\text{He},t)^{19}\text{Ne}$ reaction in normal kinematics using an Enge magnetic spectrometer to detect the tritons produced along with silicon strip detectors to detect coincident α -particles [54]. There are problems with the normalisation of this experiment due to the threshold in the electronics in the silicon detectors. The α -particle branching ratios from this experiment are therefore not considered robust enough to be used [32].

Laird *et al.* used the $^{18}\text{Ne}(d,p)^{19}\text{Ne}$ reaction in inverse kinematics to populate states in ^{19}Ne [55]. The excitation in ^{19}Ne was given by the energy of the emitted proton. The low beam intensity (10^6 pps), the low cross section of the transfer reaction, the background from fusion evaporation reactions on the carbon (and to some extent, deuterons) in the target and the low α -particle branching ratios of the states of interest means that only upper limits of 0.01 for the branching ratios of the 4033-, 4140- and 4197-keV states can be given. This experiment was performed in inverse kinematics due to the radioactive nature of the ^{18}Ne meaning that the energy resolution of this experiment is consequently poor and separation of the various states is not possible.

Dauids *et al.* used the $^{21}\text{Ne}(p,t)^{19}\text{Ne}$ reaction with a 42 MeV/u ^{21}Ne beam to populate the relevant resonances at KVI using the Big-Bite spectrometer at 0° [56, 57]. In this experiment, ^{19}Ne or ^{15}O heavy recoils produced in the reaction is measured at the focal plane along with the tritons that are also produced. Measurement of the triton energy gives the level populated in ^{19}Ne . The focal plane uses a phoswich to detect the heavy ions with drift chambers placed behind the phoswich. The background in the $^{19}\text{Ne}+t$ coincidence spectrum is lower than that of the $^{15}\text{O}+t$ spectrum, as there are fragmentation reactions which can produce a ^{15}O recoil and a triton but which cannot produce a ^{19}Ne recoil and a triton. In common with a number of other studies of the α -particle branching ratio, this experiment is unable to resolve the 4140/4197-keV doublet due to the poor energy resolution of the experiment (90 keV, FWHM). In fact, this study makes no effort to attempt to quantify the possible contribution of the doublet to the total reaction rate.

¹In fact, Ref. [53] does not report any results for α -particle branching ratios for the lowest three states, i.e. those relevant to this thesis.

State / keV	Ref. [55]	Ref. [56,57]	Ref. [46]	Ref. [58]
4033	< 0.01	$< 4.3 \times 10^{-4}$	$< 6 \times 10^{-4}$	$(2.9 \pm 2.1) \times 10^{-4}$
4140	< 0.01			$(1.2 \pm 0.5) \times 10^{-3}$
4197	< 0.01			$(1.2 \pm 0.5) \times 10^{-3}$

Table 3.3: Previous measurements of α -particle branching ratios in ^{19}Ne for the first three states above the α -threshold. Boxes are left blank for those references for which no information is given for that state. Refs. [53,54] have been omitted as neither reports α -particle branching ratios for these states. The doublet is not resolved in Ref. [58] and the branching ratio reported is a combination of these two states.

Rehm *et al.* used the $^{20}\text{Ne}(^3\text{He},\alpha)^{19}\text{Ne}$ reaction in inverse kinematics using a silicon $dE - E$ telescope (α -particles) with an Enge magnetic spectrometer (^{19}Ne and ^{15}O heavy recoils) [46]. In this case, a gas cell filled with ^3He was used as a target. The energy resolution in this experiment is extremely poor (a Q -value resolution of about 220 keV, FWHM) which makes extraction of α -particle branching ratios for the lower-lying states extremely difficult due to overlapping events from higher-lying states. No results are reported for the branching ratios of the doublet.

Tan *et al.* used the $^{19}\text{F}(^3\text{He},t)^{19}\text{Ne}$ reaction in normal kinematics [31,58]. The TWIN-SOL system of soilnoidal magnets was used to transport reaction tritons to a silicon $dE - E$ telescope. Decay α -particles were detected in an array of 300- μm thick silicon pad detectors within the reaction chamber. The energy resolution in this experiment is too poor to resolve the doublet. In addition, the background in this experiment is high and some authors [32] have expressed concerns over the α -particle branching ratios extracted from this experiment due to this. This experiment is discussed in more detail in chapter 9.

Table 3.3 shows a summary of known α -particle branching ratios.

Of all of the previous experiments which have studied this reaction, only [53,54] two have had energy resolutions that were good enough to separate the doublet in ^{19}Ne and neither of them reported α -particle branching ratios for the lowest three states above the threshold. Without being able to properly separate the various states in ^{19}Ne , proper quantification of the α -particle branching ratios is not possible due to the stronger states overlying the weaker ones and hiding the corresponding events.

3.4.5 Relative influence of the astrophysical states

Though the rate will likely be dominated by the 4033-keV resonance, it is worth considering for a moment the contribution of the 4140- and 4197-keV resonances to the reaction rate

relative to that of the 4033-keV resonance. For the purpose of this calculation, both resonances have been assumed to be $7/2^-$.² Using the equation for the rate given in eq. (2.24) it is possible to calculate the ratio of the reaction rates for the resonances as a function of the ratio of spectroscopic factors of the resonances. In this case, the $\Gamma_{\alpha,sp}$ have been calculated using eq. (2.4) with $R = 5.5$ fm [58] and are found to be $123 \mu\text{eV}$ for the 4033-keV resonance, $5.61 \mu\text{eV}$ for the 4140-keV resonance and $28.2 \mu\text{eV}$ for the 4197-keV resonance. This leads to, at 0.4 GK, the ratio of the rates being given by:

$$\langle\sigma v\rangle_{4140}/\langle\sigma v\rangle_{4033} = 4.09 \times 10^{-3} S_{\alpha,4140}/S_{\alpha,4033} , \quad (3.1)$$

and

$$\langle\sigma v\rangle_{4197}/\langle\sigma v\rangle_{4033} = 3.93 \times 10^{-3} S_{\alpha,4197}/S_{\alpha,4033} . \quad (3.2)$$

In both cases, if the S_{α} for the $\ell = 4$ 4140- and 4197-keV α -cluster resonances are around 25 times of that for the 4033-keV resonance, then the contribution of the $\ell = 4$ resonances will be around 10% of that of the 4033-keV resonance at 0.4 GK. Unless and until the possibility of the $\ell = 4$ resonances contributing to the total rate on a similar scale to the 4033-keV resonance can be discounted, experiments studying the α width of these states should be designed such that the $\ell = 4$ resonances are separable.

3.5 The planned $^{15}\text{O}(^6\text{Li},d)^{19}\text{Ne}$ study with SHARC/TIGRESS

An experiment is planned at TRIUMF-ISAC using SHARC, a silicon array, and TIGRESS, a high-purity germanium array both of which are described in detail in chapter 4. The α -transfer reaction $^{15}\text{O}(^6\text{Li},d)^{19}\text{Ne}$ will be used to extract α spectroscopic factors of states in ^{19}Ne . The decays of the 4033-, 4140- and 4197-keV states are all dominated by γ -ray emission. TIGRESS will be used to detect the γ rays resulting from the decays of these states; the cross section to these states will allow the α spectroscopic factor to be extracted and the α width calculated.

This experiment must be performed in inverse kinematics due to the radioactive nature of ^{15}O . In addition, a ^6LiF target is required, which can lead to problems with reactions occurring off the ^{19}F in the target. Suppression of these reactions is required in order to be able to observe the channels of interest.

The yield for the states of interest, especially the 4033-keV state in ^{19}Ne , is very low. A thick target can be used to maximise the yield but this will have a corresponding impact on the energy resolution which may be achieved. However, in this experiment, the yield to the 4033-keV state is of interest and this can be found using the superior energy resolution

²If both resonances were assumed to be $9/2^-$, then the corresponding contributions would be 1.25 larger.

of TIGRESS. SHARC can be used to constrain the angular region used in the experiment to where the DWBA calculations may be valid which will assist in calculating the yield.

3.6 Studying the J^π s of resonances in ^{19}Ne using the $^{20}\text{Ne}(d,t)^{19}\text{Ne}$ reaction

An experiment to determine the J^π s of the 4140- and 4197-keV resonances is planned using a ^{20}Ne -implanted target. Branching ratios and transition rates from γ -ray data suggest opposite spin assignments from one another. Therefore, a new method is required if the spin-parities are going to finally be assigned. The experimental details of the test experiment for this are laid out in chapter 7.

In order to constrain these J^π s, the angular distributions of outgoing tritons from the $^{20}\text{Ne}(d,t)^{19}\text{Ne}$ reaction will be used.³ The shapes of the angular distributions gives the ℓ -values transferred in the reaction. The $7/2^-$ resonance is populated by an $\ell = 3$ reaction while the $9/2^-$ resonance is populated by an $\ell = 5$ reaction. The different shapes of the angular distributions of tritons should allow for differentiation between the resonances.

There are a number of experimental considerations in the case of this experiment. First of all, how the implanted targets will react under a high beam current and whether the target backing material can obscure the states of interest. Secondly, the strongly negative Q -value of this reaction makes inverse kinematics unfeasible with the accelerator at Munich. Thirdly, the small separation of the doublet means that it is difficult to separate the states of interest using any charged-particle detector by a magnetic spectrometer. Finally, the small separation of the doublet means that, in inverse kinematics, the states would likely not be separated due to the compression of the kinematic lines and the larger energy losses through the target.

3.7 Direct measurement of the α -particle branching ratios

In addition to the indirect calculation of the α -particle branching ratios, direct measurement is also possible. This can be accomplished by indirect population of the states of interest (via a transfer reactions of some sort ($^{19}\text{F}(^3\text{He},t)^{19}\text{Ne}$, for example) or via inelastic scattering of ^{19}Ne , followed by observation of the subsequent decay into $^{15}\text{O}+\alpha$. In chapter 9, a test for an experiment to measure the α -particle branching ratios of these unbound states in will be discussed. With a branching ratio from this experiment and a total width from lifetime measurements [48, 49], the reaction rate for each narrow resonance can be calculated by using $\Gamma_\alpha = B_\alpha\Gamma$ in eq. (2.24).

³ $^{20}\text{Ne}(^3\text{He},^4\text{He})^{19}\text{Ne}$ is another possibility for this reaction - the possibility of using this instead is also discussed later in this thesis.

The experiment involves the use of a magnetic spectrometer along with silicon detectors in the reaction chamber to probe the branching ratios. In contrast to the previous study by Tan *et al.* [58] the 4140- and 4197-keV doublet are not resolved but a relatively large branching ratio is claimed for these states. It is reasonable in the light of the discussion above to design an experiment in which the doublet can be resolved. It is hoped that these states can be resolved in the spectrometer, which is a major advantage over previous studies. If this is done, the contribution (or lack thereof) of these states to the total reaction rate can finally be resolved.

The experimental requirements for a branching ratio study of this type were discussed above. In all but two experiments, Magnus *et al.* [53] and Visser *et al.* [54] which both used magnetic spectrometers to detect the outgoing tritons from the $^{19}\text{F}(^3\text{He},t)^{19}\text{Ne}$ reaction, the doublet is not resolved and the energy resolution is too poor to be able to confidently separate the states of interest. Therefore, in order to be able to quantify the possible contribution from the doublet compared to the 4033-keV state, the states must all be properly resolved. This rules out the use of an experiment in inverse kinematics, at least until the relative contributions of the three states can be determined, as the energy resolution will be too poor in this case. In the normal kinematics approach used in this proposed experiment, the overall efficiency for the detection of α -particles is lower than in inverse kinematics, but the possible separation of the states means that the contributions from different states can be separated.

Chapter 4

The SHARC/TIGRESS Setup

4.1 Introduction

The planned $^{15}\text{O}(^6\text{Li},d)^{19}\text{Ne}$ measurement using a radioactive ^{15}O beam will be performed at the ISAC facility at TRIUMF, using SHARC, a silicon array, and TIGRESS, a germanium array. In this chapter ISAC, SHARC and TIGRESS are described. There have been a number of changes to the detector setup and to the data acquisition (DAQ) system for SHARC/TIGRESS since the commissioning of the arrays; testing this new DAQ system and the use of the new detector $dE - E$ telescopes forms part of this thesis. The new DAQ setup is also described in this chapter. Testing the DAQ necessitated the creation of a sort code to analyse data from SHARC/TIGRESS, which is also described in the next two chapters.

4.2 TRIUMF-ISAC and radioactive ion beam production

The TRI-University Meson Facility (TRIUMF) is located in Vancouver, Canada. It is one of the world's leading Isotope Separation OnLine (ISOL) facilities for Radioactive Ion Beams (RIB). Production of RIB is a very complex topic, with only the outline of the beam production, acceleration and delivery given in this section. The details of the ISAC facility are taken from the TRIUMF information pages [59].

A 500-MeV proton beam from the TRIUMF H^- ion cyclotron with a current of up to $100\ \mu\text{A}$ was used to bombard a SiC target in a surface ionisation source. The protons cause spallation of the target nuclei into various different nuclides. Ions with a low ionisation potential (such as alkali and alkali earth elements, which are strongly electropositive) will lose an electron to a surface with a high work function. The ions produced can then be extracted using an electric field.

Ions extracted from the ion sources are transported to the Radio-Frequency Quadrupole

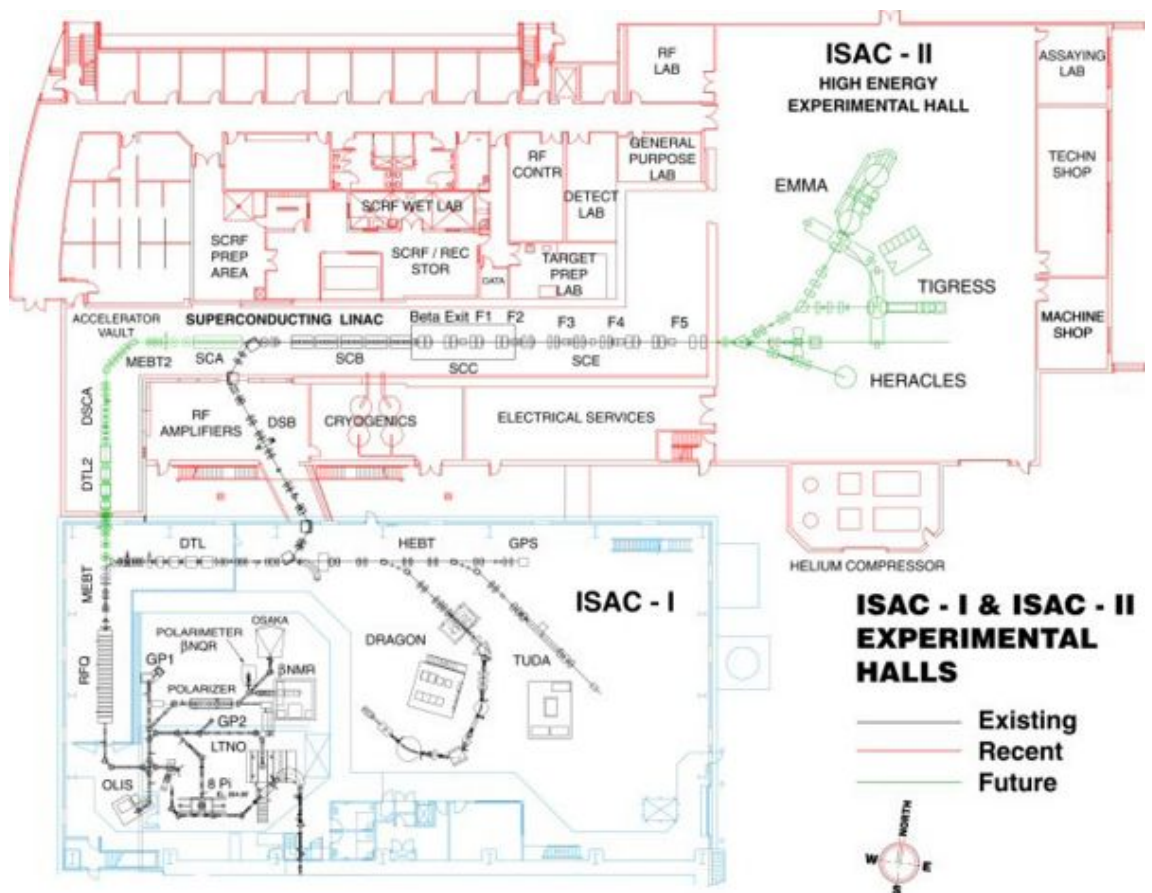


Figure 4.1: Schematic of TRIUMF-ISAC showing the various accelerating stages [60].

(RFQ)¹ in the ISAC-I (Isotope Separation and ACceleration) experimental hall which is designed to accelerate ions with a mass-to-charge ratio of less than 30 from 2 keV/u to 150 keV/u. A RFQ has four vanes with sinusoidal profiles running down the length of each accelerating cavity [61]. A quadrupole field is generated by applying opposite polarity potentials to the four vanes, with the potentials applied varying sinusoidally. This electric quadrupole field focusses the beam in one transverse direction. After half a cycle, the quadrupolar field will focus in the other transverse direction. If one opposite pair of vanes is shifted by half an RF cycle, then a longitudinal electric field is also created, causing acceleration.²

The beam is bunched before the RFQ. The beam from the RFQ has a main peak and two satellite peaks that are removed using a 11 MHz chopper giving pulses separated by 84.8 ns. After the RFQ, a carbon stripper foil is used to obtain higher charge states. The beam is then accelerated again by the Drift Tube Linear accelerator (DTL). A DTL uses a time-varying electric field to accelerate the beam. The drift tubes shield the beam from the periods during which the electric field would cause deceleration. The beam is then steered into the ISAC-II superconducting linear accelerator (SC-LINAC) which takes the beam energy up to 6 MeV/u. The SC-LINAC uses radiofrequency electric fields in each cavity to accelerate the beam; the time variation in the field ensuring that the beam is not inadvertently decelerated. The beam is then steered to the TIGRESS experimental station in the ISAC-II experimental hall.

4.3 Semiconductors as detectors

Both SHARC and TIGRESS use semiconductor devices for measuring energy deposition, silicon and germanium respectively. The mechanism of how semiconductors can provide a measurement of energy deposition is described in this section.

Electrons in semiconductors can exist in one of two energy bands: the valence band and the conduction band. The first of these comprises the outer electrons fixed to points within the crystal, the second comprises the electrons which can move through the crystal. The bandgap is the energy which separates the two bands. If an electron in the valence band receives energy from an incoming photon or charged particle, then it can be promoted to the conduction band, becoming free to move in the crystal. The promotion of an electron leaves a hole behind, a gap into which another electron can move. Under the influence of an electric field, electrons and holes will move in opposite directions, and this movement of charge [62] will produce a measurable signal on the contacts with the semiconductor.

Electron-hole pairs can be destroyed by recombination, when an electron moves from the conduction band to the valence band filling a hole. This loss of charge carriers can

¹Figure 4.1 is included to allow the reader to follow the different acceleration stages.

²An small animation showing this can be found at: http://www.triumf.info/wiki/exp-prog/index.php/Radio_frequency_quadrupole

result in an incomplete energy being recorded for the detector. In order to reduce the possibility of this effect, the collection time for the signal should be minimised. This is equivalent to maximising the drift velocities of the charge carriers. The drift velocities of the electrons and holes depend on the electric field strength; for the high fields used in semiconductor detectors, the drift velocity saturates, usually at a value of around 10^7 cm/s [62].

In order to achieve a high electric field strength, semiconductor detectors are made of two doped materials. Doping artificially increases or decreases the number of electrons in the conduction band. For silicon, a Group IV element, each atom bonds with 4 others in the crystal. Doping the silicon with a Group V element, such as phosphorus, results in more electrons being available in the system. This is an n-type semiconductor. Doping with a Group III element, such as boron, will result in extra holes being created as charge carriers, making a p-type semiconductor. Combining a p-type and an n-type semiconductor into one system creates the semiconductor junction. In this system, the n-type side has a high concentration of electrons and the p-type has a high concentration of holes, and a resulting low concentration of electrons. Electrons therefore flow from the n-type to the p-type semiconductor where they combine with the holes. A Group V element which has donated an electron will remain as a positive ion in the n-type semiconductor (and a similar negative ion will be created by an electron combining with a hole at a Group III element in the p-type semiconductor) resulting in an electric field being created over the junction between the p- and n-type semiconductors. A depletion region is created in the semiconductor where the electrons and holes have recombined and an electric field has been created which will result in electrons and holes moving in opposite directions in the depletion region. If the voltage on the p-type semiconductor is made negative with respect to the voltage on the n-type semiconductor, electrons flow from the n-type to the p-type semiconductor again creating a larger depletion region with a higher field.

4.4 Scintillators as detectors

Scintillators convert the energy deposited in them by charged particles into light. There are a great number of different scintillators with different properties (energy resolution, stopping power, light yield etc., a complete list of important properties may be found in Ref. [62]) with the experimental requirements guiding the choice of scintillator. The photons emitted from the scintillator are collected by a light-guide and subsequently to a photomultiplier tube (PMT). At the photocathode in the PMT, electrons are produced by the incident photons via the photoelectric effect. A bias applied through the PMT causes the photoelectrons to accelerate. When these electrons are incident on the next dynode, they cause a much larger number of electrons to be ejected, and the process repeats. After a number of these stages (typically there are around 10 dynodes in commercially-available

PMTs [62]), there are enough electrons to cause a detectable signal at the anode.

4.5 SHARC

SHARC (Silicon Highly-segmented Array for Reactions and Coulex) is an array of silicon detectors. SHARC was designed to fit inside TIGRESS while still allowing TIGRESS to be close to the target position and so that the signals from SHARC could be fed into the TIGRESS DAQ. It can investigate a wide range of different nuclear physics processes (single-nucleon transfer, cluster transfer, fusion-evaporation, coulex, inelastic and deep-inelastic scattering) at a wide range of energies, with good energy and angular resolution, and a high angular coverage. The silicon detectors used in SHARC are introduced first. A schematic diagram of SHARC (fig. 4.6) is provided in the following section along with an introduction to the full array.

4.5.1 Silicon detectors

Silicon is one of the most commonly used semiconductor detectors and a large number of different varieties are available in a range of thicknesses and geometries. In addition, unlike germanium, the bandgap in silicon is large enough (1.12 eV [62]) that the detectors do not need to be cooled. Charged particles (nuclei or electrons) passing through the detector cause ionisation which manifests in the promotion of electrons to the conduction bands. These electrons, and the holes created when the electrons are promoted to the conduction band, move in opposite directions under the influence of the reverse potential difference applied to the detector. This motion of charge carriers causes signals to be induced on the metalised contacts on each surface of the detector.

In table 4.1 are set out the particulars of the various different silicon detectors used in SHARC. Diagrams of the SHARC detectors can be found in figs. 4.2 to 4.5. The MSX-35 and QQQ1 detectors do not have strips, these are referred to in the text from here as ‘pad’ detectors. The BB11 and QQQ2 detectors are referred to as ‘strip’ detectors.

Doubled-sided silicon detectors usually consist of a p-type doping (usually doped with boron) on the front (junction) side of the detector, with a n-type bulk and a layer of more heavily doped n⁺-type (usually doped with arsenic or phosphorus) material on the back (ohmic) side of the detector. Electrons created in the bulk of the detector move towards the p-type contact and hole towards the n⁺-type back contact. Strip detectors segment the front and back contacts in order to localise the interaction within the detector. The spatial resolution of strip detectors is limited by the lateral diffusion of the charge produced. This effect is much smaller, however, than the dimensions of the strips used in the SHARC detectors, however.

The p-n junction contact on the front of the detector can be used to form strips for position localisation. In order to ensure that the front strips are electrically isolated, the

Detector Type	Thickness / μm	Active area	Junction strip pitch	Ohmic strip pitch	Junction strips (direction)	Ohmic strips (direction)	Junction Window	Ohmic Window
MSX-35	1500	50 mm x 70 mm	N/A	N/A	N/A	N/A	Gridded	Metal
BB11	140 1000	71.9 mm x 47.9 mm	3 mm	1 mm	24 (ϕ)	48 (approx. θ)	Gridded	Gridded
QQQ1	1000	82° with a radial range of 9 to 50 mm	N/A	N/A	N/A	N/A	Metal	Metal
QQQ2	40 80 1000	82° with a radial range of 9 to 41 mm	2 mm	3.4°	16 (θ)	24 (ϕ)	Metal	Metal

Table 4.1: SHARC detector particulars [63].

front contact is formed from p^+ material implanted within the n -type bulk of the detector. A 200-nm thick SiO_2 layer is used to isolate the front surface. Aluminium contacts of 200 nm separated by oxide strips are placed on top of this oxide layer in order to detect the movement of charges within the silicon.

The ohmic contact uses a similar structure. In this case, the n - n^+ contact is used ensure that electrons from the conduction band in the silicon can move easily into the metalised contact. There are additional problems with the ohmic segmentation, however. The SiO_2 layer used can form positive static charges at the Si-SiO_2 contact which causes electrons to be attracted, creating an electric contact between adjacent strips. This results in the charge produced by an ionising particle being spread over a number of strips making position measurement impossible. In order to prevent this, p^+ implants may be placed between the n^+ implants on the ohmic side of the detector. This increases the resistance between the strips and isolates them from one another again.

The metal contacts on each strip can either cover the whole of each strip or a portion of each strip. The gridded contacts cover around 3% of the total area of the detector. The gridded contacts means that the effective deadlayer of most of the strip is lower and thus there is a lower threshold on the energy of incident particles that can be detected. However, the grid overlaying the strips also means that the deadlayer is not constant across the detector resulting in some small proportion of events which have a higher deadlayer loss and will register a slightly different energy. This effect is small and can be discounted.

Silicon detectors, like all semiconductor detectors, have deadlayers in which the semiconductor is not fully depleted.³ In these areas, the charge created is lost, resulting some energy being missed. In order to use silicon detectors in ‘transmission mode’, that is, with charged-particles passing through the detector as in silicon telescopes (see section 4.5.4, the dE detector must be fully depleted.

Silicon strip detectors can also suffer from crosstalk. This crosstalk can be due to diffusion of charge between strips or due to other effects such as capacitive coupling between strips - this occurs when charges moving in strips or wires induce moving charges in adjacent strips. Corrective action for crosstalk can be made by suppressing events with multiple-strip events in the silicon detectors or by using addback algorithms between adjacent strips. Corrective action is not required for the energy calibration caused by crosstalk (unless, as described later in this thesis, it changes over a strip) as this is intrinsic to the calibration (i.e. if a certain portion of charge is lost in each event then the calibration will already include this effect).

³In germanium detectors, the γ ray interacts within the detector so thin deadlayers around the edges have little effect.

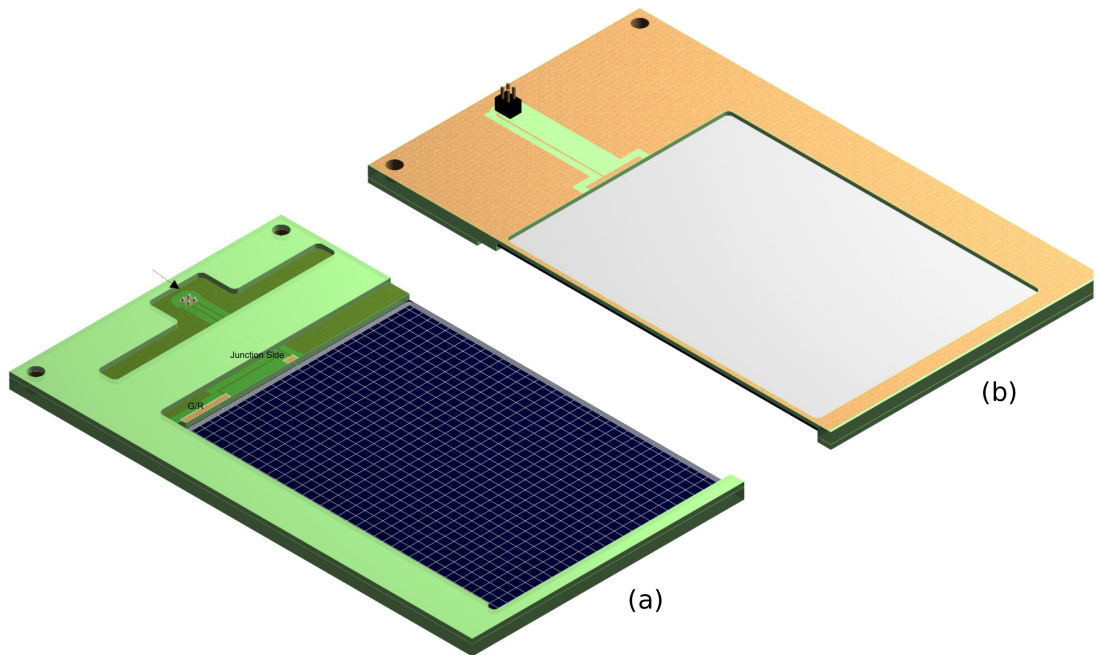


Figure 4.2: A diagram of a MSX-35 detector. The junction side (a) of the detector has a gridded contact. The ohmic side (b) with the planar metal contact and the 4-pin connector [63].

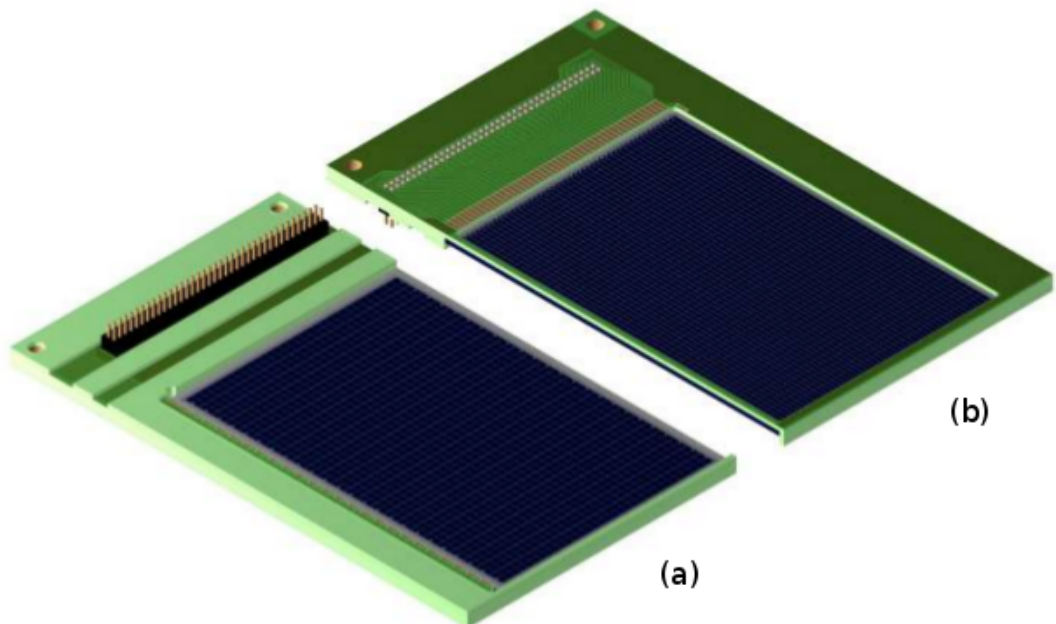


Figure 4.3: A diagram of a BB11 detector. Both junction (a) and ohmic (b) sides are gridded, as 140- μm BB11 detectors are used as part of dE-E telescopes [63].

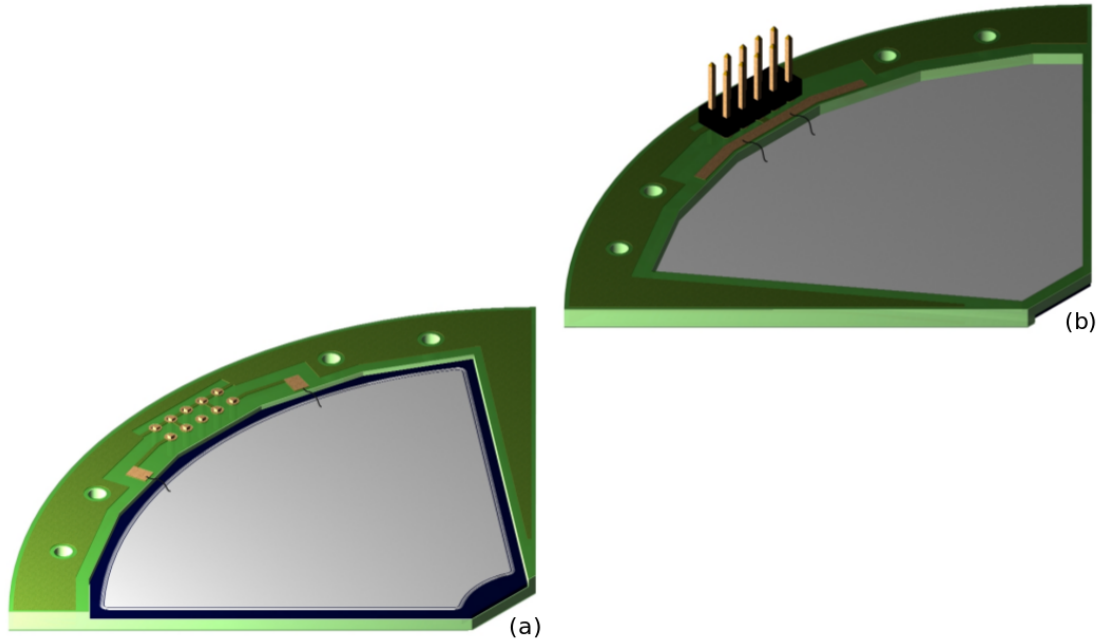


Figure 4.4: A diagram of a QQQ1 detector. Both the junction (a) and ohmic (b) sides of the detector have metal contacts. The 5 by 2 connector uses the 5 pins closest to the detector for detector connections, the outer 5 pins are connected to the PCB ground plane. The pins are junction (guard ring), ground, ohmic, ground, junction (detector face) [63].

4.5.2 The array

SHARC consists of two ‘boxes’ and two ‘CDs’, one of each upstream and downstream of the target position. The detectors are mounted on metal brackets which are attached to the flange. In addition to these detectors, there is a target fan and mechanism through the flange allowing for a number of targets to be installed simultaneously and changed from outside the chamber. The flange is made from steel, the vacuum chamber into which it is placed is constructed from aluminium to minimise the attenuation of γ rays.

The SHARC box detectors fit together in a ‘windmill’ arrangement. This compact setup allows for high angular coverage, and increases the physical stability of the detector array. In fig. 4.3, a slot can be seen in the PCB between the wafer and the connector, this slot accommodates the PCB for the next detector in the windmill.

The detectors used in the experiment described in the next chapter and their properties are summarised in table 4.2.⁴ Dummy detectors are required when a real detector is not in place to preserve the structural stability of the windmill of box detectors.

⁴For detectors 2651-[A-D], the link between the original documentation and the detectors has been lost. All are assumed to be 1000 μm thick.

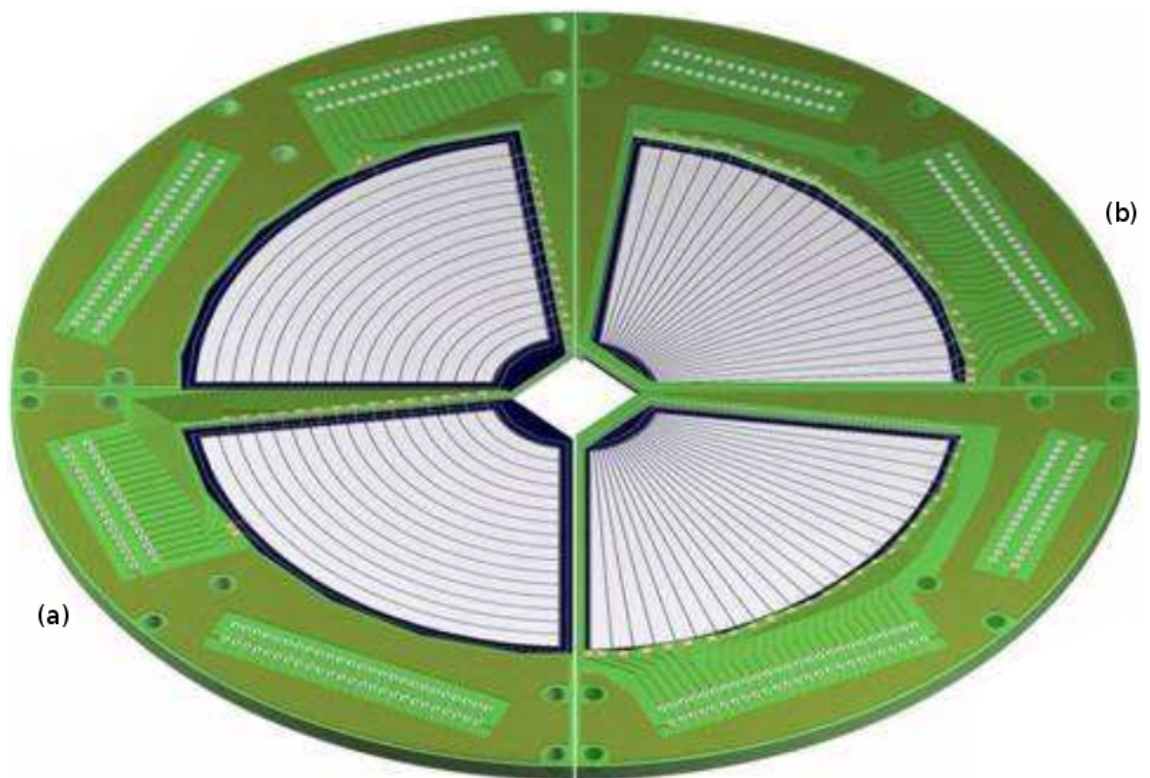


Figure 4.5: A diagram showing four QQQ2 detectors arranged to make a full CD. The junction side (a) is separated into rings (θ) and ohmic side (b) is separated into segments (ϕ). Both sides use full metal contacts. The connectors for these detectors are not shown [63].

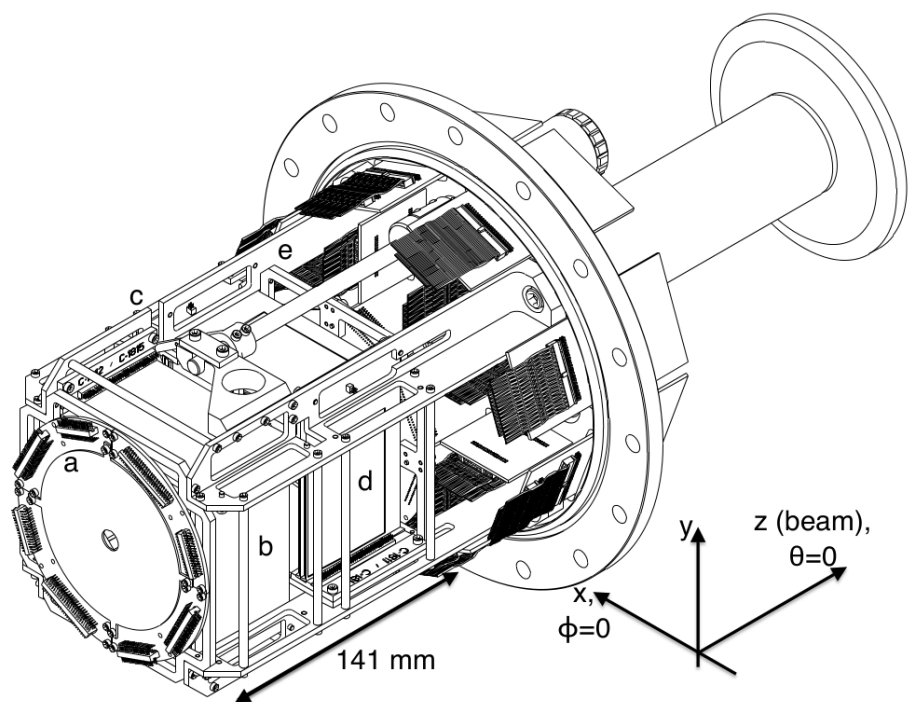


Figure 4.6: A schematic of a fully instrumented SHARC with the upstream CD (a), upstream box (b), target holder (c), downstream box (d) and downstream CD (e — mostly hidden by the downstream box). The target holder (c) supports the target rotary upon which the target fan is mounted. [64].

Serial Number	Position	Type	Thickness / μm	Bias / V	Typical Leakage Current / μA
2232-2	Downstream CD 1	Strip	40	3.5	0.017
2645-6	Downstream CD 2	Strip	79	15	0.029
2645-7	Downstream CD 3	Strip	79	15	0.028
2645-4	Downstream CD 4	Strip	80	15	3.280
Dummy	Downstream Box 1	Strip	N/A	N/A	N/A
2624-9	Downstream Box 2	Strip	133	40	1.944
Dummy	Downstream Box 3	Strip	N/A	N/A	N/A
2624-3	Downstream Box 4	Strip	141	40	2.170
2624-7	Upstream Box 1	Strip	143	40	1.691
2624-4	Upstream Box 2	Strip	142	30	1.481
2624-6	Upstream Box 3	Strip	143	20	0.391
Dummy	Upstream Box 4	Strip	N/A	N/A	N/A
2651-D	Upstream CD 1	Strip, no pad	1000	100	0.230
2651-C	Upstream CD 2	Strip, no pad	1000	80	0.217
2651-B	Upstream CD 3	Strip, no pad	1000	100	0.223
2651-A	Upstream CD 4	Strip, no pad	1000	100	0.229
2651-12	Downstream CD 1	Pad	993	100	0.294
2651-4	Downstream CD 2	Pad	994	100	0.296
2651-11	Downstream CD 3	Pad	999	100	0.274
2651-5	Downstream CD 4	Pad	992	100	0.260
Dummy	Downstream Box 1	Pad	N/A	N/A	N/A
2754-9	Downstream Box 2	Pad	1535	375	2.310
Dummy	Downstream Box 3	Pad	N/A	N/A	N/A
2754-2	Downstream Box 4	Pad	1531	150	1.123
2754-1	Upstream Box 1	Pad	1535	240	1.085
2754-2x	Upstream Box 2	Pad	1535	330	2.840
2754-8	Upstream Box 3	Pad	1534	260	1.748
Dummy	Upstream Box 4	Pad	N/A	N/A	N/A

Table 4.2: SHARC Detectors used. The upstream CD was a single layer of segmented QQQ2s so there are no corresponding pads to these detectors.

4.5.3 Instrumentation: preamplifiers and DAQ modules

Signals from SHARC are passed through the flange by shielded PCB feedthroughs which carry signals, grounds and guard ring connections for the detectors. All feedthroughs are glued into the flange using an insulating epoxy covered in black lacquer to prevent light entering the chamber [65]. Signals are carried from the feedthroughs to the preamplifiers by ribbon cables fed through the middle of grounding braid wrapped in kapton tape. The grounding braid was attached to the metal plates used to shield the preamplifiers.

ATSD-II charge-sensitive preamplifiers were used for the SHARC detectors. The preamplifiers have 32 channels and selectable gain, the latter is a requirement given the range of uses for which SHARC is designed, with a rise time of 100 ns and decay time of 10 μ s.

In addition to the preamplifiers, there are separate high-voltage filter boards. There are two different HV boards in use - a 32-channel board which applies the same bias to all channels, and a 4-channel board which allows for up to four different pad detectors to be instrumented simultaneously. Bias voltages for pad detectors are usually much higher than for strip detectors so the 4-channel HV boards must be able to cope with biases of up to 400 V. To instrument a QQQ2, only two preamplifiers are required: one for the front of the detector, and one for the back. For BB11s, two preamplifiers are required for the 48 back strips and one is required for the 24 front strips. Stacks of 2 or 3 preamplifiers (depending on the detector) were constructed with aluminium grounding plates between each preamplifier and on either side of the stack. These grounding plates are attached to the TIGRESS ground by grounding braid. Each preamplifier board is fed into one mezzanine of a TIG-64 module; these modules are discussed in more detail in section 4.8. The preamplifier stacks are mounted around the downstream beamline from SHARC, in the position where the 45° ring of TIGRESS clovers would sit. The signals from the preamplifier stacks are carried to the DAQ system in an air-conditioned shack by SCSI-V cables.

4.5.4 Particle identification using differential energy loss

In this experiment, particle identification was performed using the $dE - E$ method with pairs of silicon detectors. For non-relativistic particles, the energy loss per unit length can be expressed as [62]:

$$-\frac{dE}{dx} = \frac{4\pi e^4 z^2}{m_e v^2} N Z \ln \left(\frac{2m_e v^2}{I} \right) \quad (4.1)$$

where z is the charge number of the incident ion, v is the velocity of that ion, e is the electronic charge, N is the number density of the absorber ion and Z is the atomic number of the absorber ion, and m_e is the electron mass. I is an experimentally determined value which describes average ionisation potentials and excitations which need not be further

discussed.

The velocity dependence of equation 4.1 is dominated at low energies by the $\frac{1}{v^2}$ term. Taking the non-relativistic expression for the kinetic energy, this suggests that the energy loss for non-relativistic particles should vary as:

$$-\frac{dE}{dx} \propto \frac{mz^2}{E} \quad (4.2)$$

From this, the relative energy deposition in each detector can be estimated. The z^2 term suggests that particles of higher charge should deposit more energy than particles of lower charge (assuming the same velocity). Considering tritons and ^3He for simplicity: for the same energy, the triton will deposit less energy in the first detector relative to the ^3He , and therefore the triton deposits more energy in the E detector. Particles can then be identified by considering the relative energy loss in each detector; ^3He ions deposit more energy in the dE and less in the E detector than tritons.

In addition, massive species will deposit more energy in the dE detector. This allows for discrimination between different species with the same proton number e.g. protons, deuterons, and tritons.

4.6 γ -ray interactions

Before discussing TIGRESS, it is beneficial to discuss the ways in which γ rays interact in detectors and produce ionisation. The mechanisms differ from those of charged particles and create additional complications that must be considered. Charged particles deposit energy along their path by numerous interactions with electrons, each of which transfers a small amount of energy. γ rays scatter infrequently from electrons while often transferring a large amount of energy when they do interact. There are three main modes of γ ray interaction: photoelectric absorption, Compton scattering and pair production. γ rays interacting within the detector by these three processes will cause electrons (as well as, in the case of pair production, positrons) to recoil through the detector causing more ionisation to take place. It is this ionisation that is detected, not the direct absorption of the γ ray.

Photoelectric absorption

In photoelectric absorption, an electron is excited out of an atom due to the absorption of a γ ray. This process is predominant for low energy γ rays and the probability of interaction rises approximately as $Z^{4.5}$ [62]. For high-purity germanium (HPGe) detectors, photoelectric absorption dominates for γ rays of below around 100 keV [66].

Compton scattering

Compton scattering is the process in which a γ ray scattering off an electron in the absorbing material, transferring energy to the electron in the process as shown in fig. 4.7. A γ ray of initial energy E_γ scattered through an angle θ will have an energy, E'_γ , given by:

$$E'_\gamma = \frac{E_\gamma}{1 + \frac{E_\gamma}{m_e c^2} (1 - \cos \theta)} \quad (4.3)$$

where $m_e c^2$ is 511 keV, the rest mass of the electron. The scattered electron causes secondary ionisation as it moves through the absorber material, resulting in the detector measuring the energy of the scattered electron. However, in Compton scattering, the γ ray must always take away some energy and so, if the scattered γ ray is not stopped within the detector, the full energy of original γ ray will not have been fully deposited within the detector. This results in the ‘Compton continuum’ the range of possible energies which can be deposited by a γ ray. The probability of Compton scattering in the absorber depends on the number of electrons available for scattering, and so linearly increases with the atomic number, Z [62].

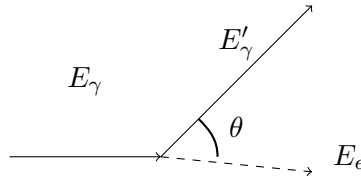


Figure 4.7: Compton Scattering

Pair production

For high-energy γ rays, pair production is also possible. A minimum energy of 1022 keV ($2m_e c^2$) is required to produce an electron-positron pair though the probability of pair production increases strongly with energy. Pair production must take place within the Coulomb potential of a nucleus as pair production *in vacuo* is forbidden. The electron and positron can both travel within the nucleus and cause secondary ionisation. The positron will annihilate upon coming to a stop, producing two back-to-back 511-keV γ rays. One or both of these γ rays can escape the detector, producing the single- and double-escape peaks, 511 keV and 1022 keV below the full-energy peak respectively. The interaction probability for pair production increases approximately with the square of the atomic number [62].

4.7 TIGRESS

In TIGRESS, HPGe crystals are combined into clovers, where a number of crystals are placed together, increasing the total efficiency. When SHARC and TIGRESS are used together, a maximum of twelve clovers can be used. This is because the SHARC preamplifiers sit around the downstream beamline where the 45° ring of TIGRESS clovers would sit. In this experiment, eleven clovers were in place with seven detectors in the 90° ring and four in the 135° ring; one of the detectors in the 90° ring had to be removed from the analysis, however, as the script that set the DAQ mapping had an error which resulted in double-mapping of certain channels. Figures 4.8 and 4.9 show the North hemisphere of TIGRESS.

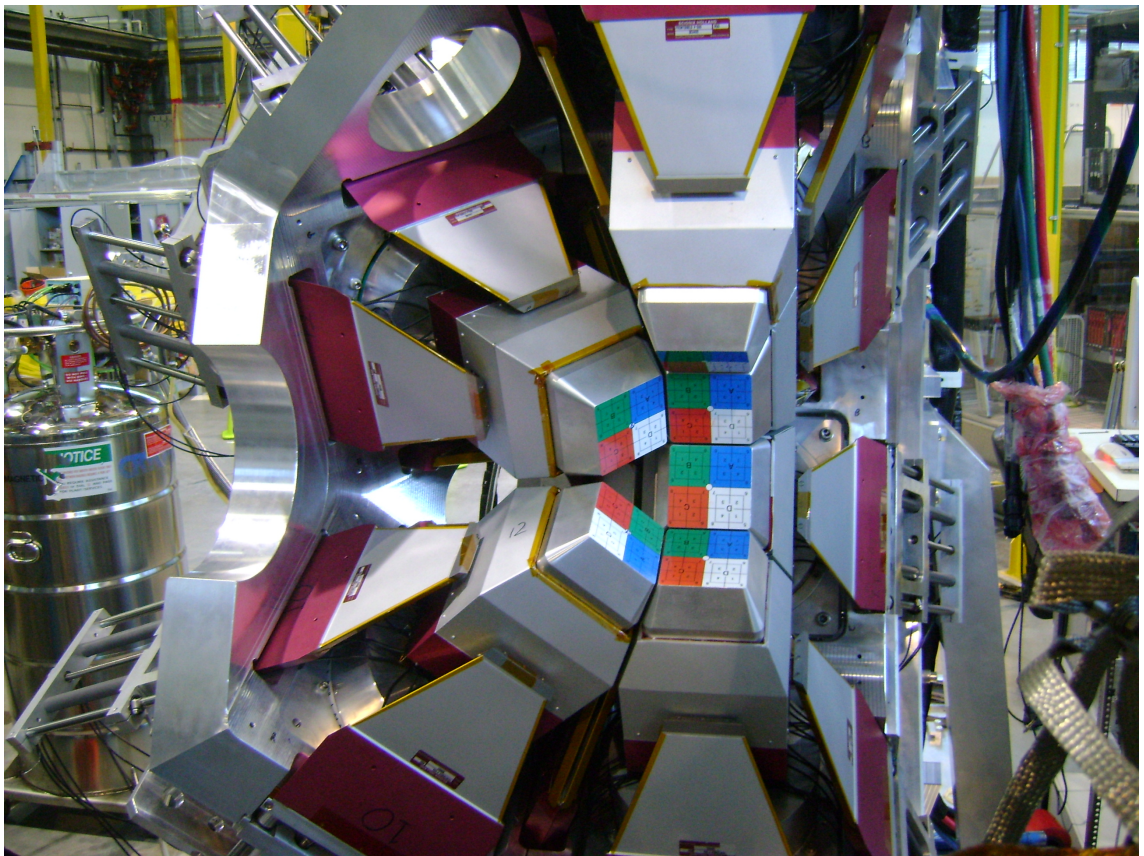


Figure 4.8: The North hemisphere of TIGRESS in high-efficiency mode - the HPGe detectors are wound in and the BGO suppressors are wound back. The beam enters from the left. Note the lack of a downstream ring of detectors. The different crystal and segment positions are marked on the front face of the detector, fig. 4.9 shows this in more detail.

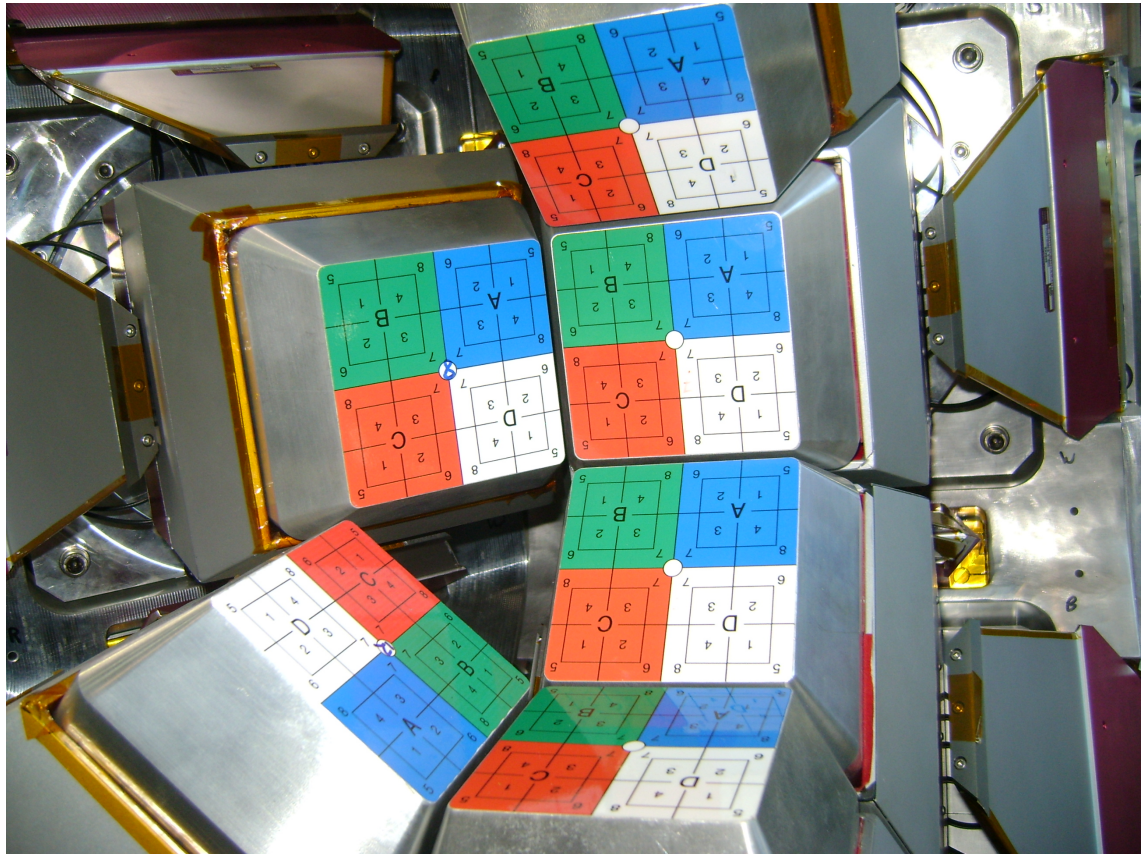


Figure 4.9: Close-up of the North hemisphere of TIGRESS (beam entering from the left). Crystal and segment positions are marked on the front face of the detector. Note the rotated clover in position 16 (lower left clover). Blue and White crystals should be at lower θ , with $\theta = 0$ horizontally right in this picture. The lower-left clover has Blue and Green crystals at lower θ . This is corrected in the analysis code.

4.7.1 TIGRESS detectors

The TIGRESS clovers consist of four segmented closed-end coaxial n-type germanium crystals. The crystals are labelled Blue, Green, Red and White where Blue and White are at lower θ and Blue and Green are at greater ϕ . Each crystal is segmented on the outer contact longitudinally and into front and back sections, giving eight segments per crystal. This segmentation can be seen in fig. 4.9. In addition, the inner contact of each crystal is read out. This gives 36 separate signals per clover. Each crystal has a nominal operating voltage of 3500 V [67].

A diagram of a TIGRESS clover is shown in fig. 4.10. Each TIGRESS detector has a diameter of 60 mm and a length of 90 mm. The z-segmentation is at 31 mm from the front face of the crystal [67]. Each crystal is tapered towards the front to allow for the detector to pack more tightly around the target.

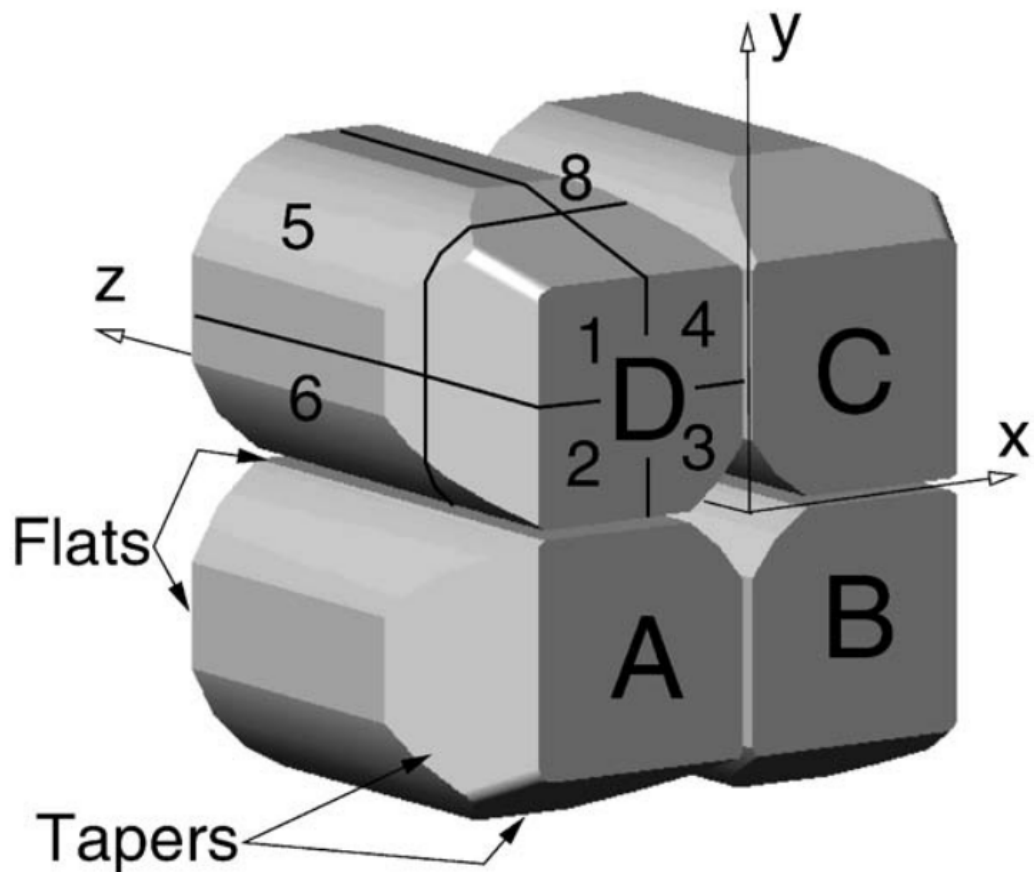


Figure 4.10: A TIGRESS Clover [67]. The origin of the clover coordinates are at the centre of the front face of the cryostat.

In a coaxial n-type detector, electrons move towards the core of the detector. This

core contact is used for the energy measurement of the γ rays as this signal is not split; the segmented outer contacts will only record a proportion of the total energy each. In addition, the outer contact of each crystal is segmented to allow for localisation of events within the crystal. If waveforms are stored, this can be done by using the shapes of the signals detected on the segmented contacts, giving a localisation to better than 2 mm position sensitivity [68]. If waveforms are not stored, the localisation is taken to be from a particular segment based on the total charge collected in each segment. The process by which this is done in this thesis is described in section 5.3.2.

4.7.2 Add-back

In arrays of HPGe detectors, γ rays which do not deposit their full energy in one detector may scatter into another detector. The total energy of the γ ray can then be reconstructed by adding the energies of the two events together. The use of clovers increases the total efficiency relative to having the same number of single detectors, as Compton events which occur in one crystal and scatter into another are easily identified. Segmented crystals allow for more discrimination as to which events are due to Compton scattering [65]. Details of the add-back algorithms which have been tested with TIGRESS can be found in Schumaker *et al.* [69] while the add-back scheme used in this work is discussed in section 5.3.2.

4.7.3 Suppressors

Add-back can reduce the Compton continuum (and escape peaks) and recover the total energy for events. However, this depends on the scattered γ ray hitting and being totally absorbed in another HPGe crystal. If the scattered γ ray is detected leaving the HPGe crystal, then the event can be identified as one for which the total γ -ray energy will not have been collected, allowing the event to be rejected. Detectors with a high probability of causing the scattered γ ray to interact are used for this purpose. Bismuth Germanate (BGO - $\text{Bi}_4\text{Ge}_3\text{O}_{12}$), a scintillator the principle of operation of which is described in section 4.4, is often used for this purpose as the high density of the crystal and high atomic number of bismuth ($Z = 83$) result in a very high probability of interaction per unit volume [62].

TIGRESS can be used in one of two main suppression modes. The first, high-suppression, uses the suppressors wound forwards with the HPGe clovers wound back. This makes undetected scattering out of the clovers less likely and reduces the Compton background. The second, high-efficiency, uses the HPGe clovers wound forwards with the suppressors wound back. In this case, the chance of failing to detect a scattering γ ray is much higher, but with the clovers closer to the target position, the total efficiency is higher. In this experiment, the high-efficiency mode was used. The suppression scheme used in this work is discussed in section 5.3.2, while the suppression schemes tested with TIGRESS may be

found in [69].

4.7.4 Instrumentation: preamplifiers and DAQ modules

Each TIGRESS HPGe segment is instrumented by a separate preamplifier. Unlike the case with SHARC, each preamplifier is on a separate board, mounted within the back of the detector casing. Each clover requires 36 preamplifiers (core and eight segments per crystal for four crystals). All preamplifiers have 100 mV/MeV negative-going signals [65].

4.8 The TIGRESS DAQ

The TIGRESS DAQ must be able to cope with a large number of channels⁵ being read out simultaneously. In addition to this, the large range of experiments that can be performed with TIGRESS requires a flexibility in the triggers available for use in the DAQ. Details of the TIGRESS DAQ and trigger system can be found in Martin *et al.* [70] and are briefly summarised here for completeness. In contrast to the TIGRESS DAQs used previously [65], the system used in the experiment in this thesis used TIG-64s (64 channels per module in two mezzanines of 32) to instrument the SHARC detectors (for the first time) as well as pre-existing TIG-10s (10 channels per module) for TIGRESS.

The DAQ consists of front end (FE) modules and collector (COL) modules. FE modules sample the rise-time region of incoming charge signals at 100 MSPS (mega-samples per second) in order to convert the exponentially-decaying incoming pulses into rectangular pulses by moving window deconvolution. Moving window deconvolution allow correction for the ballistic deficit [62, 70] and enables the DAQ to deal with higher rates.

If the k th data sample is denoted as D_k , the moving window length is L samples, and τ is the decay constant of the exponential pulse in units of the number of samples, then the k th point in the transformed sequence is:

$$F_k = D_k - D_{k-L} + \frac{1}{\tau} \sum_{i=1}^L D_{k-i} \quad (4.4)$$

The $D_k - D_{k-L}$ is the differentiation term that cancels a DC baseline while the summation term removes the exponential tail leaving a tophat function. This attenuates the low frequency component of the noise. Higher frequency noise components can be removed using another filtering (a ‘boxcar’ filter), this time of the form:

$$G_k = \frac{1}{K} \sum_{i=0}^{K-1} F_{k-i} \quad (4.5)$$

⁵SHARC can only be used with 12 TIGRESS clovers - if SHARC was instrumented completely as dE-E telescopes and all 12 possible TIGRESS clovers were being used, there will be 1376 channels excluding any ancillary detectors or scalar readouts from scintillators for beam monitoring

where K is the number of samples to be used in the moving average window.

For an ideal exponential pulse with zero rise time and an exponential decay of time constant τ , G_k takes the form of a trapezoid with rise time K , a flat top of length $L - K$ and a fall time of K . For the ideal signal, all points on the top of the pulse are measures of the total charge collected in the pulse. In the TIGRESS DAQ, in order to remove any bias produced by noise, the evaluated charge is taken at a pre-determined time after the beginning of the pulse [70].

Both TIG-10s and TIG-64s perform this digitisation of the incoming signals. Within these modules, there are sub-event collectors denoted as ‘COL-Channel’. The purpose of this COL-channel module is to merge the incoming data streams into a single stream. A TIG-10 consists of 10 front-end modules and one COL-channel module. Each COL-channel connects to a TIG-C module performing the role of a ‘COL-Slave’. These COL-Slave modules are each connected to the COL-Master module (also a TIG-C module but in a different configuration). The COL-Slave modules contain the basic trigger logic, telling the COL-Master when triggering conditions in the COL-Slave’s COL-Channel modules have been satisfied. The actual trigger for each channel is a leading edge discriminator - when the input voltage goes over a certain threshold, the channel is considered triggered. This leading edge discriminator is not used to give timing information, this information is instead drawn from a constant fraction discriminator (see below). The COL-Master then considers which COL-Slaves have given triggers and whether the triggers given satisfy the master trigger (e.g. a Si- γ coincidence would have required a trigger from one of the germanium channels and one of the silicon channels within the DAQ window of ± 500 ns). If the master trigger is satisfied, the COL-Master arms the DAQ by sending a signal to each COL-Slave, which cause them to collect the information being sent up by the COL-Channel modules. A diagram taken from Ref. [70] is provided to illustrate the above description in fig. 4.11.

4.8.1 Constant fraction discrimination

In order to suppress the background from the decay of scattered beam and the environment further, timing correlation between different detectors can be required. A constant fraction discrimination-style (referred to from here as ‘CFD’) system was implemented in the TIGRESS DAQ. In contrast to a leading-edge system, where the time for the pulse is taken from where the pulse crosses a fixed discrimination threshold, CFD gets the timing from the point where the signal reaches a constant fraction (usually 10-20% of the total amplitude of the peak). This makes the timing value independent of the amplitude of the pulse and the point-of-interaction within the crystal.

The signals used in the TIGRESS DAQ for analysis of the CFD time are those which result from the moving window deconvolution (the F_k , as described above). Unlike the ideal pulse described above, the leading edge of the exponential pulse has a finite rise time

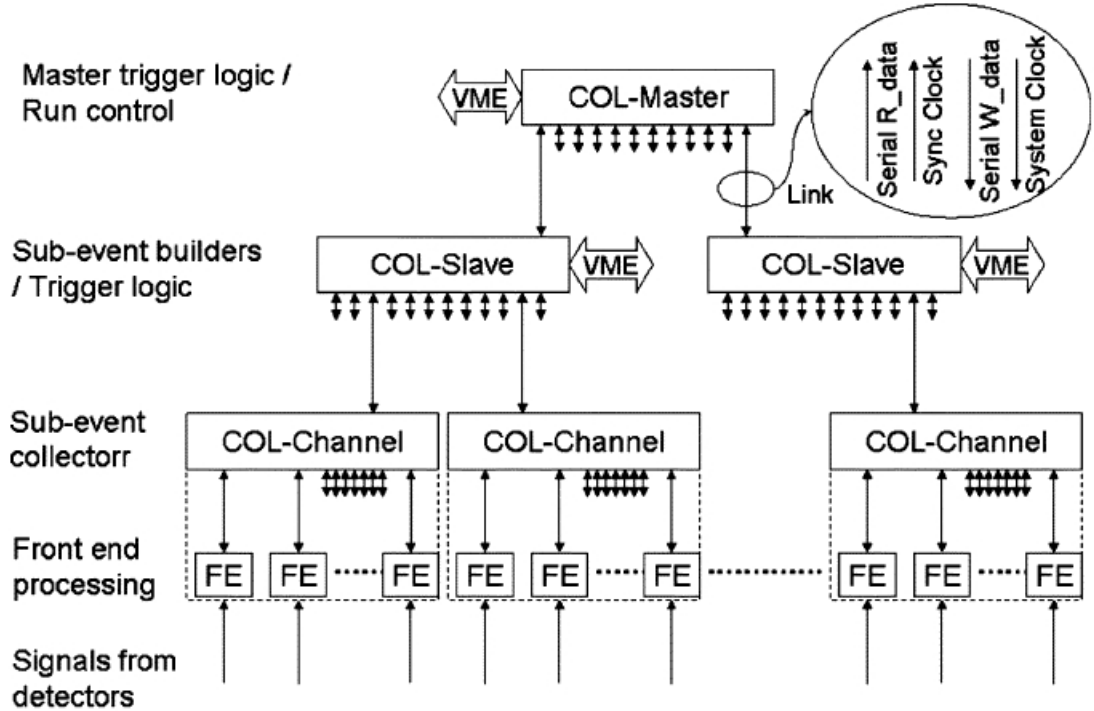


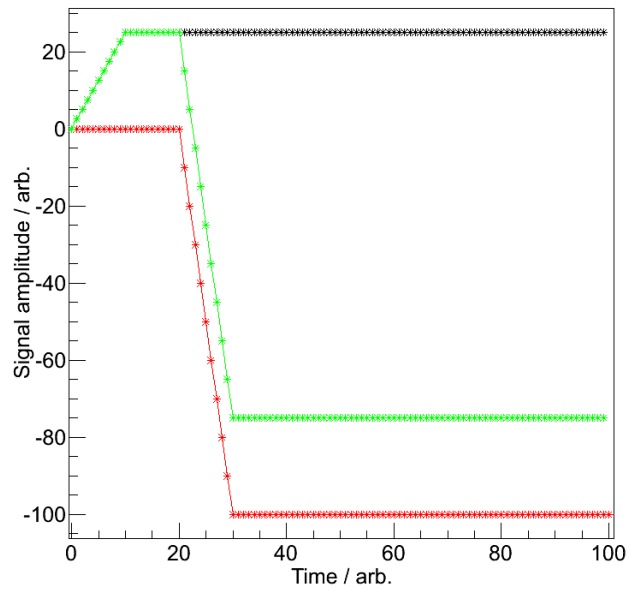
Figure 4.11: DAQ architecture diagram [70]. The role of the various modules is described in the text.

which is reflected in the rising edge of the transformed samples (F_k). This rising edge is used for the computation of the CFD time.

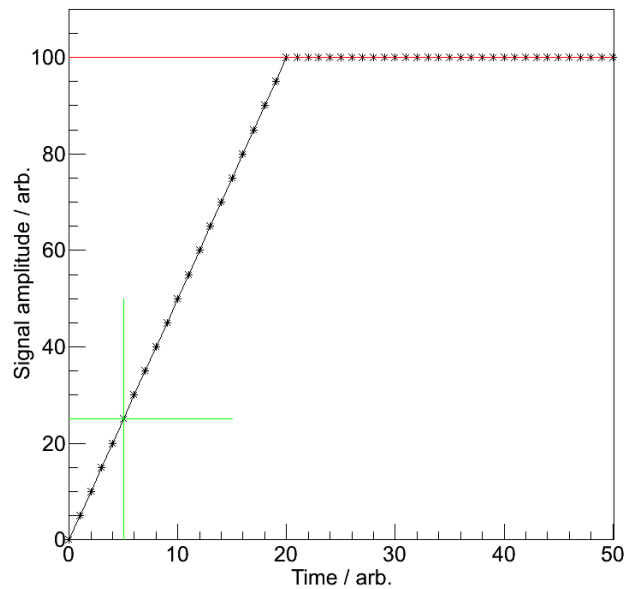
In the TIGRESS DAQ, when a signal goes over the leading-edge threshold to arm the DAQ, the DAQ takes a delay line clip of the signal and evaluates the height. The clipped pulse is then tested until it reaches 1/4 of the total size of the signal, this is all performed on a 100 MHz sampling clock synchronised with the global clock of the DAQ. The samples above and below the threshold are linearly interpolated to give a value of where the threshold was crossed of around 1/16 of a sample (0.625 ns). In DAQ tests of γ - γ timing, the best resolution achieved was around 30 ns FWHM [71]; with a 1- μ s long DAQ window, even assuming a poor timing resolution of 50 ns FWHM for the germanium signals, a timing gate should reduce the background from scattered beam to around 5% of its original value. Better timing resolutions, down to around 15 ns FWHM, may be achievable with a true digital CFD algorithm implemented in the DAQ [71]. Figure 4.12 shows schematic ‘classical’ and ‘TIGRESS’ CFD algorithms.

4.8.2 Output MIDAS files

The TIGRESS DAQ writes out the data in MIDAS files. In the experiment described in the next chapter, the DAQ was being run in ‘unassembled fragments’ mode for the



(a) Schematic diagram showing ‘classical’ CFD. The black line shows the attenuated original signal (which is assumed to have a risetime which is much smaller than the decay time of the signal, resulting in a flat top), the red line shows the inverted and delayed original signal and the green line shows the sum of the two signals. The CFD time is taken to be the zero-crossing point of the combined (green) signal.



(b) Schematic diagram showing ‘TIGRESS’ CFD. In this case, the position where the signal reaches 25% of the total signal height is taken to be the CFD time. The black line shows an ideal signal similar to that in figure (a), the red line shows the amplitude of the pulse. The green lines show the point where the signal has reached 25% of the total signal amplitude and the relationship of this to the CFD time.

Figure 4.12: Schematic diagrams showing ‘classical’ and ‘TIGRESS’ CFD algorithms.

first time; this allows the DAQ to deal with a higher trigger rate which is required for the $^{15}\text{O}(^6\text{Li},d)^{19}\text{Ne}$ experiment. This mode writes out each channel individually after the DAQ has been triggered rather than collating the information from all channels together and writing it out as one event. This was the first time this mode had been used in an experiment and testing whether the reassembly of event fragments into full events with correlations between channels formed part of the work of this thesis.

Each fragment, whether from silicon, germanium or BGO, starts with a header which contains the number of entries stored in each event⁶, along with other information. Each event then includes an event ID (starting 0x8), the channel that the event corresponds to (starting 0xb), the trigger pattern (0xb) which contains information about which channels have requested triggers, a timestamp (0xa0 and 0xa1), the CFD value (0x4) and the charge (0x5). [72] The event may also include waveform samples (starting with 0x0). These are only present for two of the TIGRESS clovers (positions 5 and 6). Each fragment terminates with an entry that begins 0xe.⁷

In order to evaluate the data, it is necessary to first assemble the event fragments into full events. The method for this is described in section 5.2.

⁶I.e. whether the event only consists of the triggered channel, energy etc. or whether it also includes waveform information.

⁷In late 2012, a leading edge discrimination entry was added to the MIDAS output. This entry starts 0x6 and is not present in the data discussed in this work.

Chapter 5

Data analysis of the $^{20}\text{Na} + ^6\text{Li}$ experiment

5.1 Introduction

In October 2010 an experiment (S1213 - spokesman C. Aa. Diget) was carried out at TRIUMF-ISAC with the SHARC and TIGRESS arrays. The aim was to measure the $^{20}\text{Na}(^6\text{Li},d)^{24}\text{Al}$ and $^{20}\text{Ne}(^6\text{Li},\alpha)^{22}\text{Mg}$ reactions using a ^{20}Na beam incident upon a $290 \mu\text{g}/\text{cm}^2$ ^6LiF target on a $15 \mu\text{g}/\text{cm}^2$ ^{12}C backing. The experiment provided a test of SHARC/TIGRESS for $(^6\text{Li},d)$ reactions in inverse kinematics with radioactive beams at TRIUMF-ISAC, which will be used for the planned $^{15}\text{O}(^6\text{Li},d)^{19}\text{Ne}$ experiment. The author was responsible for the analysis of the data from this experiment, specifically:

1. Constructing an analysis code for SHARC/TIGRESS data in the new event fragment format, and demonstrating that the reconstruction of event fragments functions correctly. In order to do this, reaction channels must be successfully identified in the data.
2. To test the performance of the new TIG-64 ADC/TDC modules which had replaced the TIG-10 modules used previously.
3. Testing the new preamplifiers which had been constructed for silicon detector readout
4. Develop algorithms for: calibration of the array including crosstalk corrections, particle identification using differential energy loss including the thickness corrections required due to the range of angles of entry into the dE detector and multiparticle Doppler correction for the recoil based on light ions detected.

Several problems were uncovered during the analysis. In particular, a serious problem with the constant fraction discrimination algorithm in the firmware was found which requires major modifications to the TIGRESS data acquisition system.

In this chapter, the details of the analysis code written by the author are discussed followed by discussion of results emerging from the analysis.

5.2 MIDAS to ROOT conversion

In order to analyse the data, the MIDAS files must first be converted into a more useful format. This is done using the TigSort program written by U. Hager of the Colorado School of Mines [73]. TigSort uses the event numbers created by the DAQ to reconstruct events from the event fragments that were written out. Assembly of events online takes processing power in the DAQ and makes it more difficult to deal with higher rates. TigSort requires a list of hexadecimal channel addresses and the detector to which they correspond; these addresses are generated from DAQ scripts.

TigSort reads in the event fragments from a MIDAS file, collates all event fragments with the same timestamp, converts the values recorded in the MIDAS file into integers, and then writes out complete events to an ‘assembled’ ROOT file. In this assembled file, each event contains certain data:

- The number of hits for each detector; for the silicon detectors, the front and back of the detector were treated separately for these purposes.
- An array that lists the channels hit.
- An array that lists the charge collected in each channel.
- If CFD values were included, then similar data exist for the CFD values. In this case, the number of hits for each detector should be the same as for the charge collected hits.

5.3 ‘Event’ to ‘Particle’ conversion

In order to reduce the time taken to sort the data, a presort was undertaken. This comprises the first part of the newly constructed sort code written by the author. This sort converted from ‘event’ data to ‘particle’ data. Practically, this means that silicon detector strip numbers and germanium segment positions were converted into angles and charges were converted into energies. Suppression and addback for the TIGRESS clovers is also done in this stage.

TigSort occasionally has problems converting hexadecimal values back into decimal numbers. When this occurs, the value recorded is 65536 (2^{16}) too high. This wrap-around effect is trivial to remove. This may be due to problems with a sign/unsigned and/or long/short integer software issue [74].

5.3.1 SHARC events

SHARC events were considered valid if there is one hit on the front and one on the back of a strip detector and the energy recorded for the front and back of the detector were approximately equal. The pad detector charge recorded is required to be greater than a set threshold in order to remove noise and background. The strip and pad detector energies (including corrections for crosstalk which will be discussed later), azimuthal and polar angles, etc. were all then computed and the ‘particle’ is saved in the output ROOT file.

Preamplifier saturation

During the experiment, it was noted that there were two wide peaks at high energy in the upstream CD. These were originally thought to be deuterons from $^{20}\text{Na}(^6\text{Li},d)^{24}\text{Al}$ reactions. This effect was traced to premature preamplifier saturation. On the highest sensitivity preamplifier setting (the highest sensitivity and lowest energy range) which had a nominal range of up to 14 MeV, the saturation was occurring at some energy below this, at about 12 MeV for the front and 10 MeV for the back. Subsequent pulser tests of the preamplifiers showed that all of the gain settings saturated too soon, and that one of the settings (the third most sensitive, with a nominal range of around 200 MeV) showed strong non-linearity for the ohmic signals in addition to early saturation of junction and ohmic signals. The SHARC preamplifiers have now been modified to remove this effect, but this resulted in most of the $^{20}\text{Na}(^6\text{Li},d)^{24}\text{Al}$ data being unusable.

5.3.2 TIGRESS events

TIGRESS events are computed in stages. First of all, the signals in the BGO suppressors are considered using previous studies of the Compton suppression schemes [69, 75] which suggested that, for low multiplicity events where there are high energy γ rays (as might be expected from lighter nuclei), the optimal suppression scheme is the ‘full-clover’ scheme. This involves using all suppression shields on a clover to check whether an event is valid or invalid.¹ Once this has been done for all clover positions, the energy of each hit can be calculated from the charge recorded for the core of the HPGe crystal. Addback and interaction position are calculated simultaneously. The position of the interaction is calculated using a similar logic as that used for the Segmented Germanium Array (SeGA) at the National Superconducting Cyclotron laboratory [76]:

1. If only one segment detects a hit, then the position of the interaction is assumed to be at the centre of that segment.

¹N.B. In Refs. [69, 75], the high-efficiency configuration of TIGRESS is called ‘HPGe Forward’.

2. If there are two segments with hits, then the higher energy one is taken as the interaction position if the total energy recorded is greater than 511 keV. Otherwise, the lower energy segment is taken to be the interaction position.
3. If three or more segments fire, then the highest energy one is taken as the interaction position.

Using this position, the line-of-sight vector of the TIGRESS segment from the target can be calculated for use in the Doppler correction.

There are a number of addback schemes suggested in Ref. [75]; originally, a modified version of the ‘neighbouring’ scheme had been adopted. This scheme uses ‘full-clover’ addback if more than one core has a signal within one clover, and also performs addback between two adjacent crystals in different clovers if both of the crystal cores are the only cores to have fired in their respective clovers. This is the suggested scheme for low multiplicity scenarios. In this case, the lack of timing information discussed in section 5.5 means that, if addback of this form is used, then false coincidences between 511- and 1634-keV γ rays from decay of scattered beam and γ rays from reactions are falsely interpreted to be due to one γ ray. With this in mind, the addback was returned to the ‘full clover’ scheme, omitting the addback between adjacent crystals in different clovers.

Removal of double-Mapped TIGRESS crystals

During the analysis, it was noted that the hexadecimal addresses for the MIDAS files produced by the DAQ were repeated for some channels. This overlap occurred for a pair of positions and was the result of a mislabelling in the DAQ and was thus irrecoverable. For one of the positions, the HPGe detector failed before the experiment and was removed. The BGO suppressors were still in place, however. Therefore, to avoid false suppressions, both positions (clover and suppressors) were removed from the analysis.

5.4 Calibration

5.4.1 SHARC

The SHARC strip detectors were calibrated using a 3α source composed of ^{244}Cm , ^{241}Am and ^{239}Pu . Data for the decays of these nuclei may be found in table 5.1. Resolutions of around 28 keV FWHM were typical for the SHARC detectors. In addition to this calibration, corrections must be made for cross-talk effects.

Cross-talk

The BB11 SHARC box strip detectors have a 76-way connector on the PCB from which signals are read out, as shown in fig. 5.1.

Nuclide	Energy / MeV	Intensity / %
^{244}Cm	5762.64	23.10
	5804.77	76.90
^{241}Am	5442.80	13.1
	5485.56	84.8
^{239}Pu	5105.5	11.94
	5144.3	17.11
	5156.59	70.77

Table 5.1: α -decay energies and intensities from a 3α ($^{244}\text{Cm}/^{241}\text{Am}/^{239}\text{Pu}$) source [77–79]. Only the strong decay branches ($>5\%$) are given.

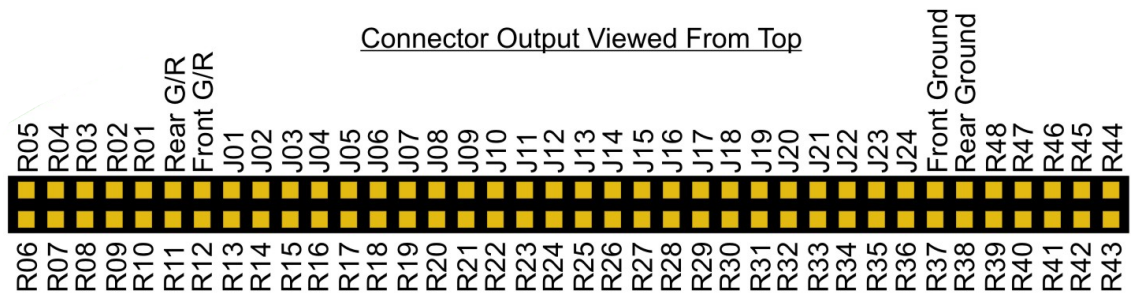


Figure 5.1: Ribbon cable pin arrangement for the BB11 box strip detectors from SHARC. Pins labelled with a J are junction-side (front) pins, while those starting with R are reverse-side (ohmic, back) pins. The pin arrangement is the same for the $140\mu\text{m}$ and the $1000\mu\text{m}$ SHARC BB11 detectors. [80]

If certain pixels are hit, the two wires which read out the front and back strips corresponding to that pixel are next to each other in the ribbon cable. This occurs when the difference between the back channel number and front channel number ($\delta(\text{channel})$) is 12 or 13. Negative crosstalk between these adjacent signals causes a reduction in the size of the signals in these wires. In order to calibrate the SHARC detectors, these pixels are initially omitted in the calibration of each strip. The energy recorded in these pixels will be lower than the true value, this can be seen in fig. 5.2a. This effect can be removed by a multiplicative factor for these pixels; the factor is just that value required to give the correct 3α energies for these pixels. A plot of the energy against $\delta(\text{channel})$ with the correction applied is shown in fig. 5.2b.

Pad Detector Calibration

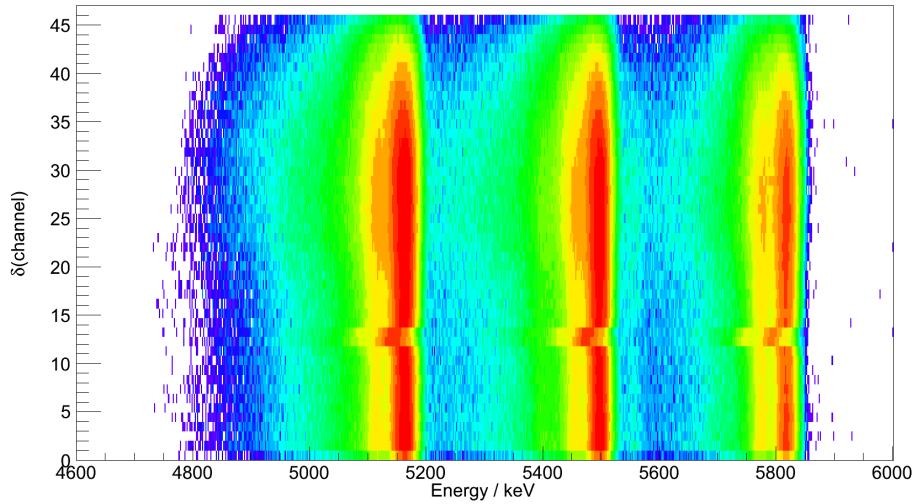
During this experiment an attempt was made to calibrate the SHARC pad detectors using a ^{207}Bi source. However, due to the high levels of electronic noise on the detectors, this was not possible. Subsequently, an attempt was made to calibrate the pads by considering the energy lost in the strip detector. Given dE , the energy lost by the proton passing through the detector, and the path-length of the proton within the detector, the total energy (E_{tot}) of the proton can be calculated. The energy deposited in the pad detector will then be equal to: $E_{pad} = E_{tot} - dE$. This technique provided gain and offset parameters with large uncertainties. For simplicity, the offsets for the pads were taken as 0, and the gains were taken to be an average value for the preamplifier setting used, which was known from the calibration of strip detectors using the same setting.

5.4.2 TIGRESS

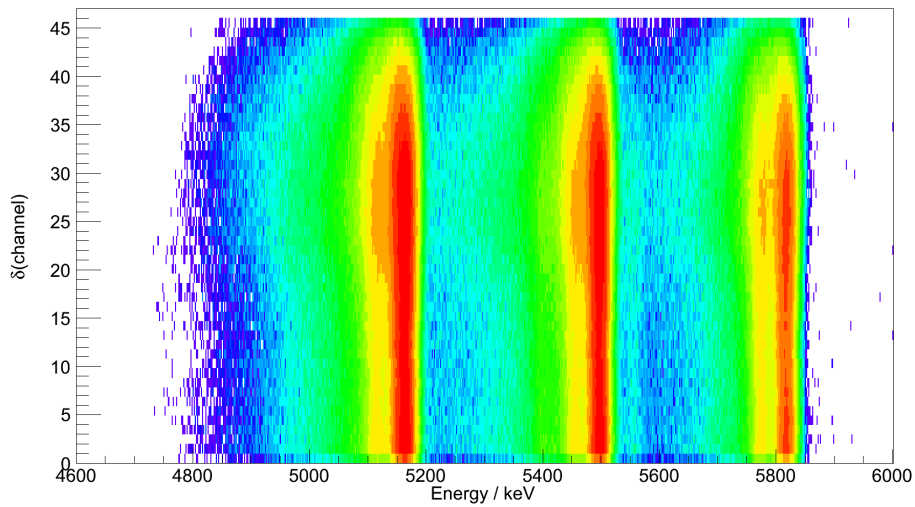
The TIGRESS clovers (cores and segments) are calibrated using ^{60}Co and ^{152}Eu sources. Calibration of the segments is necessary to allow for the correct determination of the position hit by a γ ray for the Doppler correction. The calibration of the TIGRESS detectors is performed automatically by the DAQ. Charges are recorded in the output data stream along with the calibration parameters generated by the DAQ. These calibration parameters have been used in the analysis.

5.5 Timing information

The DAQ readout window is $1\text{-}\mu\text{s}$ long meaning that γ rays resulting from the decay of scattered beam which are not related to the event-producing trigger are a large source of background. Incomplete collection of the energy from γ rays as discussed in section 4.6 means that a Compton continuum below each photopeak can obscure γ rays resulting from the reaction channel of interest. It is possible to use either Leading-Edge Discrimination



(a) Energy against $\delta(\text{channel})$ for one BB11 box strip detector. The reduction in the energy collected is easily visible when $\delta(\text{channel})=12,13$.



(b) Energy against $\delta(\text{channel})$ for one BB11 box strip detector. The crosstalk effect in $\delta(\text{channel})=12,13$ has now been removed with the application of a multiplicative corrective factor.

Figure 5.2: Histograms showing the crosstalk in the BB11 box strip detectors and its removal.

(LED) or Constant Fraction Discrimination (CFD) to calculate a time within the DAQ window when the event was detected.

Only CFD was implemented in the TIGRESS DAQ at the time of the experiment; as mentioned in the previous chapter, a LED timing value was added in November 2012 as a result of the problems identified in the test experiment data from this thesis. In theory, the CFD value recorded for each channel should be relative to the timestamp for each event. All event fragments from the same trigger should have the same timestamp. The difference between CFD values can then be used to require a time-coincidence.

Silicon timing was the first analysed as silicon has a shorter collection time for signals due to the higher drift velocity of electrons and is therefore better for testing the timing from the DAQ. This experiment was the first that used TIG-64s and it was not known if there were channel offsets that would need to be taken into account for the silicon timing. More details will be provided on this in the following section.

After the silicon timing data were analysed and the required offset corrections were made, the germanium timing data were analysed. This uncovered a major problem in the DAQ: germanium CFD values are frequently not being recorded for some reason. More details are provided on this after the silicon timing has been discussed.

5.5.1 SHARC timing information

In order to test how the times recorded in different SHARC channels are related to each other, 3α data was used to look at the front-back coincidences in the strip detectors. A typical δ CFD (CFD value for the front strip - CFD value for the back strip) spectrum for one pixel is shown in fig. 5.3. A common feature of the silicon δ CFDs is the satellite peak at some lower value of δ CFD. This can also be seen in figs. 5.4a and 5.4b. This origin of this has not been ascertained; it is not due to beam pulses as the data used for the plots below comes from 3α calibration data.

In addition, an offset effect is observable between channels. This is likely caused by either the preamplifiers or, more likely, the TIG-64s. Figures 5.4a and 5.4b show the offsets for one channel on the front of the box detector versus all of the backs and *vice versa* respectively. The repetition after 24 channels in fig. 5.4a is either due to the two different preamplifiers or the two different TIG-64 mezzanines used for the 48 channels across the back of each BB11. Given that the preamplifier channel track lengths do not follow the pattern visible in fig. 5.4a, it is likely that this effect is due to the TIG-64s. Correction for this effect just requires a predictable channel-by-channel offset to be added to the δ CFD.

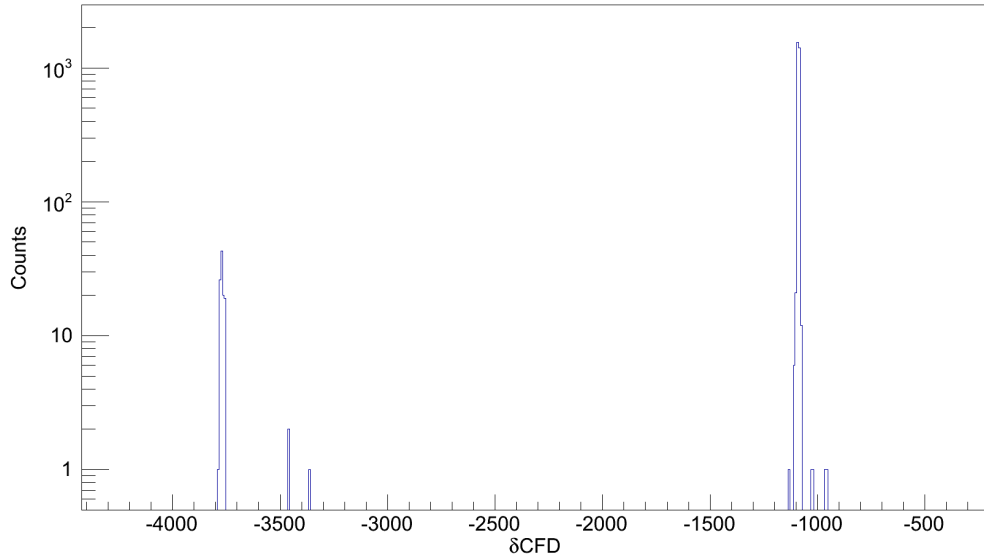


Figure 5.3: δ CFD spectrum for one pixel in upstream box 2 (front channel 12, back channel 4). Each CFD unit corresponds to 0.625 ns, meaning that the two peaks are around 2 μ s apart, a longer period than the trigger window. This further suggests an artefact of the CFD algorithm rather than any physical effect. The timing peaks are around 20 ns FWHM.

5.5.2 TIGRESS timing information

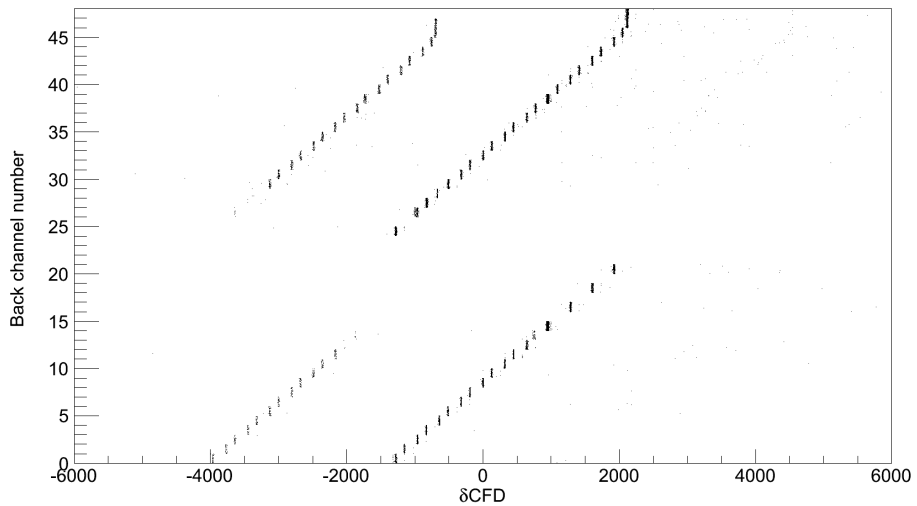
A similar procedure was used to test the TIGRESS timing information. In this case, ^{152}Eu data which had been taken for efficiency calibrations were used. ^{152}Eu has a large number of peaks, only some of which are in coincidence, allowing tests of not only the timing coincidences, but also the suppression of γ rays that cannot come in coincidence.

To test the CFD values, a gate can be placed around two γ rays that should come in coincidence and the relative CFD values can be compared. For events in coincidence, this should result in a peak in δ CFD at around 0, assuming that there are no offsets between channels. When this was done, however, many of the δ CFD values calculated were exactly 0. To ascertain why this was the case, the actual numerical values of the CFD values, rather than the differences between two CFD values, were plotted for HPGe detectors, BGO suppressors and SHARC silicon detectors.² These are shown in figs. 5.5 to 5.8.

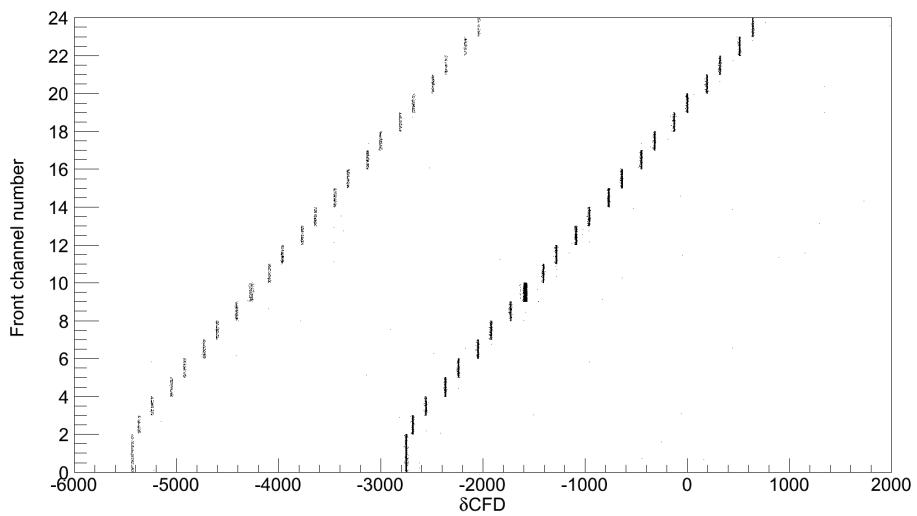
For the HPGe detectors, a CFD value of 0 is being recorded for the vast majority of events. In fact, for the ^{152}Eu data, 98% of CFD values recorded were 0.³ In contrast, the BGOs and silicon detectors show a constant CFD value distribution. Obviously, given that 98% of the CFD values are lost, the timing information cannot be effectively used for sup-

²The SHARC CFD values are from the 3α run used for the previous timing investigation.

³For clarity: the MIDAS event fragments contained '0x40000000' words which, when converted from hexadecimal, give 0.



(a) δCFD for upstream box 2 front channel 12 against upstream box 2 back channels.



(b) δCFD for UBx2 back channel 4 against UBx2 front channels.

Figure 5.4: Figures showing systematic effects in silicon timing values from one of the SHARC BB11 silicon detectors. The repeated pattern in (a) suggests that the effect is due to the TIG-64 mezzanines.

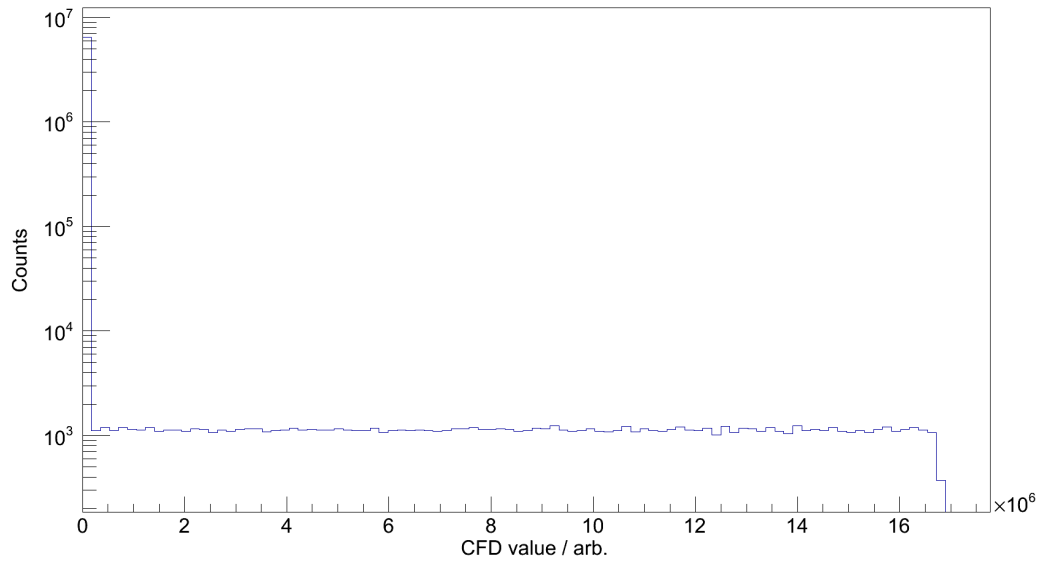


Figure 5.5: CFD values for all TIGRESS cores

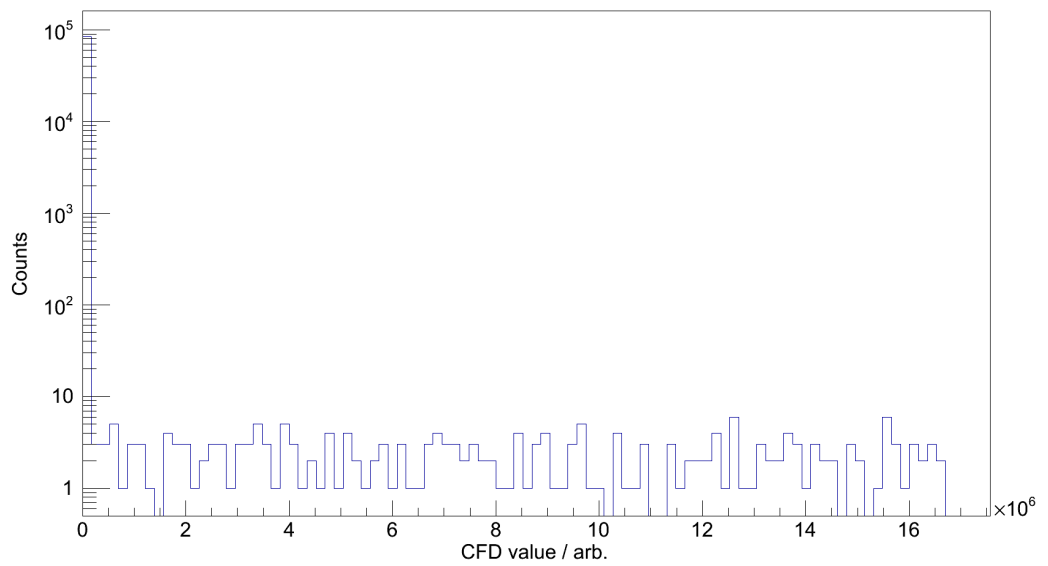


Figure 5.6: CFD values for the Blue crystal core of clover position 8

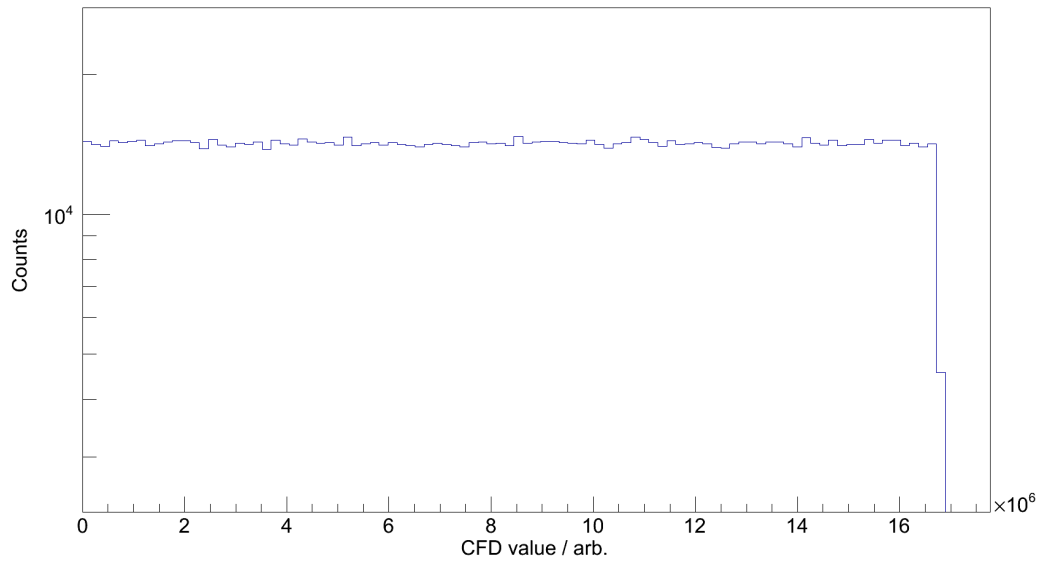


Figure 5.7: CFD values for all BGO suppressors

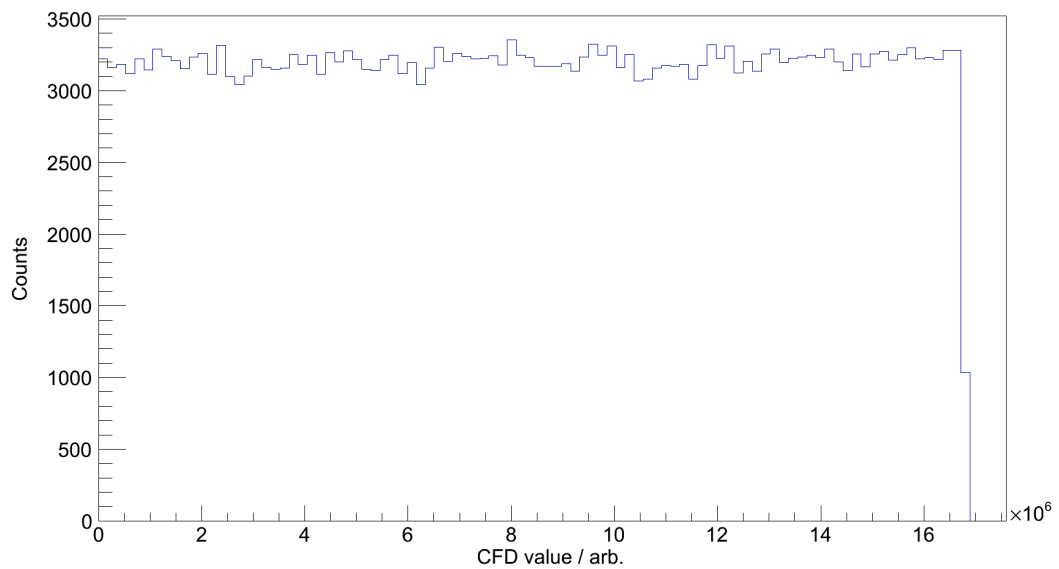


Figure 5.8: CFD values for SHARC detector upstream box 2, front strip 12.

pression of the random background. This is a serious problem with the TIGRESS readout that has not been uncovered previously. While testing of the TIGRESS timing algorithm has taken place previously, and an attempt was made to use the timing information to suppress background in another SHARC/TIGRESS experiment (that of Ref. [65]) using a radioactive beam, changes had been made to the DAQ in the intervening period which may have caused the problems with the DAQ. Subsequent tests of the timing information have found that the delay line clip appears to frequently miss the germanium signal [81]. A leading-edge discriminator has now been added to the DAQ, and further tests are being made in order to effect a robust CFD system.

Waveforms were written to disk for two clovers while the ^{152}Eu data were taken. An offline CFD algorithm was constructed in an attempt to recover timing information for the purpose of testing the germanium timing background suppression. However, the total number of coincident events in the two clovers was not high enough for useful conclusions to be drawn.

5.6 Testing the reconstruction: writing the analysis code and identifying reaction channels

In order to test whether the reconstruction of the event fragments and the analysis code are functioning correctly, identification and characterisation of different reaction channels was required. In this section, the original aims of the experiment (in addition to the test of the ^{15}O experiment) are briefly discussed along with the identifiable reaction channels and the analysis techniques used in order to identify channels.

This experiment was designed to, as well as test $(^6\text{Li},d)$ reactions in preparation for the $^{15}\text{O}(^6\text{Li},d)^{19}\text{Ne}$ experiment, also test whether $(^6\text{Li},\alpha)$ reactions can be used to populate astrophysically-relevant states. In this case, the lack of timing information means that the 332-keV γ ray which would have been used to tag on the $^{20}\text{Na}(^6\text{Li},\alpha)^{22}\text{Mg}(p)^{21}\text{Na}$ reaction is obscured under the Compton continuum of the 511-keV γ rays resulting from annihilation.

There are a number of other reaction channels which can be used to test the analysis code. Fusion-evaporation channels are strong and give an opportunity to test whether the multiparticle Doppler correction functions correctly. Water contamination in the hygroscopic LiF target causes (p,p') scattering from the target which is detected in downstream detectors. Finally, a $(^6\text{Li},d)$ reaction channel which populated proton-unbound states in ^{24}Al is observed.

5.6.1 Effective thickness correction

In section 4.5.4, the use of the $dE - E$ method of particle identification was discussed. In the box detectors, the effective thickness of the dE detector to particles originating at the target position changes by a large amount. This leads to broadening of the $dE - E$ loci and loss of the particle ID. In order to retrieve this information a number of approaches can be taken, the criterion being that the $dE - E$ loci from different species are separated well-enough to be identified. A pixel-by-pixel approach, while removing the effective thickness problem, can leave $dE - E$ loci hard to see due to the low number of counts. In addition, 1152 separate gates would need to be made for each box detector. A strip-by-strip approach should give narrower $dE - E$ loci, but for certain strips that are far from the target position, the variation in the effective thickness is still large enough to be problematic. In addition, in order to reduce the broadening of the loci, the back (θ) strips should be used, which necessitates 48 different graphical cuts for each box detector. Therefore, to avoid a large number of cuts with low statistics having to be made, it is easier to use a detector-wide effective thickness algorithm.

There are two different possible methods for this algorithm, the first is to assume a constant energy loss as the particle travels through the dE detector. This can cause $dE - E$ loci from species with the same atomic number to be poorly-separated when most of the energy loss is in the dE detector; in this case, the energy loss is not well-approximated by assuming it to be constant. The second method uses the range-energy curve for that species in silicon to calculate what the energy lost would have been if the particle had been normally-incident on the detector. If a particle of energy E_i has a range $R(E_i)$ in an absorber, then for a particle of energy E_1 incident on an absorber of thickness t , then the final energy E_2 must satisfy the relation:

$$R(E_2) = R(E_1) - t \quad (5.1)$$

The purpose of this effective thickness correction is only to separate the $dE - E$ loci. The energy of the emitted particle is taken to be the sum of the strip and pad energies. Therefore, while the effective thickness correction does require some knowledge of the species, it is sufficient to correct for protons and deuterons simultaneously, using the same energy-range function. However, in this case, in order to prevent the α $dE - E$ locus being broadened down over the proton and deuteron loci as an artefact of the correction, it is necessary to limit the maximum dE when doing the hydrogen-species correction. The uncorrected $dE - E$ spectrum from UBx2 is shown in fig. 5.9, while the corrected $dE - E$ spectrum is shown in fig. 5.10 assuming that the emitted species are all protons with a dE cut-off at 6 MeV. In the uncorrected spectrum, there is no separation between the deuteron and proton loci, this separation is clearly recovered when the spectrum is corrected for the effective thickness.

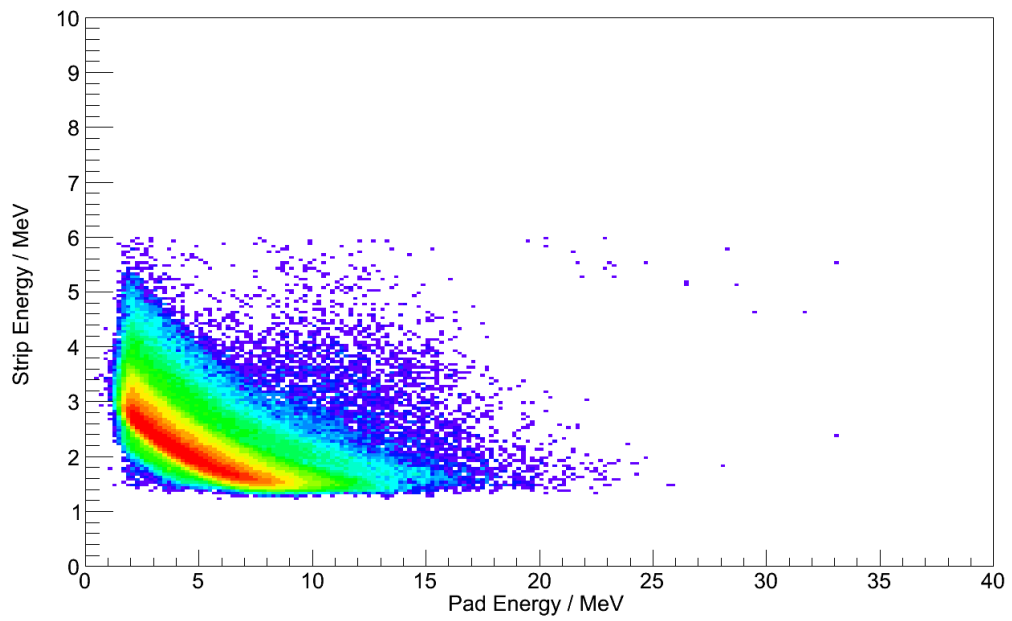


Figure 5.9: $dE - E$ UBx2 Uncorrected with strip detector energy cut-off at 6 MeV

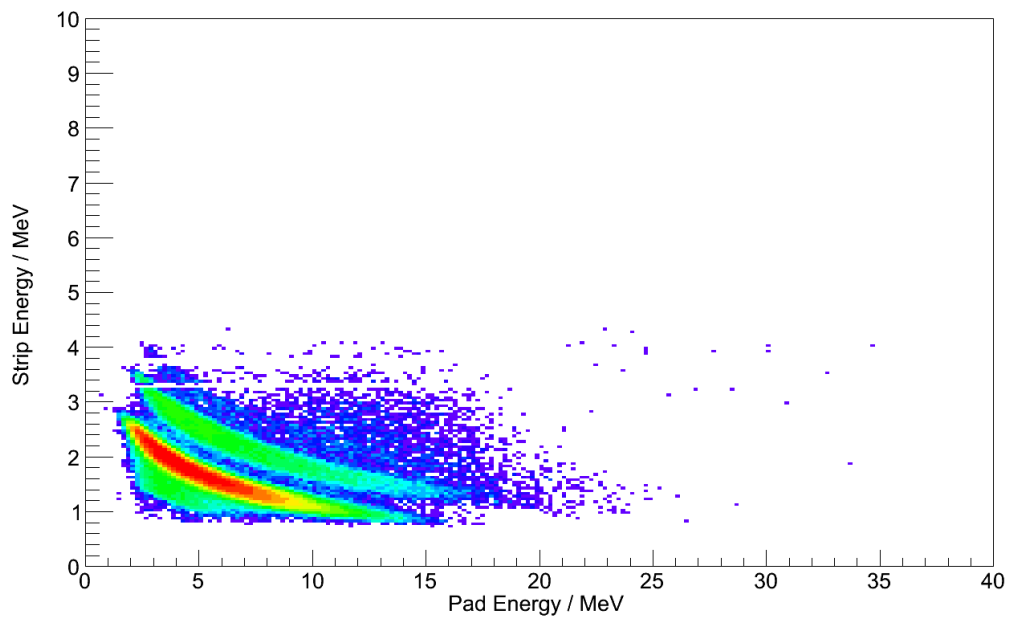


Figure 5.10: $dE - E$ UBx2 with a proton correction and strip energy detector cut-off at 6 MeV

5.6.2 Doppler correction

The Doppler shift is a well-known phenomenon: the apparent frequency of radiation emitted from a source changes depending on the relative velocity between the source and the observer. The recoils in this experiment were moving at 5-10% of the speed of light, depending on whether the reaction is off ${}^6\text{Li}$ or ${}^{19}\text{F}$, so a Doppler correction is required in order to correctly reconstruct the γ -ray energies. The relation between the source energy and the observed energy is:

$$E_{observed} = \frac{E_{source}}{\gamma(1 + \beta \cos \psi)} \quad (5.2)$$

where E_{obs} is the observed energy; E_{source} is the energy of the γ ray ‘at source’, when emitted by the recoil nucleus; $\beta := \frac{v}{c}$ and $\gamma := \frac{1}{\sqrt{1-\beta^2}}$; and ψ is the angle between the line-of-sight based on where the first interaction point of the γ ray is calculated to be and the velocity of the source (see fig. 5.11).

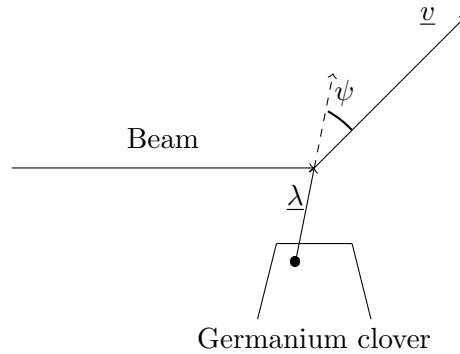


Figure 5.11: The angle ψ used in the Doppler correction formula is shown on the above diagram to show the relationship with the recoil velocity, \underline{v} and the line-of-sight, $\underline{\lambda}$ of the detector. The filled circle in the detector represents the calculated interaction position.

In order to correct for the Doppler shift from the recoiling nuclei, two pieces of information are required: the velocity of the recoiling nucleus, and the angle relative to the recoil velocity at which the γ ray from the decay was emitted. The recoil velocity can be calculated from the momenta of the detected light ions by requiring the conservation of momentum. Multiparticle exit channels are possible, especially from fusion evaporation reactions of ${}^{20}\text{Na}$ on ${}^{19}\text{F}$ in the target. In this case, the Doppler correction should be made based on all of the evaporated particles. In cases where an α particle is evaporated but not collected, the Doppler correction will be poor.

To calculate the angle of emission, the particle velocity and the line-of-sight are used. The line-of-sight is from the point within the TIGRESS HPGe detector where the first interaction of the γ ray is assumed to occur to the target position, where it is assumed the γ ray originated. The line-of-sight vector, $\underline{\lambda}$, is calculated from the angles calculated

in the ‘event’ to ‘particle’ conversion described in section 5.3.2. The angle is calculated using the scalar product:

$$\psi = \arccos\left(\frac{\underline{v} \cdot \underline{\lambda}}{|\underline{v}||\underline{\lambda}|}\right) \quad (5.3)$$

5.7 Fusion evaporation products

Using the energies of the detected ejectiles, the momentum of the recoiling nucleus can be found using conservation of momentum:

$$\underline{p}_{beam} = \sum_i \underline{p}_i + \underline{p}_{recoil} \quad (5.4)$$

where \underline{p}_i is the momentum of the i th ejectile. The recoil velocity can be found from the recoil momentum and used as an input for the Doppler correction algorithm described in section 5.6.2.

Light ions ejected during $^{20}\text{Na}+^{19}\text{F}$ reactions are likely to dominate over other reaction channels. PACE [82] was used to estimate which nuclei were likely to be produced. PACE suggests that the three most likely products from fusion evaporation are ^{31}P (α , $3p$, n), ^{28}Si (2α , $2p$, n), ^{27}Al (2α , $3p$, n) and ^{24}Mg (3α , $2p$, n). In the strong fusion evaporation channels, there is always a neutron emitted which limits the resolution which can be obtained through Doppler correction - some momentum will always be missed. α -particle emission will, however, dominate the outgoing momentum as they are more massive and provide a larger momentum ‘kick’ to the recoil.

The effect of better-constrained kinematics can be seen in figs. 5.12 to 5.16. These spectra have been generated by inspecting the number of protons and α s detected during an event, based on the $dE - E$ particle identification. Once this has been done, a Doppler correction is performed based on the momentum of these ejectiles. α -particles cause a larger momentum kick when being emitted; fig. 5.16 has two ejectile α s detected, giving the best reconstruction of the peaks.

Based on these plots, it is possible to identify peaks with well-known transitions. It is noticeable that the 511-keV transition (even though spread out due to the Doppler correction) is still strong in these spectra when the timing information cannot be used to suppress the beam background.

In addition to the 511-keV transition, there are a number of other transitions. The 184-keV transition is due to the decay of the 1121-keV state to the 937-keV state in ^{18}F . The mechanism for population of this state is not clear. Coincidence spectra with the 184-keV transition show the 937-keV transition to the ground state clearly but no structure in the particle spectra.

The 197-keV transition is due to inelastic excitation of the ^{19}F in the target.

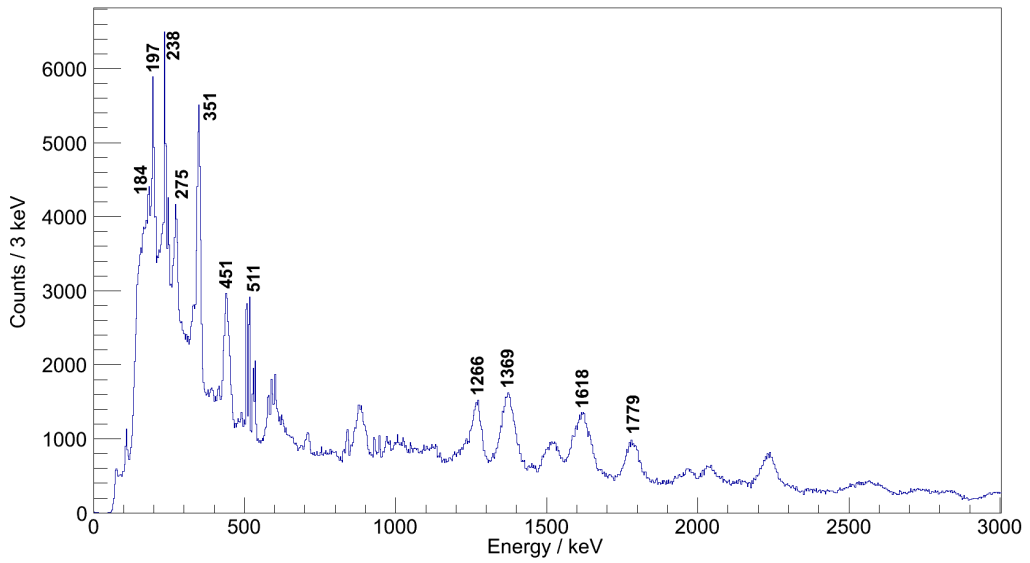


Figure 5.12: Doppler-corrected γ -ray spectrum with one ejectile proton detected, assuming reactions from ^{19}F and a recoil of mass 38 a.m.u. Some of the transitions of interest have been marked; see the text for further details.

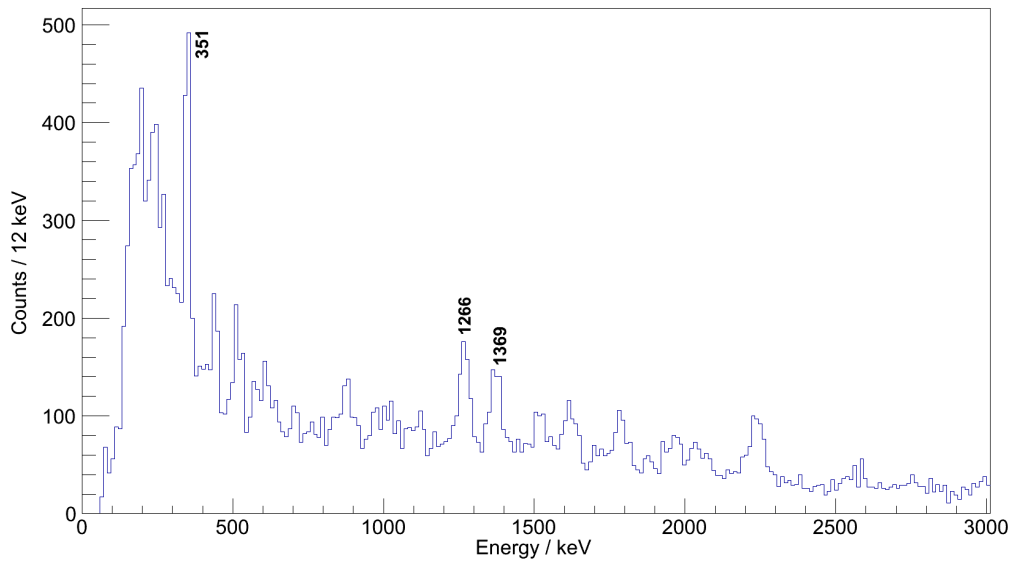


Figure 5.13: Doppler-corrected γ -ray spectrum with two ejectile protons detected, assuming reactions from ^{19}F and a recoil of mass 37 a.m.u.

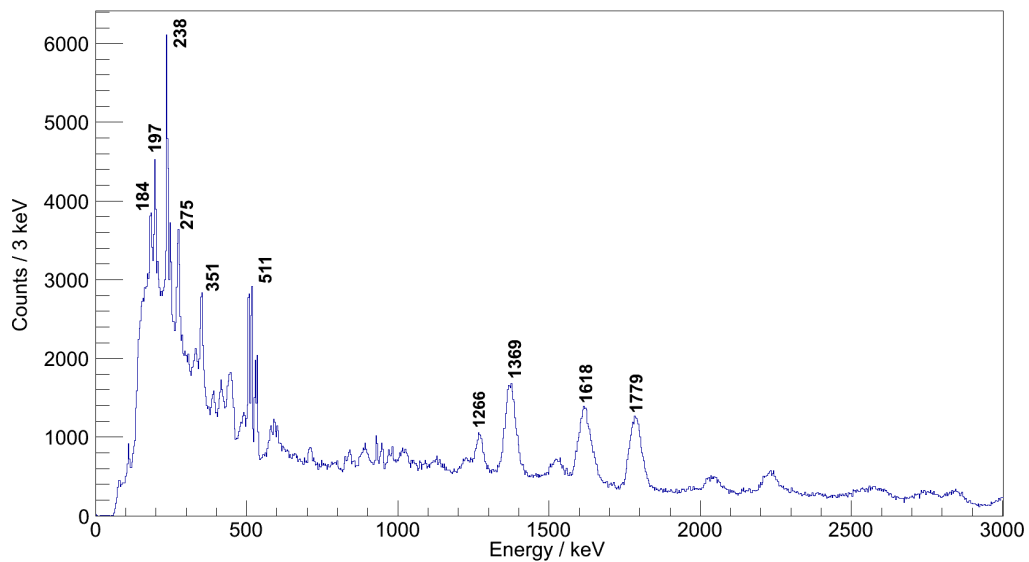


Figure 5.14: Doppler-corrected γ -ray spectrum with one ejectile α -particle detected, assuming reactions from ^{19}F and a recoil of mass 35 a.m.u.

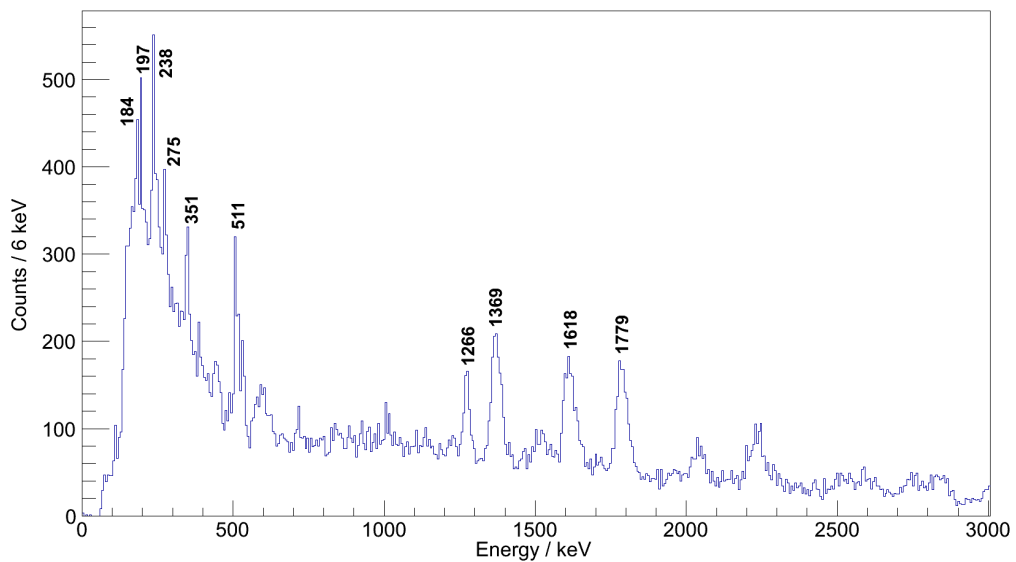


Figure 5.15: Doppler-corrected γ -ray spectrum with one ejectile α -particle and one ejectile proton detected, assuming reactions from ^{19}F and a recoil of mass 34 a.m.u.

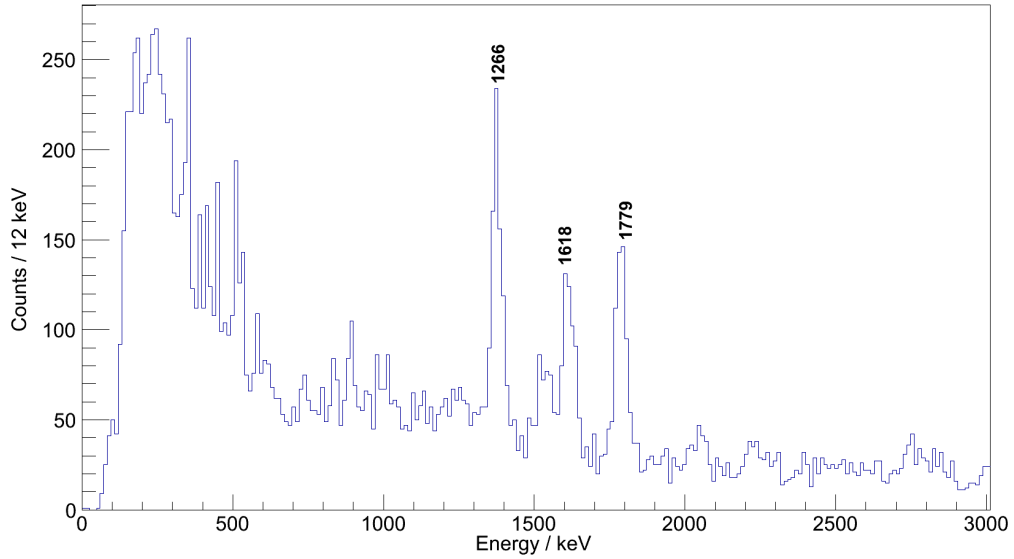


Figure 5.16: Doppler-corrected γ -ray spectrum with two ejectile α -particles detected, assuming reactions from ^{19}F and a recoil of mass 31 a.m.u.

The 238-keV and 275-keV transitions are both due to decays of the states of those energies in ^{19}Ne . Both states are likely populated by reactions which remove a proton from the ^{20}Na beam.

The 351-keV transition is due to ^{21}Ne produced in fusion-evaporation reactions from the ^6Li and ^{12}C backing in the target.

The 451-keV transition is due to ^{23}Mg produced in fusion-evaporation and α -transfer reactions only the beam.

The large peaks ranging from 1 to 2 MeV are all due to fusion-evaporation reactions of ^{20}Na with ^{19}F . These include the 1266-keV transition from ^{31}P , the 1369-keV transition from ^{24}Mg , and the 1618- and 1779-keV transitions from ^{28}Si . This demonstrates that the multiparticle Doppler correction is functioning as required.

5.8 $^{20}\text{Na}(p,p')^{20}\text{Na}^*$

One of the main advantages of using silicon-germanium arrays in coincidence is the ability to suppress background in the silicon detectors by gating on a γ ray. This technique has been successfully used previously with SHARC/TIGRESS [65]. In this experiment, the hygroscopic LiF target absorbs water. Protons from this water contamination can be scattered into downstream detectors. If there is inelastic scattering, then the coincident γ rays resulting from the decay of ^{20}Na excited states should be observable. Unfortunately, the kinematic locus of $^{20}\text{Na}(p,p')^{20}\text{Na}^*$ is such that the protons resulting from this reaction

punch through both of the downstream CD detectors (strip and pad), and only punch through the box strip detector at low values of θ in the downstream box detector. Given such a limited angular range and the small amount of water in the target, there is no useful physics information that can be extracted from this reaction, though it provides a good test as to whether the DAQ is functioning correctly.

In fig. 5.17, the Doppler-corrected γ -ray spectrum gated on protons in the downstream box is shown. A number of peaks are visible, most of which are due to fusion-evaporation. However, a peak is visible at around 600 keV. The identity of this peak can be confirmed by placing a gate around it, producing the Doppler-corrected γ -ray spectrum shown in fig. 5.18. The 200-keV γ ray produced by transitions from the 802 (4^+) state to the 596 (3^+) state in ^{20}Na can be observed.

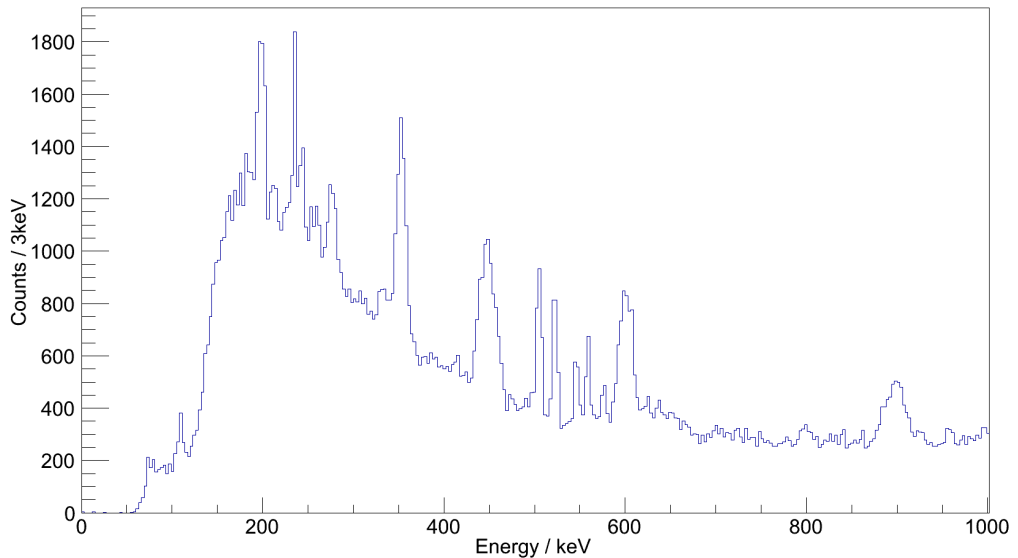


Figure 5.17: γ -ray spectrum gated on protons in the downstream box detectors with Doppler correction. The 600-keV γ ray can clearly be observed.

Using this γ ray, the selectivity on the reaction channel can be demonstrated. A E vs. θ plot for protons identified using $dE - E$ is shown in fig. 5.19. Figure 5.19a shows all of the proton events, while fig. 5.19b shows protons events which are in coincidence with the 600-keV γ ray. It is clear that the proton locus has been greatly reduced by the γ -ray gate.

5.9 $^{20}\text{Na}(^6\text{Li},d)^{24}\text{Al}^*(p)^{23}\text{Mg}$

Finally, reactions involving α -cluster transfer or incomplete fusion will populate states in ^{24}Al via the $^{20}\text{Na}(^6\text{Li},d)^{24}\text{Al}$ reaction. Due to problems with the preamplifiers, data

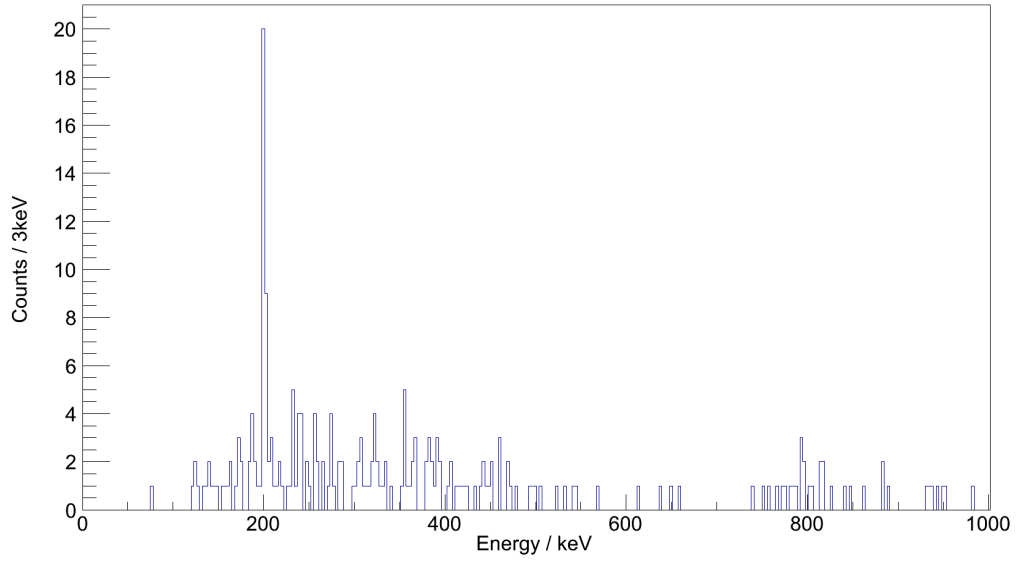
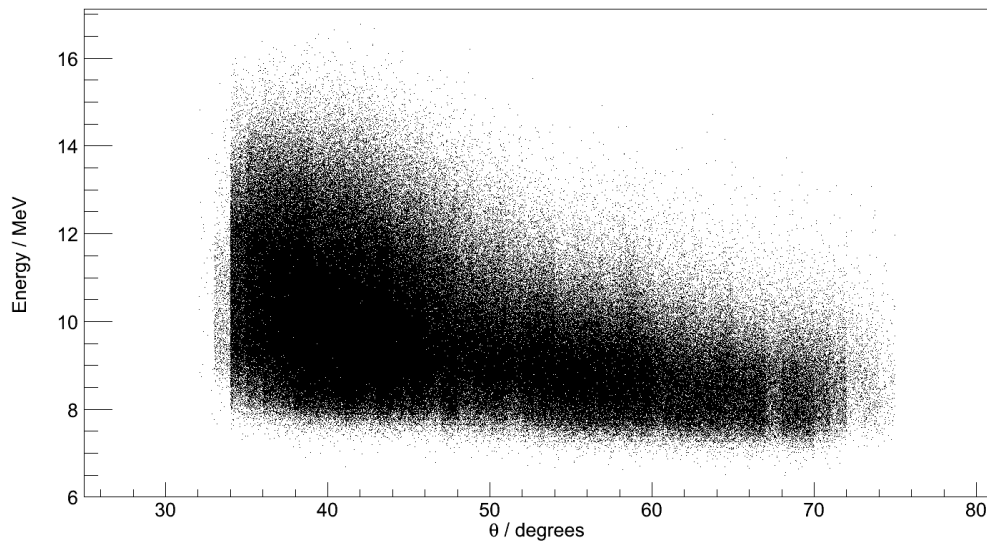
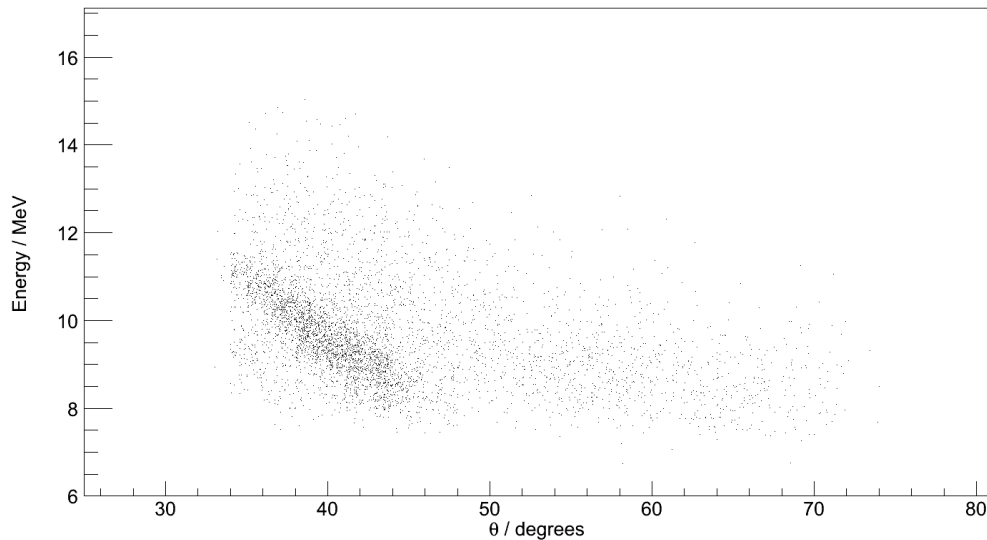


Figure 5.18: γ -ray spectrum gated on protons in the downstream box detectors with Doppler correction and the 600-keV transition visible in fig. 5.17. The 200-keV γ ray can clearly be observed.

from the upstream CD is not usable for much of the run and the cross section for the transfer reaction is largest into small centre-of-mass angles, which fall around 180° in the laboratory frame. However, in the upstream box, the particle identification that is offered by the $dE - E$ silicon telescope allows for a deuteron gate to be made. In this case, the states populated appear to be mainly those above the proton threshold; the γ ray visible in fig. 5.20 is at 451 keV, and results from the decay of the first excited state in ^{23}Mg . Again, this demonstrates that the analysis code can clearly identify reaction channels.



(a) Energy vs angle plot for protons in the downstream box with no conditions on the coincident γ rays.



(b) Energy vs angle plot for protons in the downstream box with a gate on the 600-keV γ -ray transition from the first excited state to the ground state of ^{20}Na . The locus due to the inelastically scattered protons is now clearly visible.

Figure 5.19: Figures showing the effect of gating on a γ -ray transition on the particle spectrum. The first plot shows the energy vs angle plot for protons in the downstream box identified through $dE - E$ gates. The second shows the same plot with an additional condition that a 600-keV γ ray was detected in coincidence with the proton. This corresponds to the first excited state to ground state transition in ^{20}Na and is caused by inelastic proton scattering from water in the target.

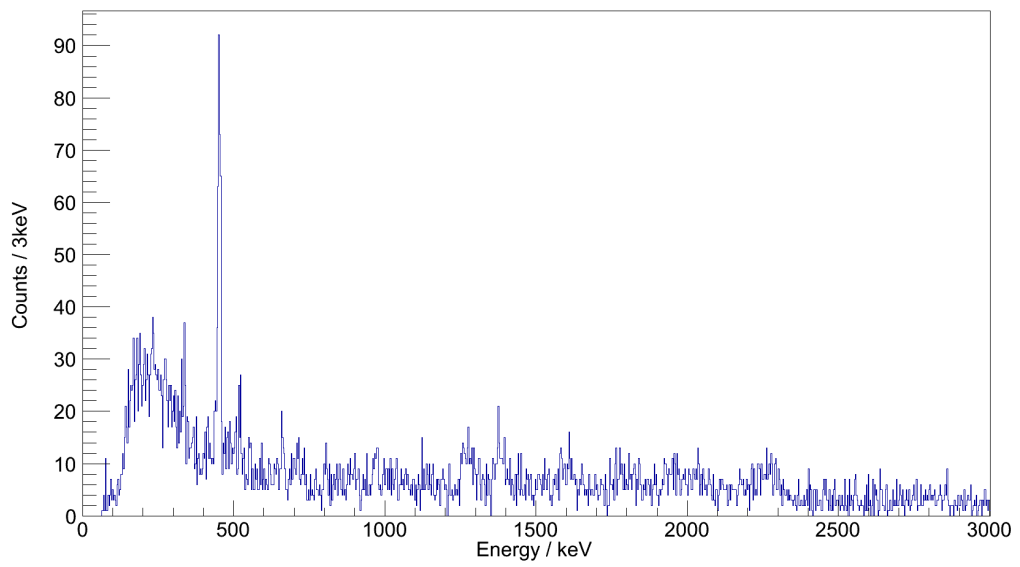


Figure 5.20: γ -ray spectrum gated on deuterons in the upstream box detector.

Chapter 6

Readiness for the $^{15}\text{O}(^6\text{Li},d)^{19}\text{Ne}$ experiment

From the work set out in the previous chapter, a number of important issues with the ^{15}O experiment have been identified as well as more wide-ranging problems with the arrays some of which have been fixed, some which remain a matter of concern.

6.1 Reconstruction of event fragments, construction of a sort code and future requirements

From the number of identifiable reaction channels in the previous section, it is fair to say that the reconstruction and the analysis code function correctly. A number of small bugs were found in the reconstruction (e.g. the number of energy hits and timing hits differed - this was a result of zero-suppression being included in the reconstruction code which was removing the timing values for obvious reasons). In addition, a sort code which allows for the analysis of SHARC/TIGRESS data has been developed along with a number of algorithms which will form the basis of future SHARC/TIGRESS analyses of this sort.

There is one outstanding area of concern in this regard. The decision as to which addback and suppression schemes to use for TIGRESS were based on the work of Schumaker *et al.* [69, 75]; the response of the DAQ will obviously play a role in the choice of which scheme should be used, as well as the background rate from the decay of scattered beam. Without an understanding of the DAQ performance, however, it is not possible to provide guidance for future experiments as to which scheme should be implemented in the post-experiment analysis, and as to whether high-efficiency or high-suppression modes should be used during the experiment.

6.2 Pad calibration

The pad calibration approach used failed to perform its function during the experiment. This has led to a poor energy calibration for any SHARC events with particle ID. A new calibration scheme has been adopted in subsequent experiments, based on that which is already in use for T-REX [83]. In this system, a γ -ray source is placed near the array and data are taken with the pad detectors and the germanium array which surrounds T-REX. Compton-scattering of the incident γ rays deposits some energy in the pad detector before scattering into the germanium detector. The energy deposited in the pad detector should be equal to the energy of the initial γ ray less the energy deposited in the germanium detector. This allows the pad detector to be calibrated. During the test experiment, γ calibration data were not taken with all slaves enabled, meaning that the only data which include both germanium detectors and pad detectors is online data. Investigations were carried out as to whether the beam data could be used in this fashion to calibrate the pad detectors; no clear loci were visible to use for calibration, however.

6.3 Technical problems - preamplifiers and timing

A large amount of potentially useful data was lost due to the preamplifier saturation. Fortunately, this effect was noticed during the experiment and in time to prevent problems with preamplifiers causing problems with subsequent SHARC/TIGRESS experiments. The issue was easily identified and modifications carried out to correct the problem.

DAQ timing issues were deeply problematic for this experiment. Figure 6.1 shows a raw γ -ray spectrum for beam data. These are data taken while the beam was running using a silicon singles trigger. The level of background is obvious. Weak reaction channels without any other form of gating (such as a 0-degree detector as described below) can easily be lost in the background from decaying scattered beam. A leading-edge discrimination timing algorithm has now been implemented in the DAQ and will be available for use in future experiments.

6.4 Fusion-evaporation

Experiments using compound targets have been attempted with SHARC/TIGRESS before [65]. In that case, a trifoil scintillator ‘0-degree’ detector was used to suppress fusion-evaporation products from reactions with carbon in the CD_2 target. In front of the trifoil was a thin degrader foil which prevented fusion-evaporation products reaching the trifoil detector. This reduced the number of fusion-evaporation products to a manageable level. The trifoil can only be used with low-intensity beam currents and the efficiency of the trifoil can be reduced due to damage caused by scattered beam.

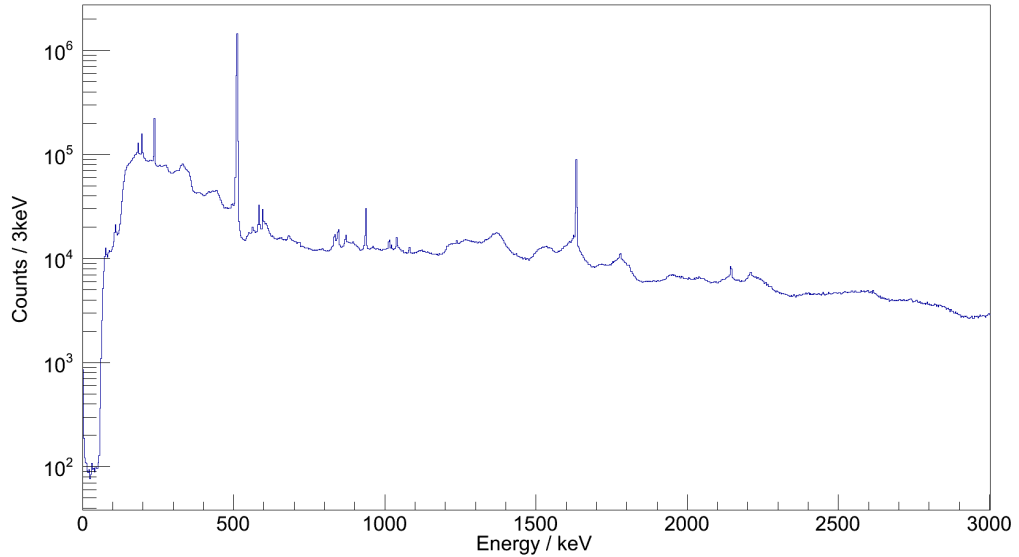


Figure 6.1: Raw γ -ray spectrum from beam data - trigger was silicon singles. Log scale on the y -axis.

The simplest solution to this problem of recoil detection would be to use EMMA, the Electro-Magnetic Mass Analyser which is being constructed at TRIUMF and is designed to couple to TIGRESS [84]. This detector would allow for identification of reaction products, and would allow for suppression of unwanted fusion-evaporation. However, the construction of EMMA has not yet been completed so stop-gap measures are required if the ^{15}O experiment is to run in the near future.

It has been proposed that SHARC/TIGRESS be coupled with an additional annular silicon detector which will cover small angles (the ‘0-degree silicon detector’) [85]. The principle of operation in this case is almost identical to that of the trifoil: a thin degrader foil will stop unwanted fusion-evaporation reaction products from reaching the detector, as shown in fig. 6.3 while scattered beam and ^{19}Ne reaction products will punch through the foil and cause a signal in the 0-degree detector. In order to select the events of interest, an upstream deuteron must be detected in coincidence with a ^{19}Ne in the 0-degree detector and a γ -ray must be detected in TIGRESS. Figure 6.2 shows the relationship between the deuteron emission angle and the ^{19}Ne recoil angle for reactions to the 4033-keV state in ^{19}Ne . The angles covered by the upstream CD and box of SHARC which correspond to peripheral interactions and the angles covered by the 0-degree detector, if placed 40-cm downstream of the target, are marked. It is clear that the combination of SHARC upstream and the 0-degree detector downstream cover most of the relevant angles.

To demonstrate the modus operandi of the 0-degree detector, the case of ^{15}O at 5 MeV/u with a 20- μm thick aluminium degrader in front of the 0-degree detector is consid-

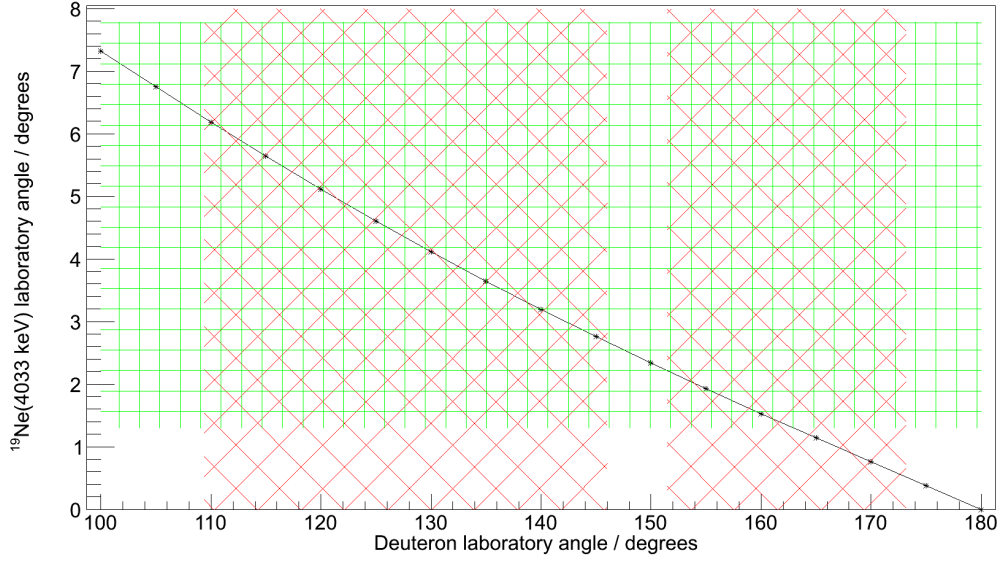


Figure 6.2: Deuteron angle vs. recoil angle for $^{15}\text{O}(^6\text{Li},d)^{19}\text{Ne}(4033\text{ keV})$ at 5 MeV/u. SHARC coverage for the upstream CD and box is shown by the red diagonal-hatched boxes, whilst the 0-degree detector coverage is shown by the green Cartesian-hatched boxes.

ered.¹ The ^{15}O is assumed to scatter elastically at 4° having an energy of 74.09 MeV. The $^{15}\text{O}(^6\text{Li},d)^{19}\text{Ne}$ reactions (at the same angle) are assumed to populate the 4.033-MeV state in ^{19}Ne , the recoils have an energy of 67.56 MeV. Using the same range-energy method as described in section 5.6.1, the energy loss of ^{19}Ne and ^{15}O passing through the foil can be considered. This leaves the ^{15}O with around 64 MeV remaining while the ^{19}Ne has around 28 MeV remaining. This should allow for one improvement on the trifoil system which cannot distinguish between scattered beam and reaction products; a silicon detector used for 0-degree detection should allow for selection of reaction products, reducing the false coincidences between scattered beam and light ions hitting the upstream detectors.

For a 5 MeV/u ^{15}O beam on a ^6LiF target, PACE [82] suggests that the main fusion evaporation products from $^{15}\text{O}+^{19}\text{F}$ reactions will be ^{28}Si and ^{27}Al . For a 20 μm -thick aluminium degrader, ^{28}Si will need around 70 MeV to punch through the degrader, while ^{27}Al will need around 60 MeV. However, for both of these products, the maximum energy at around 4° is 55 MeV meaning that both will be stopped in the degrader.

¹Changing the beam energy would require a different degrader thickness. The current example is presented for illustrative purposes.

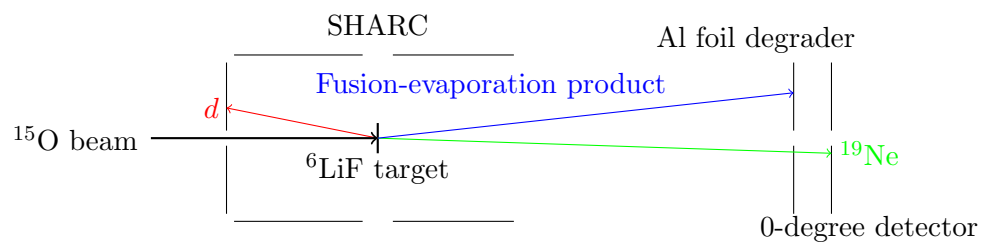


Figure 6.3: Diagram of the suggested new SHARC/TIGRESS experiment. The addition of the 0-degree detector helps to suppress fusion-evaporation background from the fluorine in the target.

Chapter 7

A test study of the $^{20}\text{Ne}(d,t)^{19}\text{Ne}$ reaction at the Munich Q3D spectrometer facility

7.1 Introduction

As discussed in chapter 3, the 4140- and 4197-keV resonances, lying at 611 keV and 668 keV above the α -threshold, could provide important contributions to the $^{15}\text{O}(\alpha,\gamma)^{19}\text{Ne}$ reaction rate. The spins of these resonances are still unknown which prevents accurate estimation of the contribution to the total reaction rate, as described in chapter 3; it may be possible to distinguish these states using the shapes of the angular distributions resulting from the $^{20}\text{Ne}(d,t)^{19}\text{Ne}$ reaction. In this chapter, the background to such a measurement is set out along with the results of a test experiment.

There are two related challenges to measuring these angular distributions. The first is the target: neon is a noble gas and does not form compounds; targets made from solid neon or solid-neon compounds are not practical. Gas cells introduce energy and angular straggling which limits the achievable energy resolution. Implanted targets allow for a superior energy resolution but the high beam currents which are required for this experiment can cause neon to migrate out of the target. The contaminant material, especially the carbon forming the bulk for the target into which the neon is implanted, can cause contaminant peaks in the excitation spectrum. This leads to the second problem: given that the 4140- and 4197-keV resonances lie close in energy, a magnetic spectrometer is required to separate the states. Magnetic spectrometers include optics which are set to correct for the reaction kinematics of the reaction of interest. Contaminant peaks will not undergo the correct optical correction and this results in broadened peaks falling on the focal plane and obscuring the peaks resulting from the reaction of interest. Whether cross sections from states in ^{19}Ne can be extracted will depend on the relative strengths

of population of the contaminant states and on how out-of-focus those states are.

While it is simple to calculate the positions of the contaminant states on the focal plane, the extent of the broadening cannot be calculated. Practically, the only way of determining whether the contaminants are problematic is to carry out test experiments.

For this reason, a test experiment was carried out at the Maier-Liebnitz laboratory in Munich. This involved a measurement of the $^{20}\text{Ne}(d,t)^{19}\text{Ne}$ reaction to investigate the strength and broadening of the contaminant states, to see if the states in ^{19}Ne would be visible over a useful range of angles to enable differentiation of J^π from the angular distributions. This test experiment took advantage of a $^{20}\text{Ne}(d,p)^{21}\text{Ne}$ experiment which was being run at the same facility.

After the setup has been described, there is a discussion of the analysis of data taken with the Q3D, and a summary of results.

7.2 The targets

A number of neon-implanted targets were available during the experiment; only two were used. These targets, which consisted of ^{20}Ne implanted in $40 \mu\text{g}/\text{cm}^2$ ^{12}C were made by the target production group at the Helmholtz Zentrum Dresden-Rossendorf by irradiation of a ^{12}C foil with a ^{20}Ne beam. Irradiation was performed at 20 and 30 keV and a dose of $5 \times 10^{16} / \text{cm}^2$ from both sides of the target (4 implantations in total) with a total dose of $2 \times 10^{17} / \text{cm}^2$. This corresponds to an areal density of ^{20}Ne of around $7 \mu\text{g}/\text{cm}^2$. The nominal properties of all of the ^{20}Ne -implanted targets available are laid out in table 7.1.

Target origin	Neon areal density / $\mu\text{g}/\text{cm}^2$	Carbon foil areal density / $\mu\text{g}/\text{cm}^2$
Dresden (3 targets)	7	40
Yale	4.67	40
Yale	18	40
Yale	14	40
Yale	6.3	40
Seattle	3-6	30
Oak Ridge	7.6	40

Table 7.1: ^{20}Ne -implanted targets available during the experiment. All target backings were ^{12}C apart from the Seattle target which was $^{\text{nat}}\text{C}$.

7.3 Beam production

Deuterons of 22 MeV were produced by the MML tandem accelerator. An ion source is used to form ${}^2\text{H}^-$ ions, which are repelled from the ion source and into the accelerator by virtue of a bias applied to the terminal electrode. The high-voltage terminal at the centre of the accelerator attracts the negatively-charged ions towards it. The stripper foil at the centre of the accelerator removes the electrons from the ${}^2\text{H}^-$ ions, leaving ${}^2\text{H}^+$ ions which are repelled from the high voltage terminal. This arrangement means that the same accelerating voltage is used twice. The energy of the deuteron resulting from the tandem will be $E_{\text{beam}} = 2eV_{\text{terminal}} + eV_{\text{source}}$ where e is the charge on the electron. The source voltage was 640 kV and the terminal voltage 10.68 MV, giving a total beam energy of 22 MeV in this case.

7.4 The Munich Q3D

The Munich Q3D (quadrupole, 3 dipoles) is a magnetic spectrometer located at the Maier-Liebnitz Laboratory at TUM. Magnetic spectrometers allow a determination of the energy of reaction products by measuring the position of the products on the focal plane of the detector, as explained below. While magnetic spectrometers have a number of limitations the good energy resolution achievable in them enables extremely precise charged particle spectroscopy.

7.4.1 Magnetic spectrometers

The basic principle of magnetic spectrometers is that the reaction products are distributed on the focal plane based on their magnetic rigidity, $B\rho$. This magnetic rigidity is a measure of the resistance of a charged particle to deviation in a magnetic field. A charged particle (of charge q) in a magnetic field of strength and direction \underline{B} feels a force, \underline{F} , perpendicular to the velocity \underline{v} , given by:

$$\underline{F} = q\underline{v} \wedge \underline{B}. \quad (7.1)$$

If the field and the velocity are perpendicular, then eq. (7.1) simplifies to give:

$$F = qvB. \quad (7.2)$$

Therefore, the particle can be described as travelling in a circle of radius ρ . A particle of mass m travelling with a velocity v in a circle of radius ρ must feel a force of magnitude:

$$F = \frac{mv^2}{\rho}. \quad (7.3)$$

Equating eq. (7.2) and eq. (7.3), rearranging and using the non-relativistic definition of momentum ($p = mv$) gives:

$$B\rho = \frac{p}{q}. \quad (7.4)$$

All of the reaction products are subject to the same field in the dipole so products with different momenta will travel in circles of different radii. The orbits of the products are interrupted by a position-sensitive detector which gives focal-plane position. This position gives a measurement of ρ , allowing the momentum and thus energy to be calculated.

The Munich Q3D contains three dipoles to achieve this separation according to rigidity. In addition to these dipoles, there is a quadrupole and a multipole. The quadrupole focusses in the vertical direction and has the effect of pulling reaction products into the spectrometer, increasing the effective solid angle. The multipole consists of a number of elements (quadrupole, sextupole, octupole and decapole) to correct the kinematic broadening due to the finite aperture size [86].

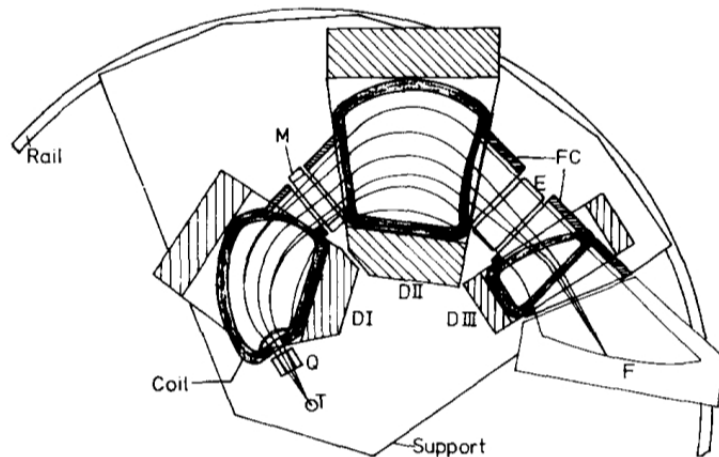


Figure 7.1: Schematic diagram of the Munich Q3D [87]. T: target, Q: quadrupole, D: dipole, M: multipole, F: focal plane, FC: field clamp, E: electrostatic deflector.

7.4.2 Focal-plane detectors

The focal-plane detectors must serve two purposes: identification of the reaction products (by differential energy loss) and determination of the focal-plane position of the interaction. The Munich Q3D uses three focal-plane detectors, two multi-wire proportional counters (MWPCs) and a scintillator. Scintillators have been discussed previously (see section 4.4). In this case, the scintillator is NE104 of $7 \times 14 \text{ mm}^2$ cross section [88]; NE104 has a 1.8 ns decay time, enabling it able to deal with high rates [62]. The arrangement of the focal plane detectors is shown in fig. 7.2

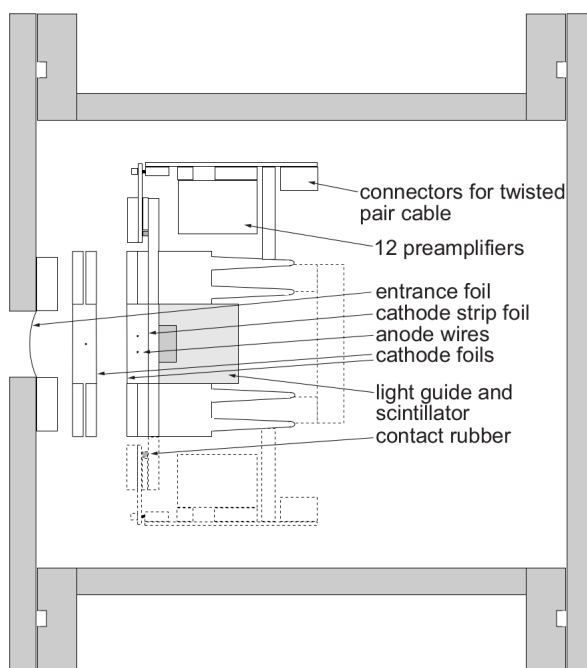


Figure 7.2: A side-on schematic showing the focal plane detectors of the Munich Q3D, looking along the focal plane. Particles enter from the left [88].

MWPCs consist of an anode and a cathode over which a bias voltage is applied. Charged particles passing through the gas cause ionisation. The electrons produced are accelerated towards the anode, causing additional ionisation and increasing the signal amplitude. The charge collected on the anode provides a measurement of the energy deposited. In the second Q3D MWPC, there are two anode wires which run lengthways down the focal plane and a segmented cathode, as shown in figs. 7.2 and 7.3. A segmented cathode is used to find the focal plane position. Signals are induced on the cathodes by the electron avalanche around the anode; the signals induced are spread over a number of strips. By fitting the magnitude of the collected charges with a Gaussian, as shown in fig. 7.4, the focal-plane position can be found to higher precision than the strip width.

7.5 Taking data

The aim of the experiment is to extract angular distributions of tritons from the $^{20}\text{Ne}(d,t)^{19}\text{Ne}$ reaction. In order to do this, the yield to states is measured at various different angles. At each angle, the dipole fields are set so that the same excitation energy is at the centre of the focal plane and the multipole fields are set to correct for the kinematic broadening. Obviously, for reactions off the contaminant carbon and oxygen nuclei, the kinematic dependence on angle will be different from that for the neon. The states resulting from (d,t) reactions on ^{12}C , ^{16}O and ^{20}Ne are tabulated in table 7.2.

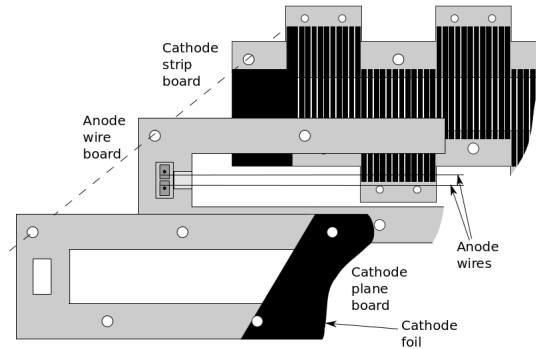


Figure 7.3: A schematic of the second (position) MWPC at the Munich Q3D focal plane. The middle board shows the two anode wires while the back board shows the cathode strips used to determine the focal plane positions. The front board is the cathode foil of the second MWPC (c.f. fig. 7.4) [88]. Additional labels have been added to the diagram.

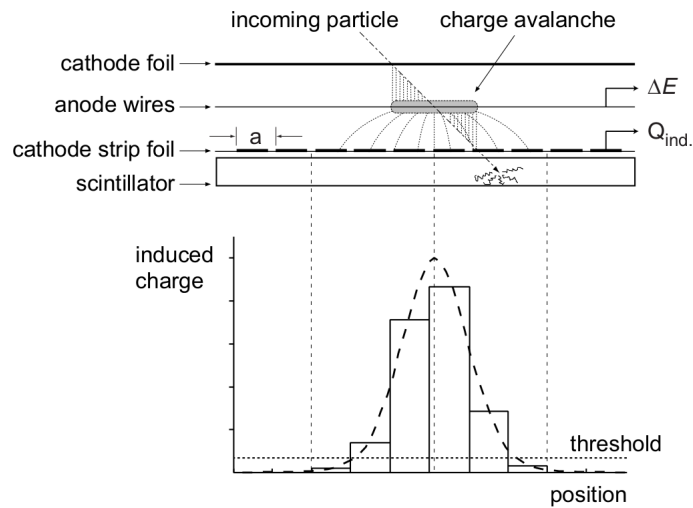


Figure 7.4: A schematic showing how the second MWPC at the focal plane of the Munich Q3D allows the focal-plane position of reaction products to be determined [88].

Figure 7.5 shows the rigidities for these states as a function of angle. From this, it is clear that contaminant states move along the focal plane when the angle is changed¹, while the states from the species of interest remain stationary since the magnitude of the magnetic field is chosen to ensure this.

Final Nucleus	Energy Level / MeV	J^π	ℓ
¹⁹ Ne	4.033	$3/2^+$	2
¹⁹ Ne	4.140	$7/2^-, 9/2^-$	3,5
¹⁹ Ne	4.197	$7/2^-, 9/2^-$	3,5
¹¹ C	2.000	$1/2^-$	1
¹⁵ O	5.183	$1/2^+$	0
¹⁵ O	5.241	$5/2^+$	2

Table 7.2: Energies, J^π and ℓ -values for relevant states in ¹⁹Ne, ¹⁵O and ¹¹C.

Using the yield, Y , to a state at a particular angle, the differential cross section can then be extracted taking account of the DAQ and focal-plane livetime fractions, η and ϵ , aperture solid angle, $\Delta\Omega$, target areal density, N , and total beam current on target, I , by:

$$\frac{d\sigma}{d\Omega} = \frac{Y}{NI\eta\epsilon\Delta\Omega} \quad (7.5)$$

7.5.1 Data acquisition

The DAQ is triggered by signals in both MWPCs and the scintillator.² The charge collected on the MWPC anodes and the scintillator are recorded, along with the charge collected on each cathode strip in the second (position) MWPC. At the end of each run, two scalers are output. These are ‘scaler1’, a measure of the integrated beam current on the target, and ‘scaler3’, a measure of the deadtime. Scaler1 is connected to the Faraday cup that acts as the beam dump, and outputs a pulse after a certain amount of charge has been incident on the cup; in this case, it was set to give a pulse every 2 μC . When the DAQ fires, the scaler pulses are fed into another scaler (scaler3) in addition to scaler1 until the DAQ is able to accept signals again. The DAQ fractional livetime is then given by $\eta = 1 - \frac{\text{scaler3}}{\text{scaler1}}$.

After the DAQ has fired, the cathode signals must be read out and evaluated as to whether the event is a valid one. If a cathode goes over the signal threshold, it sends a signal to the readout module. The readout module then scans adjacent strips for signals that are above threshold. If between three and seven neighbouring strips show signals above threshold, then the signal is considered valid.³ The position information is then

¹I.e. that the $B\rho$ of the contaminant changes relative to the $B\rho$ of the excitation energy in ¹⁹Ne chosen to be at the centre of the focal plane.

²For ³He and α s, the DAQ can be run so that the scintillator is not required for the trigger [88].

³These are typical values for reaction products hitting the focal plane at 40-50° [88].

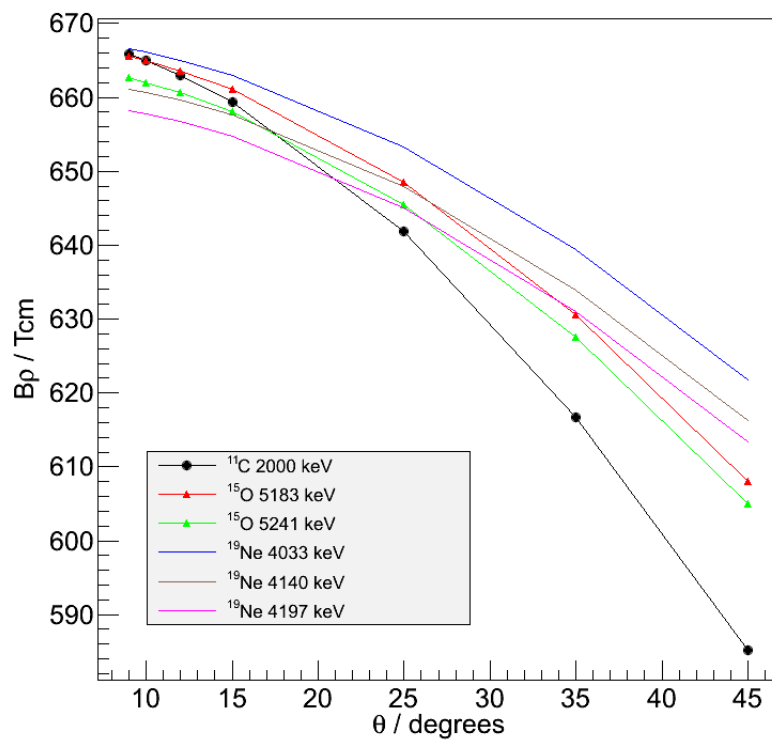


Figure 7.5: Rigidities for various states at various angles. The relative movement of the states from reactions involving different mass nuclides can clearly be seen.

added to the DAQ output by the readout module. If the readout module is busy with a previous event, or the event has the wrong strip multiplicity, then the readout module does not give position information, returning a value of 0. Therefore, the focal plane deadtime fraction can be found by considering the number of hits of the focal plane and the number of hits in the 0-bin on the focal-plane position spectrum (or equivalently, considering the number of events with multiplicity of zero as a fraction of the total events).⁴ If D is the number of events with a multiplicity of zero and T is the total number of events, then the focal plane fractional livetime is given by $\epsilon = 1 - \frac{D}{T}$.

7.6 Processing the data

Unlike the situation when analysing the SHARC/TIGRESS data when the author was required to develop a new sort code, the Munich Q3D has a dedicated sort code, Marabou, which processes the online spectra and does the Gaussian fitting of the peak positioning. This code allows for two cuts to be made for the purposes of particle identification by differential energy loss, one on the first anode charge against the second anode charge, and the other based on one anode charge against the scintillator charge. In this case, in an attempt to suppress the background due to contaminants and other reaction products, a modified version of Marabou was used which allows a greater number of cuts to be applied to the data [89].

7.6.1 Calibrating the focal plane

The focal plane of the Q3D must be calibrated so that each focal-plane position can be used to give the excitation energy of the recoil. In addition, while the focal plane should be almost linear in momentum, small deviations from linearity might be present due to variations in the detector readout or the optics. In this case, no calibration data were taken using the (d,t) reaction and the calibration data for the main (d,p) experiment are used for this purpose. In this case, the focal-plane positions of peaks from the $^{28}\text{Si}(d,p)^{29}\text{Si}$ reaction with the spectrometer at 8° are matched to the respective rigidities of the states, and the parameters describing this fit extracted. This results in a function that converts focal plane position to rigidity.

Knowing the rigidity ($B\rho$) and the magnetic field strength allows ρ , the radius of curvature, at each focal plane position to be calculated. In this case, therefore, the calibration converting focal-plane position to rigidity using $^{28}\text{Si}(d,p)^{29}\text{Si}$ at 8° can be modified to convert focal-plane position to rigidity for other reactions at other angles using:

$$B_{\text{experimental}}\rho = f(x)\frac{B_{\text{experimental}}}{B_{\text{reference}}} \quad (7.6)$$

⁴Note that the only values of strip multiplicity that can be returned are 0 and 3-7.

where $f(x)$ is the function converting focal plane position (x) to rigidity [90], $B_{\text{experimental}}$ is the magnetic field for the particular angle being investigated and $B_{\text{reference}}$ is the reference field at 8° for the (d,p) reaction.

7.6.2 Identifying Reaction Products and States

To analyse the data, a number of steps are required: first of all, the reaction products must be identified. Once this has been done, the various features seen on the focal plane can be explained and, if the desired state can be identified, a yield extracted by fitting the area of the peak. This yield can then be used to extract a cross section.

Reaction products were identified using the charges on the MWPC anodes and the charge from the scintillator. The principle, that of using differential energy loss, is the same as was discussed section 4.5.4. In this case, a gate is placed on the two anode charges, shown in fig. 7.6, and on each anode charge and the scintillator charge, as shown in fig. 7.7.

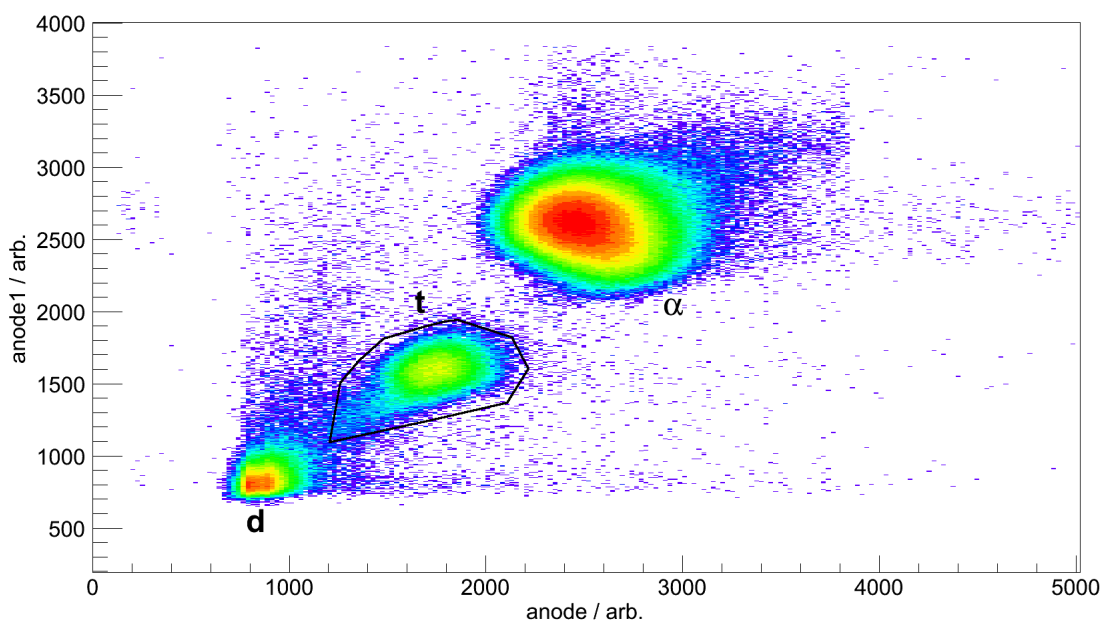


Figure 7.6: First anode charge against second anode charge for data taken with a neon-implanted carbon foil at 12° . The gate is placed around the triton locus. The deuteron and α loci are also marked.

In order to observe when the contaminant peaks obscure the ^{19}Ne peaks, the calibrated $B\rho$ spectra have been plotted for 10° , 12° , 15° , 25° and 35° in figs. 7.8 to 7.12. The rigidities for the 4033-, 4140- and 4197-keV states in ^{19}Ne are marked by a black square, a red circle and a green triangle respectively. Other focal plane features where extant are identified in the figure captions where appropriate.

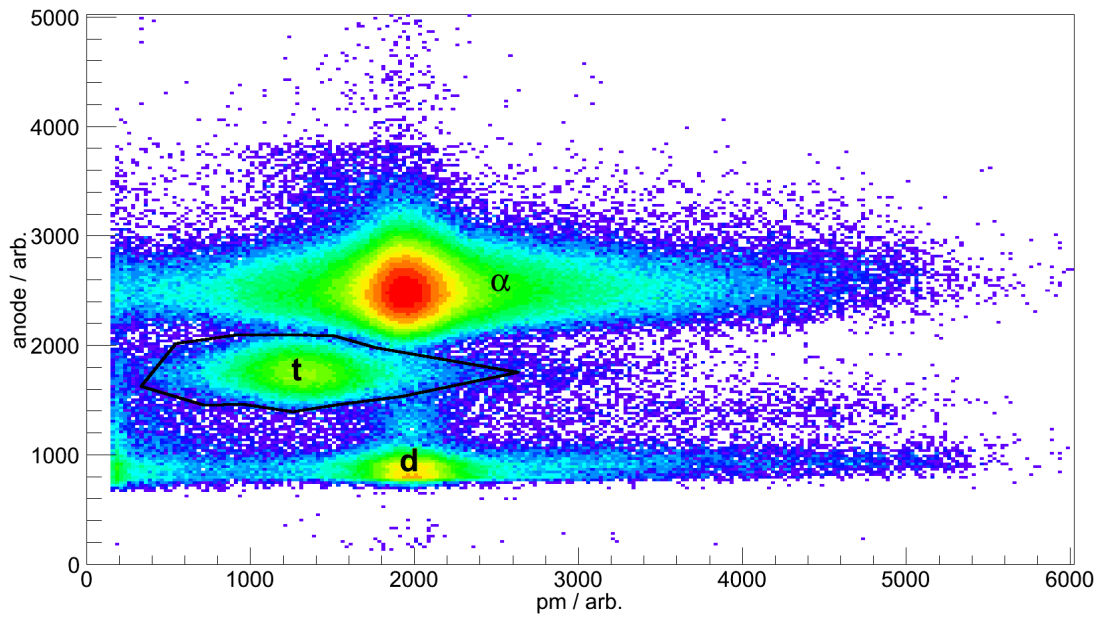


Figure 7.7: Anode charge against plastic scintillator charge for data taken with a neon-implanted carbon foil at 12° . The gate is placed around the triton locus. The deuteron and α loci are also marked.

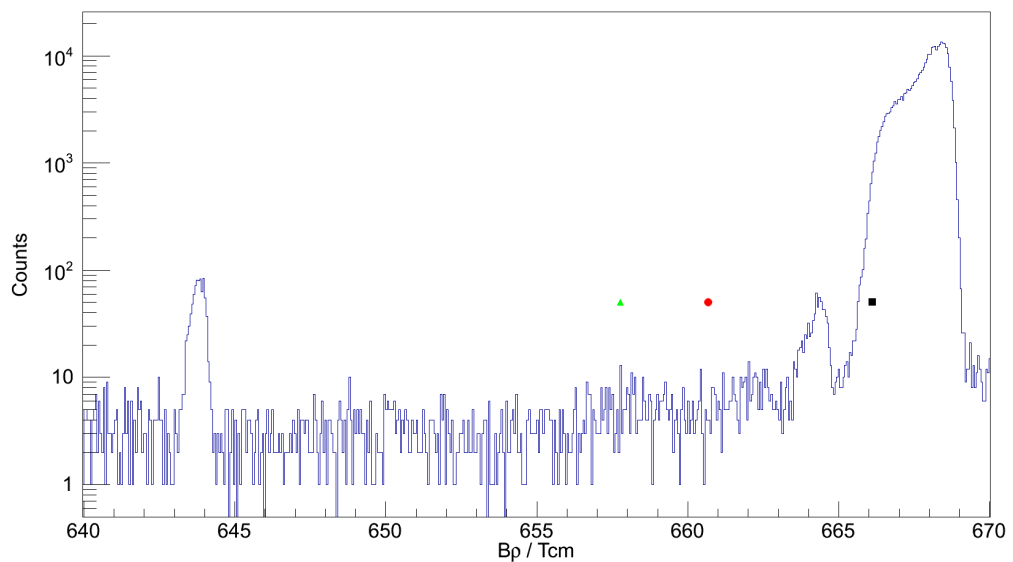


Figure 7.8: $B\rho$ spectrum at 10° . The peak at around 644 Tcm is due to α s from the ^{10}B ground state, which is discussed in more detail in section 8.4.1. The large defocussed peak from around 665 to 669 Tcm is the 2-MeV state in ^{11}C . The small peak at around 664 Tcm is due to one of the states in ^{15}O . The rigidities of states in ^{19}Ne are marked; black square, 4033 keV; red circle, 4140 keV; green triangle, 4197 keV.

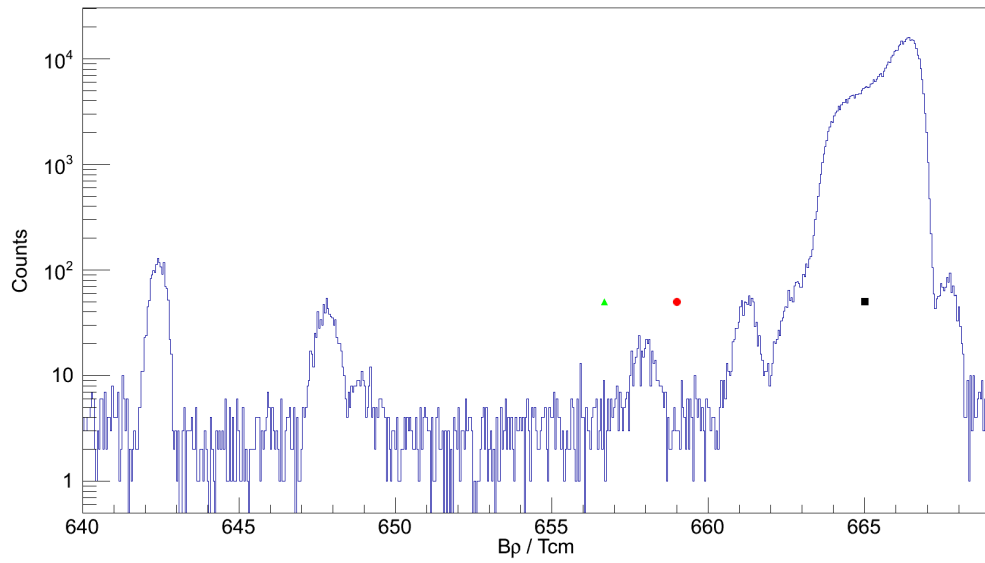


Figure 7.9: $B\rho$ spectrum at 12° . The ^{10}B ground state, 2-MeV state in ^{11}C and the 5.183- and 5.241-MeV states in ^{15}O are all visible, along with the 4.138-MeV state in ^{27}Si . The rigidities of states in ^{19}Ne are marked; black square, 4033 keV; red circle, 4140 keV; green triangle, 4197 keV.

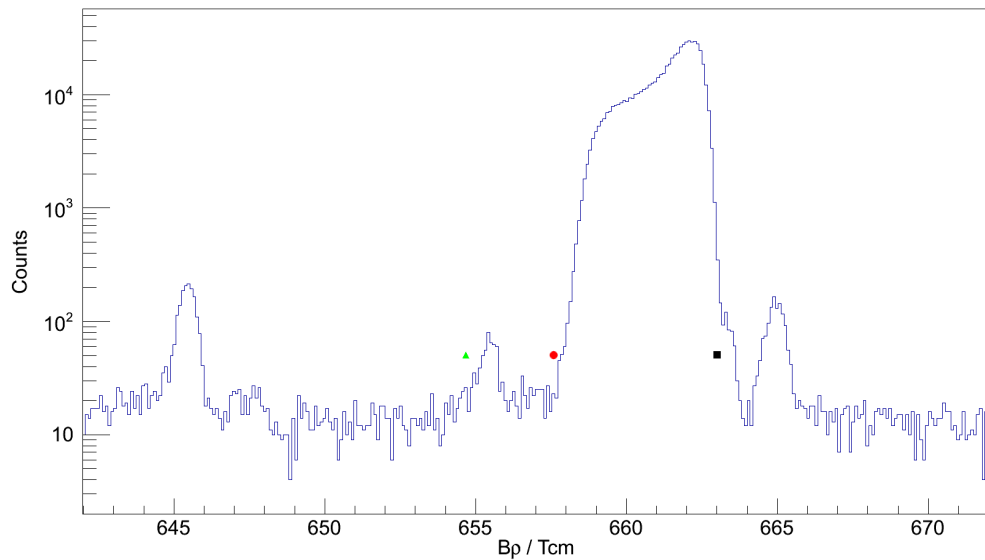


Figure 7.10: $B\rho$ spectrum at 15° . The ^{11}C 2-MeV state now overlaps the 4140-keV state in ^{19}Ne . The rigidities of states in ^{19}Ne are marked; black square, 4033 keV; red circle, 4140 keV; green triangle, 4197 keV.

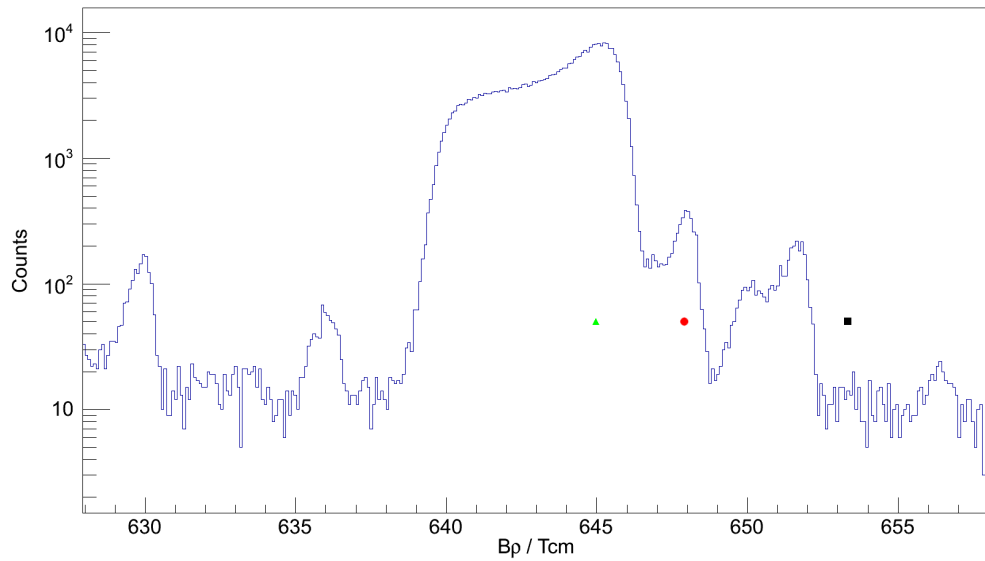


Figure 7.11: $B\rho$ spectrum at 25° . The ^{11}C 2-MeV state now overlaps both the 4140- and 4197-keV states in ^{19}Ne . The rigidities of states in ^{19}Ne are marked; black square, 4033 keV; red circle, 4140 keV; green triangle, 4197 keV.

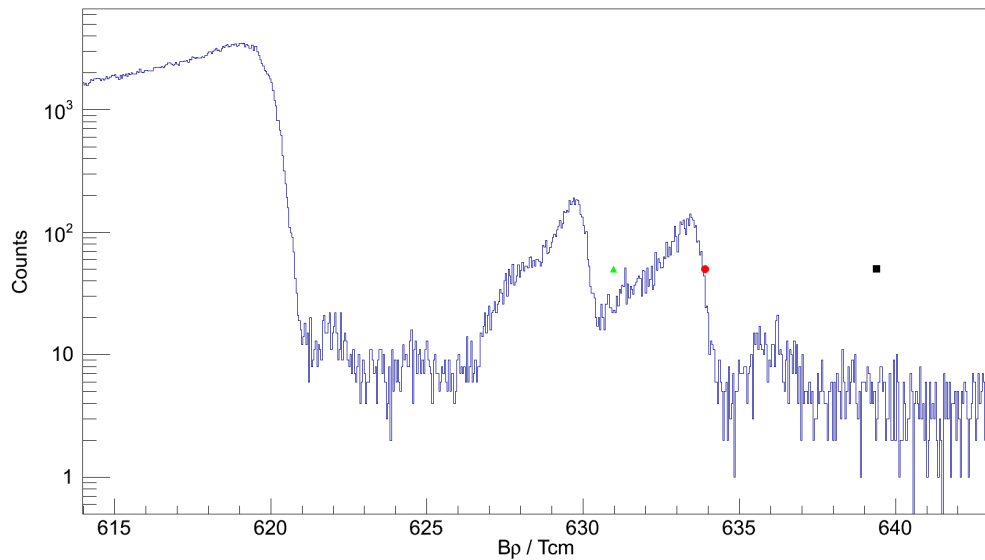


Figure 7.12: $B\rho$ spectrum at 35° . The ^{11}C 2-MeV state has now moved past both the 4140- and 4197-keV states in ^{19}Ne . However, two more defocussed peaks (likely the ^{15}O doublet) are now overlapping the positions of the ^{19}Ne doublet. The rigidities of states in ^{19}Ne are marked; black square, 4033 keV; red circle, 4140 keV; green triangle, 4197 keV.

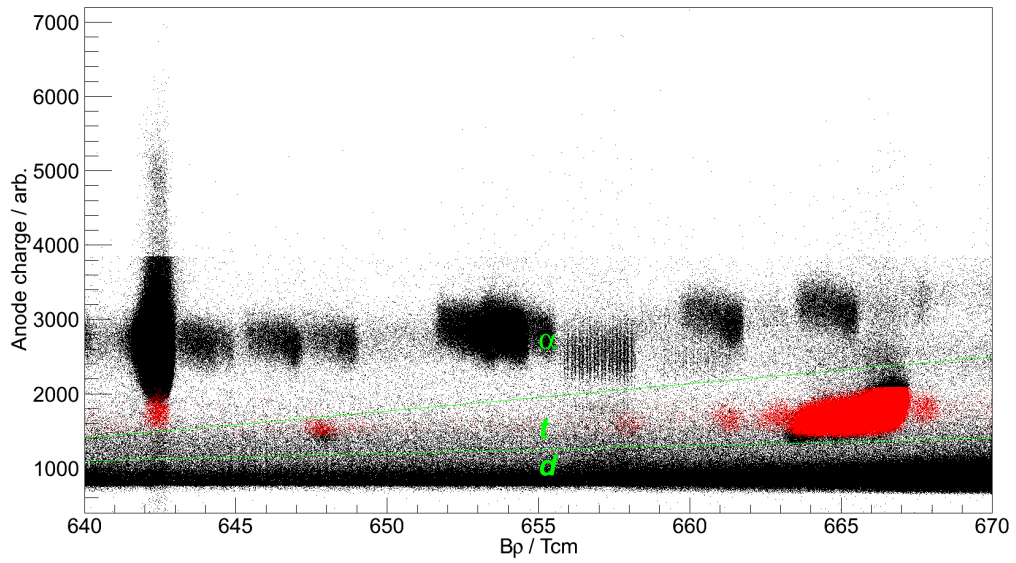


Figure 7.13: Position against anode charge collected for 12° without (black) and with (red) the triton gates on data from a neon-implanted carbon foil. Heavier ions and ions with a higher atomic number deposit more energy in the MWPC. The approximate bands of scattered deuterons, tritons and α s are marked on the plot.

It is clear from figs. 7.8 to 7.12 that the ^{19}Ne states are obscured at many angles. The impact of this on the feasibility of this experiment is discussed in the next chapter.

Chapter 8

Discussion of the Munich tests

8.1 Introduction

The Munich experiment, as previously described, was designed to test whether neon-implanted targets can be used to study states in ^{19}Ne via $^{20}\text{Ne}(d,t)^{19}\text{Ne}$. There are two main experimental factors which must be accounted for: loss of neon from the target due to target heating, and whether reaction products from target contaminants obscure the species of interest on the focal plane. In the previous chapter, the experimental equipment was discussed along with the results from the experiment. In this chapter, a number of possible changes are laid out which may allow the experiment to proceed.

8.2 Contaminant peaks

The results of the analysis in the previous chapter are not encouraging. It is clear that the contaminant states are much more strongly populated than the ^{19}Ne states. In addition, the large level of broadening of the peaks obscures large sections of the focal plane

Figures 7.8 to 7.12 demonstrate that the only angles at which the peaks can be separated from the background are below around 12° and at some point above 35° . DWBA calculations performed with the commonly-used Ptolemy DWBA code are shown in fig. 8.1. In order to ascertain the ℓ -value of the reaction, the shape of the distribution must be known and compared to calculations. In this case, it is clear that angular distributions will be obscured by contaminants for much of the useful angular range for this purpose, with the remaining angular range much too small to be used to distinguish the spins. There may be additional complicating factors due to multistep components in the reaction; inelastic excitations in the entrance channel have been shown to contribute to the angular distribution for $^{20}\text{Ne}(d,^3\text{He})^{19}\text{F}$ reactions [91]. If this is the case, as is probable, then the angular distribution must be observed over the range obscured by the ^{11}C 2-MeV state and other contaminants in order to understand this multistep contribution.

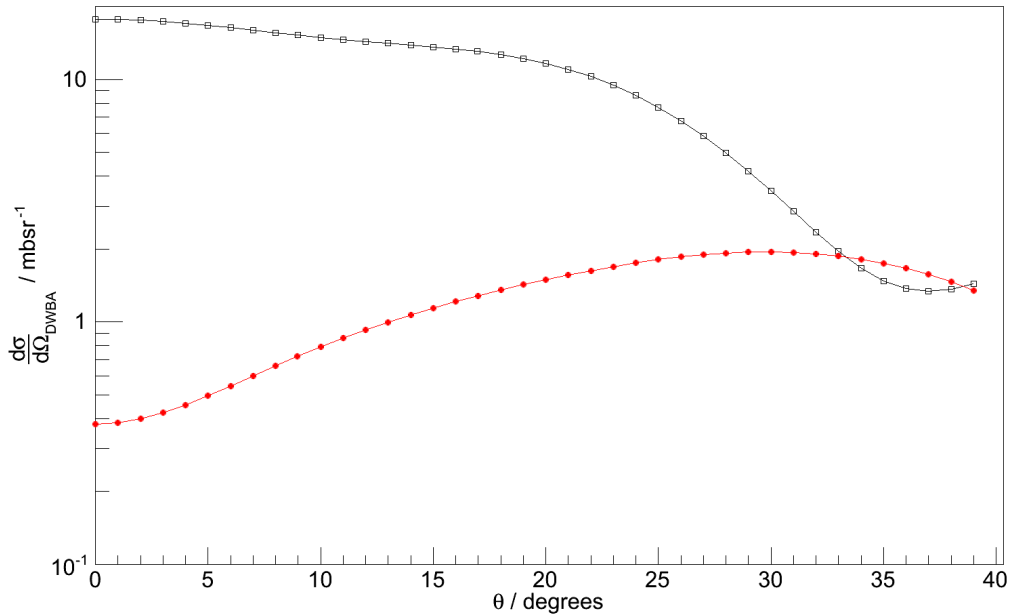


Figure 8.1: DWBA angular distributions of $7/2^-$ (empty black square) and $9/2^-$ (filled red circles) states in ^{19}Ne , assuming $C^2S = 1$ (see section 2.3). Both distributions are calculated assuming transitions to the 4140-keV state in ^{19}Ne .

8.3 Neon leakage from the target

Given the conclusions above, no checks have been made concerning the stability of the neon within the targets. During the experiment, the effect of changing to a new target was clearly seen in the $^{20}\text{Ne}(d,p)^{21}\text{Ne}$ data; it is hoped that the results from that experiment will allow for quantification of the neon leakage during the experiment. In this case, this information is not particularly helpful as the present experiment cannot proceed with neon-implanted carbon foils as targets.

8.4 Possible solutions

Given that the measurement will not be possible with the current targets, a number of improvements to the experimental method can be proposed, along with other techniques which may help to resolve the J^π assignments in ^{19}Ne . These proposals can be summarised in two sections: firstly, a change of target backing and, secondly, a switch to a different reaction.

8.4.1 Targets

The major problem with the targets was the strong contaminant lines from ^{11}C and ^{15}O , the tritons from which have approximately the same rigidity as the tritons from ^{19}Ne states. In addition, the high cross section for $^{12}\text{C}(d,\alpha)^{10}\text{B}(\text{g.s.})$ results in a very high rate on the focal plane. While this peak is not badly out of focus, it causes large amounts of focal-plane deadtime, and thus limits the maximum beam intensity that can be used.

When combined, these factors provide a strong case for changing the backing material for the implanted targets. Silicon, which has been used previously in other studies, is a possible choice. In this case the usable beam intensity might be limited by the rate due to $^{28}\text{Si}(d,\alpha)^{26}\text{Al}$ reactions but the tritons from reactions to the 4140- and 4197-keV states are less likely to be affected by contaminant tritons from ^{27}Si .

Changing the target backing will require further tests to be made with the new targets in order to check for contaminants and for target stability. In particular, carbon build-up from oil cracking onto the target or from oxygen in water vapour suggest it might be necessary to provide a cooled shield around the target.

8.4.2 (d,t) vs. $(^3\text{He},^4\text{He})$

There are three common neutron pick-up reactions: (p,d) ¹, (d,t) and $(^3\text{He},^4\text{He})$. Considering the neutron pick-up reaction from ^{20}Ne , there are a number of advantages of using $(^3\text{He},^4\text{He})$ over (d,t) .

Firstly, the Q-value for $^{20}\text{Ne}(d,t)^{19}\text{Ne}(\text{g.s.})$ is -10.608 MeV while that for $^{20}\text{Ne}(^3\text{He},^4\text{He})^{19}\text{Ne}(\text{g.s.})$ is +3.712 MeV. With the beam energies at Munich, the (d,t) reaction is only just energetically possible, while the $(^3\text{He},^4\text{He})$ reaction, for which a higher beam energy is possible (33 MeV as opposed to 22 MeV for deuterons with the same terminal voltage) in addition to the more favourable Q-value, can comfortably proceed.

Secondly, as mentioned in the previous section, the $^{12}\text{C}(d,\alpha)^{10}\text{B}(\text{g.s.})$ channel causes large amounts of deadtime in the system. This will obviously not be a problem if ^3He replaces the deuteron as the projectile.

Finally, the states of interest are populated by $\ell = 3$ and $\ell = 5$ transfers. Following standard semi-classical arguments [38] which were discussed in section 2.5.1, the ℓ -values favoured for each transfer can be calculated as a function of bombarding energy. The comparison between $^{20}\text{Ne}(d,t)^{19}\text{Ne}$ and $^{20}\text{Ne}(^3\text{He},^4\text{He})^{19}\text{Ne}$ was used as an example in section 2.5.1. The resulting plot of qR against bombarding energy, where q is the linear momentum transfer and R is the nuclear radius, is repeated in fig. 8.2. It is clear that the $(^3\text{He},^4\text{He})$ reaction favours higher ℓ -values, as is required by this experiment.

In conclusion: the more favourable kinematics, the reduction in unwanted reaction

¹The Munich tandem is not able to produce a proton beam that is energetic enough to allow this reaction. It has been excluded from the discussion in this section.

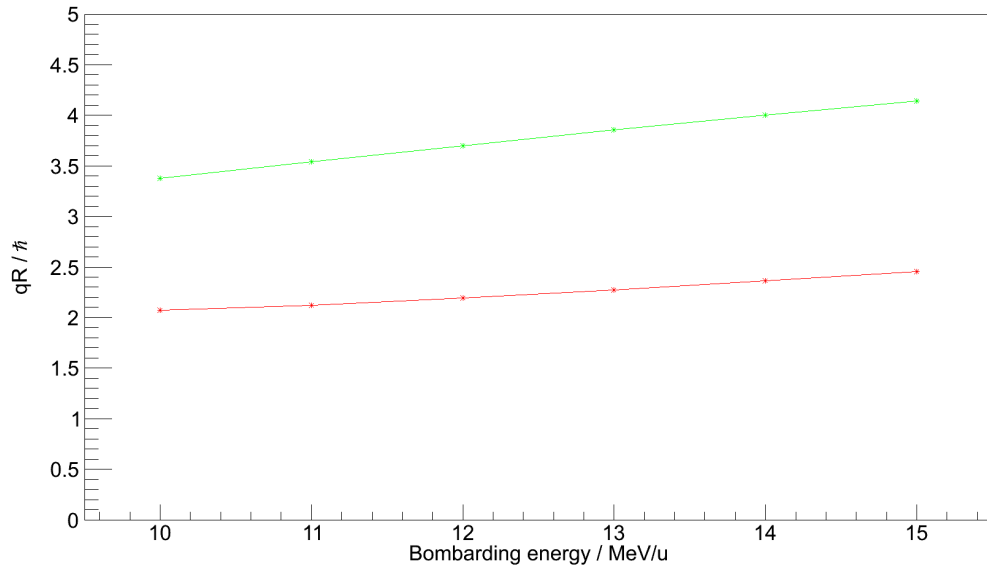


Figure 8.2: Plot of qR as a function of bombarding energy for $^{20}\text{Ne}(d,t)^{19}\text{Ne}(4.033\text{ MeV})$ (red) and $^{20}\text{Ne}(^3\text{He},^4\text{He})^{19}\text{Ne}(4.033\text{ MeV})$ (green). In this case, the angle is assumed to be 15° in both reactions.

channels, and the ℓ -value considerations suggest that if this experiment is to proceed, a different projectile - namely ^3He - should be used.

Chapter 9

Measuring branching ratios using coincidences between the Orsay Enge spectrometer and silicon detectors

9.1 Introduction

In the longer term, an accurate direct measurement of the α branching ratios of α -unbound states in ^{19}Ne would reduce one of the major uncertainties in the calculation of the $^{15}\text{O}(\alpha,\gamma)^{19}\text{Ne}$ reaction rate; for an example of a previous attempt, see Ref. [58] and references therein. States in ^{19}Ne can be populated via a transfer reaction, $^{19}\text{F}(^3\text{He},t)^{19}\text{Ne}$ being the simplest¹ reaction for this purpose, followed by coincident observation of decay α s; the ratio of the number of decays detected to the yield to a particular excited state is a direct measure of the branching ratio. The small energy separation of some of the states in ^{19}Ne , especially the previously described 4140/4197-keV doublet, favours the use of a magnetic spectrometer to detect the reaction tritons for the purpose of identifying the populated state; α -particles from the decay of the populated state are then detected by an array of silicon detectors around the target position.

In preparation for a study of this type both for applications to the case of ^{19}Ne and other charged-particle branching ratios of astrophysical interest, a new coincidence measurement setup has been developed at the Orsay accelerator facility, utilising the Orsay Enge spectrometer. The initial tests and commissioning experiment of the setup were

¹Most other reactions populating states in ^{19}Ne require neon targets, $^{20}\text{Ne}(^3\text{He},^4\text{He})^{19}\text{Ne}$ or $^{21}\text{Ne}(p,t)^{19}\text{Ne}$ for example, which suffer from the limitations of gas cells or implanted targets described in the previous chapter, or involve radioactive ion beams which have lower intensities, resulting in low reaction yields. In particular, the windows on gas cells are likely to stop the low-energy (around 500 keV) decay α -particles, removing the possibility of measuring α branching ratios.

used to probe the $^{27}\text{Al}(p,p')^{27}\text{Al}^*(p/\alpha)^{26}\text{Mg}/^{23}\text{Na}$ reactions for states in ^{27}Al above the neutron threshold to probe the stellar nucleosynthesis of ^{26}Al . The α_0 and p_0 branching ratios for one of the states observed in this measurement are already known, these can serve as tests of the accuracy of the approach.

The experimental apparatus, while different from the previously discussed experiments is similar enough that it is sufficient to confine the account to those matters where differences exist. The data analysis performed to date will be discussed along with some preliminary results to demonstrate that the system is functioning correctly. Discussion of the astrophysical implications of the experiment will be limited as it falls outside the scope of this thesis. The potential applications of this setup for the determination of the B_α in ^{19}Ne are then set out.

9.2 Astrophysical Background

Before discussing the experimental setup used for the Orsay experiment, a brief outline of the astrophysical background to the experiment is beneficial. ^{26}Al is a nucleus of great astrophysical importance. It has a long lifetime ($t_{1/2} \approx 7.17 \times 10^5$) due to the high spin of the ground state (5^+) which inhibits the decay to the lower spin low-lying states in ^{26}Mg . The decay to the 2_1^+ state produces a 1.807-keV γ ray which can be observed by γ -ray telescopes (see Ref. [92] and references therein) which provided the first evidence of continuing nucleosynthesis in the galaxy. In addition, ^{26}Al is thought to be responsible for the high $^{26}\text{Mg}/^{24}\text{Mg}$ ratio in certain Ca-Al-rich meteoritic grains. In this case, the ^{26}Al included at the formation of the grain decays into ^{26}Mg , increasing the $^{26}\text{Mg}/^{24}\text{Mg}$ ratio.

There are a number of potential production sites for ^{26}Al : supernovae, asymptotic giant branch (AGB) stars (red giant stars with significant mass loss), Wolf-Rayet stars (massive stars with strong and fast stellar winds and significant mass loss) and novae. A number of reactions contribute to the final ^{26}Al abundance. Supernovae are thought to contribute a relatively small amount of final ^{26}Al production [93]. In AGB stars and Wolf-Rayet stars, there are a number of reactions the uncertainty in which contributes to the total uncertainty in the the neutron-induced reactions $^{26}\text{Al}(n,p)^{26}\text{Mg}$ and $^{26}\text{Al}(n,\alpha)^{23}\text{Na}$ are thought to play an important role in the destruction of ^{26}Al ; the neutrons are produced by the neutron source reactions $^{13}\text{C}(\alpha,n)^{16}\text{O}$ and $^{22}\text{Ne}(\alpha,n)^{25}\text{Mg}$.

The neutron-threshold in ^{27}Al lies at a high excitation energy (≈ 13 MeV) which might lead to the expectation that statistical models would reproduce the reaction rate well. However, the high spin of the ^{26}Al ground state means that only high-spin resonances in ^{27}Al can be populated in s - and p -wave reactions. These resonances will dominate the astrophysical reaction rate due to the lower penetrability. Direct measurements of the cross section are inhibited by the dual requirements that a radioactive ^{26}Al target is constructed and that the beam required for the experiment consists of neutrons, for which the incident

energy is difficult to determine. Indirect measurements are desirable in order to constrain resonance parameters (such as branching ratios) and to support direct measurements.

Proton-decays from above the neutron-threshold are dominated by the p_1 reaction channel (to the first excited state of ^{26}Mg) due to the lower spin in the exit channel. Knowledge of the relative proton branches to excited states in ^{26}Mg allows for corrections to be made to inverse measurements using the $^{26}\text{Mg}(p,n)^{26}\text{Al}$ reaction which is only sensitive to the p_0 channel. In addition, ^{26}Al destruction is more efficient in the $^{26}\text{Al}(n,p)^{26}\text{Mg}$ reaction than in the $^{26}\text{Al}(n,\alpha)^{23}\text{Na}$ [94]. Therefore, knowledge of the relative proton and α -particle branching ratios will help to account for contributions to weakly populated channels or channels which cannot be observed with a particular experimental setup.

9.3 Experimental outline and apparatus

The principles underlying magnetic spectrometers have been set out previously in section 7.4.1. The Orsay Enge spectrometer and the Munich Q3D have some differences, however. These are summarised below in two sections: the optical differences and the different focal plane setups.

The Orsay facility also uses a tandem accelerator as described in section 7.3. In this case a 18-MeV proton beam of between 10 and 100 pA was incident upon a ^{27}Al target, causing inelastic scattering of the protons. The Enge magnetic spectrometer was placed at 40° and the magnetic field set so that scattered protons corresponding to excitation energies in ^{27}Al around the neutron-threshold (13.058 MeV) were then incident on the focal plane. Charged-particle (proton and α) decays of these ^{27}Al states were then detected by the silicon detectors placed within the reaction chamber; details of the silicon detector setup are given in section 9.3.3. Figure 9.1 shows the states in ^{26}Mg and ^{23}Na which can be populated in the decay of the neutron-unbound states in ^{27}Al , along with the relative positions of the neutron-, proton- and α -thresholds.

The Faraday cup in the reaction chamber that measures the integrated beam on target is made from graphite. Excitations of the carbon atoms to the 2_1^+ state in ^{12}C by the beam result in 4.4-MeV γ rays which can scatter from the silicon detectors causing background counts. In addition, activation of the Faraday cup is possible which results in decay β particles which can also produce background counts. In order to reduce these sources of background, a shield is placed across the centre of the reaction chamber, as shown in fig. 9.2.

9.3.1 The Orsay Enge magnetic spectrometer

Enge magnetic spectrometers were designed to be able to compensate for the kinematic broadening of states due to finite aperture size and to increase the effective aperture size to increase the acceptance of the spectrometer. The two main innovations of the Enge

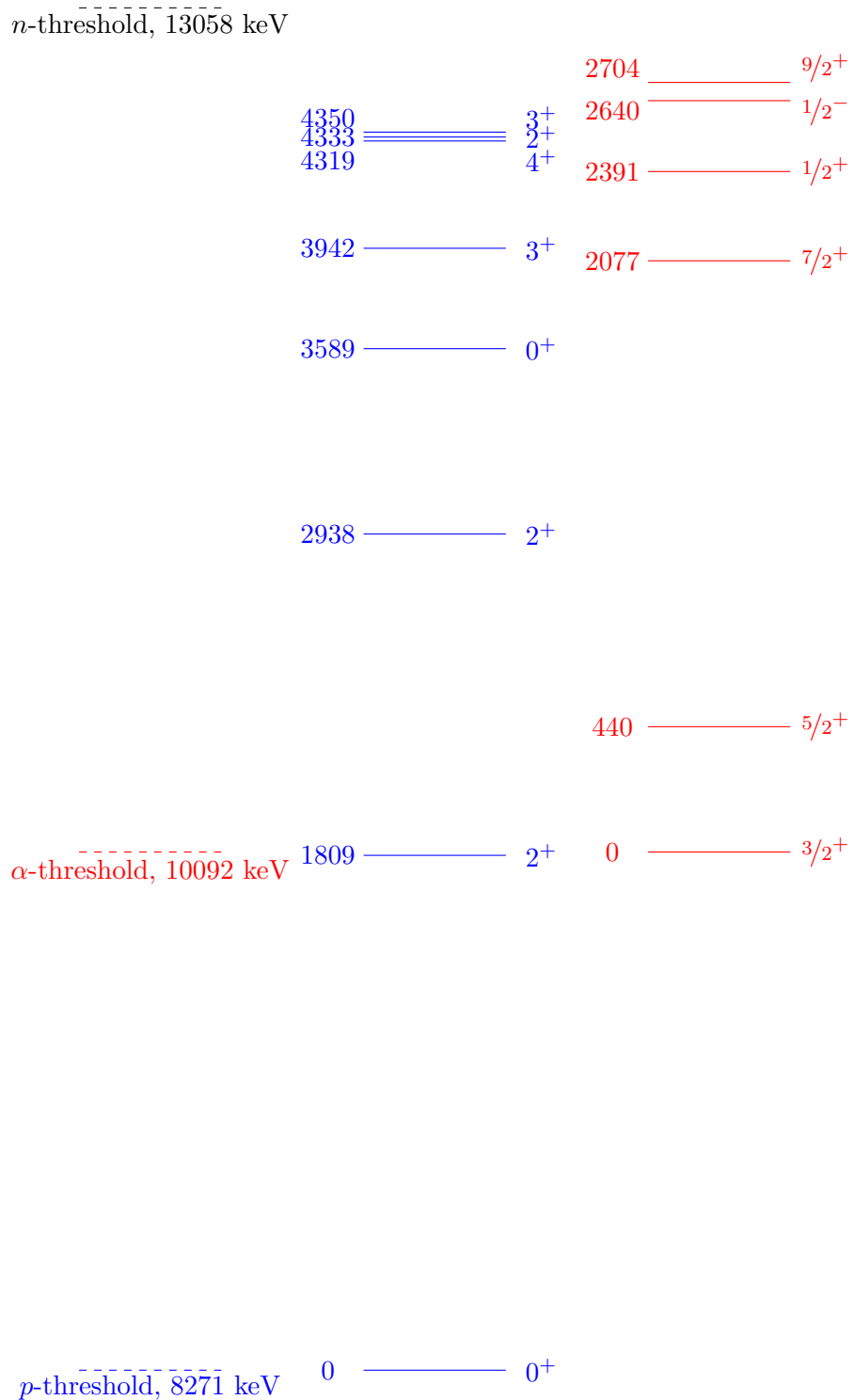


Figure 9.1: Diagram showing the relevant energy levels for the $^{26}\text{Al}(n,p)^{26}\text{Mg}$ and $^{26}\text{Al}(n,\alpha)^{23}\text{Na}$ reactions. All energies are given in keV. States marked in blue are those relating to $^{26}\text{Mg}+p$ and those in red are related to $^{23}\text{Na}+\alpha$. The ground state of ^{27}Al is $5/2^+$.

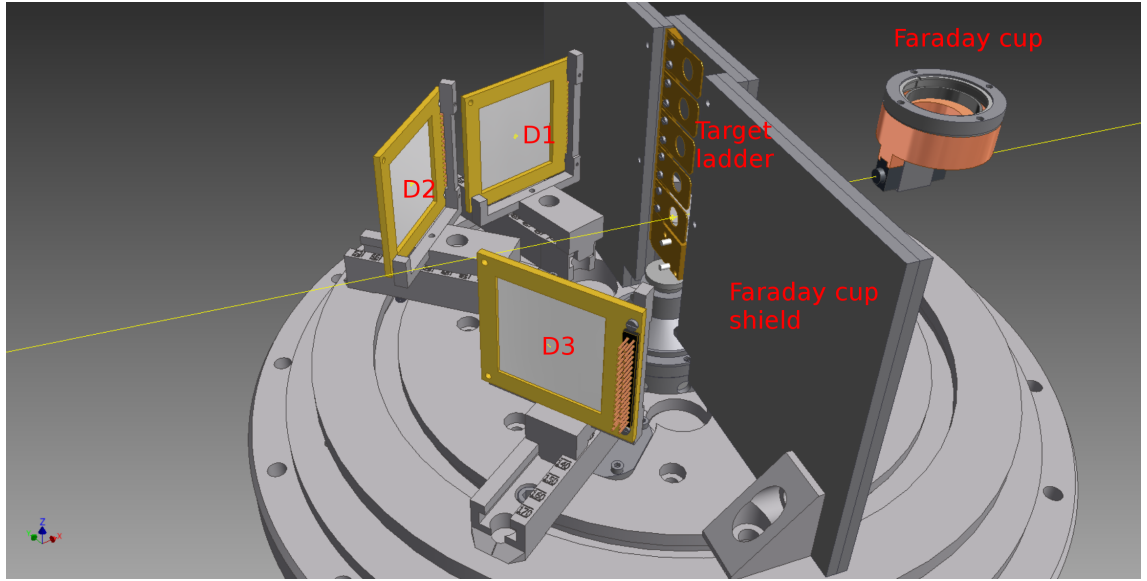


Figure 9.2: Experimental setup showing the silicon detector placement within the reaction chamber, the beam, the target ladder, the Faraday cup shield and the Faraday cup itself [95]. The spectrometer was placed at 40° to the left of the beam.

‘splitpole’ magnetic spectrometer are the splitting of the magnetic pole into two separate sections (hence the name) and the shaping of the poles [96]. Splitting the pole causes fringe fields from the edge of each pole which focus reaction products in the vertical direction increasing the acceptance of the spectrometer. This serves the same purpose as the quadrupole at the entrance to the Munich Q3D.

The shaping of the poles causes focussing in the plane of the spectrometer correcting for the kinematic broadening. Reaction products then enter the spectrometer with slightly different angles relative to the field, which causes transverse focussing. Different reaction products with different kinematics will come into focus at different focal plane depths. In order to optimise the experimental resolution, the focal plane detectors are mounted on an extendible arm which can be moved to the correct position.

The Orsay Enge spectrometer does not use a feedback loop to hold the magnetic field at a fixed strength as the Munich Q3D detector does; this can lead to slow and small variations (usually in the range of $\delta B/B \approx 10^{-4} - 10^{-5}$) in the strength of the field. In order to compensate for this effect, the field strength is instead recorded by a NMR probe and logged. During the analysis of the data, the Enge spectrometer spectrum can be corrected for the shifts in the field. This process is described in the data analysis section.

9.3.2 Focal plane detectors

There are three detectors at the focal plane of the Orsay spectrometer, two proportional gas counters, the first of which is used for determination of the focal plane position as

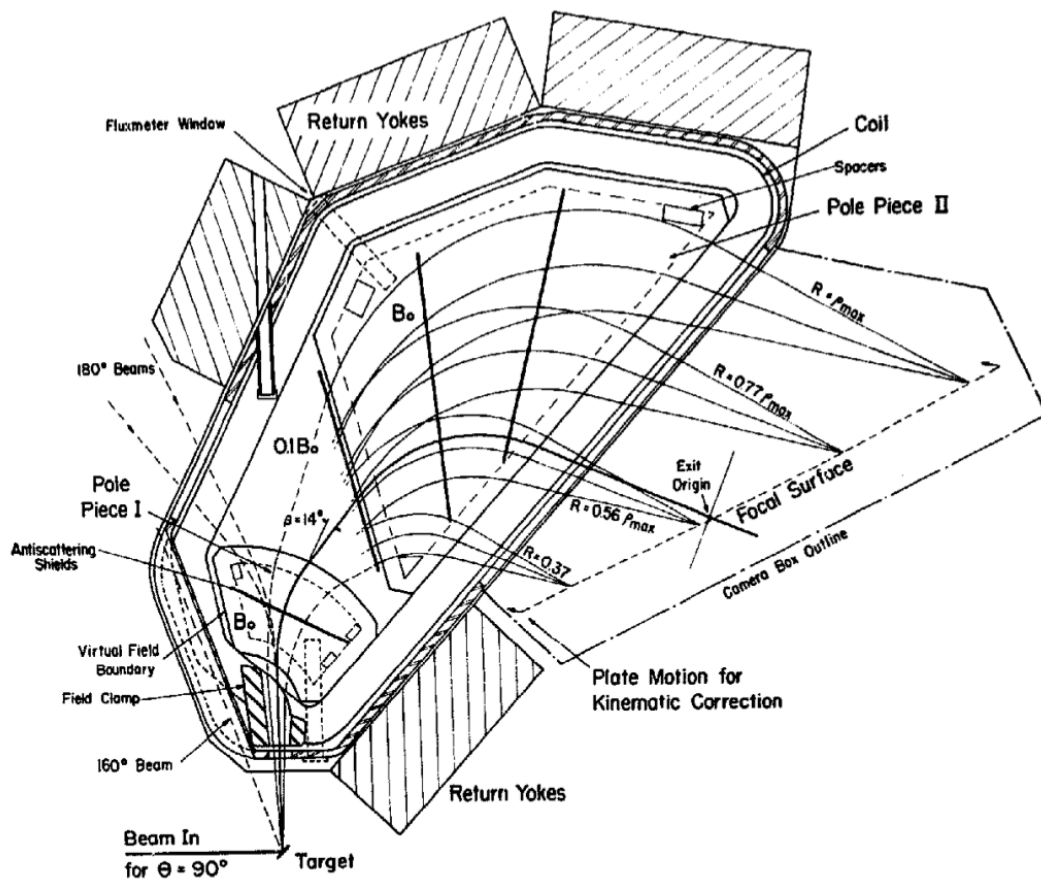


Figure 9.3: A schematic of an Enge spectrometer [97]. The shaping of the first pole piece and the gap between the poles are both clearly visible.

described below, and a plastic scintillator. In the same way as in the Munich Q3D, particle identification is achieved by considering energy loss through the proportional counters. In the case of the Orsay spectrometer, the focal plane position and the energy loss in the second proportional counter are usually sufficient (as in this case) to identify light ions from reactions; for heavier ions, further cuts may result in cleaner spectra [98].

The first proportional counter has five wires running lengthways down the focal plane. These wires form the anode and are used to record the energy lost through the proportional counter. In addition, there are a series of cathode strips which run into the focal plane at an angle of 40° to the normal, the angle at which reaction products reach the focal plane. The cathode strips are read out through a delay line. The two ends of the delay line are read out as separate signals, with one end of the delay line being used to start a TDC, and the other end being used to stop the TDC. The size of the pulse generated by the TDC gives the focal plane position [98].

9.3.3 Silicon detectors

The principles behind silicon detectors have been laid out previously in this thesis in section 4.3. In this case, three W-type detectors were used. These are double-sided strip detectors with 16 3.1-mm wide (3-mm wide active area and 0.1-mm wide interstrip region) strips per side. One 1-mm thick detector (denoted as detector 1, D1 in fig. 9.2) was used along with two 300- μm thick detectors (denoted as detectors 2 and 3, D2/D3 in fig. 9.2). These detectors were placed in the reaction chamber as shown in fig. 9.2. The detectors cover 4.9% of the solid angle in the laboratory frame (0.616 sr); the experimental efficiency is slightly lower as the decay products are forward focussed in the lab frame, this is discussed in section 9.4.2. The lab frame angular coverage is shown in fig. 9.4.

9.3.4 Data acquisition

The plastic focal plane detector was used as the trigger for this experiment. Data were subsequently recorded using a MIDAS (UK) data acquisition system transported to Orsay.

Signals are recorded using analogue-to-digital converters (ADCs - SILENA-9418 modules were used during this experiment) and time-to-digital converters (TDCs - CAEN V1190 modules in this experiment). ADCs evaluate the size of the incoming signal, convert this size to a number and provide this number to the DAQ computer for storage. The TDCs read out a value which is related to the time between the start and stop signals. The CAEN V1190 modules can be used in a multi-hit mode (able to deal with more than one hit per channel in the same event). During the experiment, problems were discovered when this mode was used. Therefore, the single-hit mode was used.

The data acquisition was controlled by a SILENA-9418 Acquisition Control module (SAC). The trigger from the plastic focal plane detector (described below) was fed into

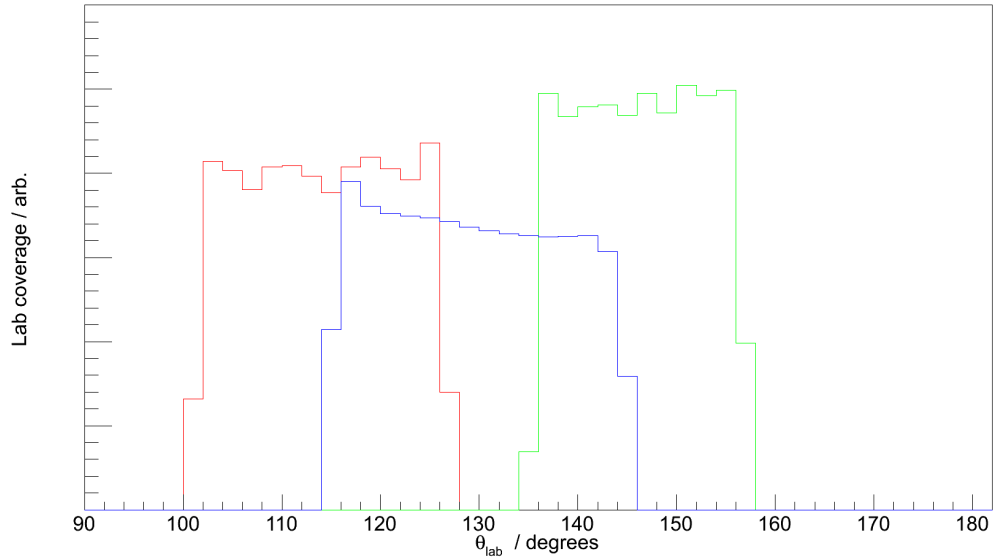


Figure 9.4: Orsay laboratory angle coverage, in arbitrary units. The red curve is detector 1, the green is detector 2 and the blue is detector 3.

the SAC and the trigger signal from the SAC was then passed to the ADCs. If the ADCs accepted the event, the ‘Monitor 2’ output from the SAC, which was fed into the TDCs, acted as the TDC trigger. Using this ‘Monitor 2’ signal meant that only events which have been accepted by the ADCs trigger the TDCs.

The TDCs have a 40-MHz clock which results in a clock cycle of 25 ns. This results in a 25-ns clock ‘jitter’ depending on when in the clock cycle the triggering signal reached the module. Two TDC values in the same event should both have the same jitter from the trigger - TDC differences will then result in the trigger jitter being cancelled.

Due to the use of the plastic focal plane detector as the trigger, signals from the silicon detectors in the chamber had to be delayed to account for the longer time-of-flight of protons through the spectrometer compared to protons or α -particles within the target chamber. This was achieved using the SAC, which allows for an offset and width, the sum of which cannot exceed 40 clock cycles ($1 \mu\text{s}$). This enables the acquisition system to accept a trigger from the plastic focal plane detector within $1 \mu\text{s}$ after a hit in a silicon detector. The flight path through the spectrometer for a proton is of the order of a few metres (depending on the energy of the proton and thus its path through the spectrometer). A proton scattered at 40° at an excitation energy in ^{27}Al of 14 MeV has a velocity of around 8% of the speed of light. In $1 \mu\text{s}$, this corresponds to around 24 m, far longer than any flightpath in the spectrometer.

The various signals from the focal plane detectors (plastic, both proportional counter energy deposited signals and the position signal as described above) were dealt with dif-

ferently. The signals from the plastic scintillator were fed into a timing filter amplifier (TFA) and the output from this was split in a linear fan-in fan-out module. One output was fed into a discriminator, the output from this discriminator was used to trigger the DAQ via the SAC. This discriminator output signal was also fed into a TDC channel for the purpose of the jitter removal described above. The other output is fed into an ADC channel.

For both of the proportional counters, the signals are fed into TFAs and then into the ADC modules for the signal sizes to be recorded. One of the proportional counter anode discriminator output signals was also fed into the TDC modules as a stop signal and recorded. In addition, the signal from the position determination, as described previously, was fed into an ADC channel to be recorded.

Silicon detector signals were initially fed into Mesytec MPR-16 preamplifiers via 16-way ribbon cables. The outputs from these preamplifiers were fed into Mesytec STM-16+ shaping amplifiers. The output of these amplifiers was fed into 32-channel SILENA-9418 ADCs which record the events, converting them into a digital format and providing this datum to the central acquisition model for recording. The shaping amplifiers also output a signal based on a leading-edge discriminator which is used as a stop signal for the TDCs.

9.4 Data Analysis

The data analysis applicable to this thesis is limited to that which confirms that the system is working correctly and confirms the applicability of the system to the study of branching ratios of α -unbound states in ^{19}Ne while recommending changes in the proposed future experiment. The software routines for processing these data have been constructed by the author.

First of all, the spectrometer data must be processed. This requires gating on the differential energy loss to identify particles at the focal plane followed by correcting the raw $B\rho$ value calculated for shifts in the magnetic field between runs. After this, various conditions must be placed on the data from the silicon detectors: the energies recorded in the front and back strips of the detector must be approximately the same, there must be an ADC value and a TDC value recorded in the same silicon front channel and the silicon event must occur within a certain range of differences in TDC value between the silicon event and a proportional counter event.

9.4.1 Focal plane singles spectrum

The focal plane spectrum is produced in a similar manner to that for the Munich Q3D. In this case, the focal plane position (as a proxy for energy) and the energy loss through the

proportional counter are used to identify protons.² Once this has been done, correction must be made for the shift in the field mentioned above. The ρ corresponding to each focal plane position can be found by calibrating using a target with well-known energy levels, in this case the ground state and the 4.4-MeV state in ^{12}C [95]. Once this is done, the $B\rho$ for each event is found by multiplying the calculated ρ by the average field for the run, as recorded by the field monitor. The focal plane singles spectrum is shown in fig. 9.5. Figure 9.5a shows the full spectrum, fig. 9.5b shows the same spectrum (without a background subtraction) just over the astrophysically-relevant region.

9.4.2 Spectrometer-silicon coincidence spectra

The silicon detectors were calibrated for energy using a 3α source. In order to look for coincidences, a number of conditions are placed on the data to reduce the random background from β s and γ s from the Faraday cup. These conditions are: that there are two silicon signals, one in the front and one in the back of the same detector, with approximately the same energy. In addition, a timing value for the event must have been recorded in the same front strip as the ADC value and the silicon-wire δTDC must fall in the peak shown in fig. 9.6.

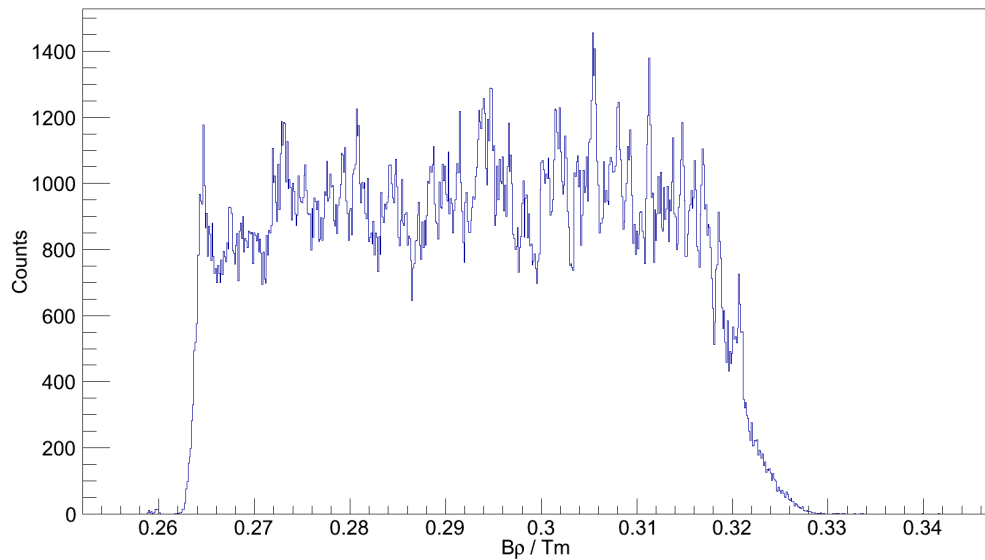
Using these gating conditions above, a $B\rho$ against silicon energy plot can be produced (fig. 9.7a). Figure 9.7b shows the same plot with the p_0 , p_1 and α_0 loci marked and only includes events from detector 3 as the background in this detector is lower than in detector 1 and the kinematic variation of the light ions is smaller than that in detector 2 which makes the kinematic loci clearer.

The focal plane spectra which result from gates being placed on the kinematic loci visible in fig. 9.7 are shown in fig. 9.8. The neutron separation energy is also marked. Below the neutron separation energy ($S_n = 13.057$ MeV), there are a series of clear peaks in the focal plane spectrum. These are most readily apparent in the p_1 spectrum. These are caused by the charged-particles from the decay of proton- and α -particle-unbound but neutron-bound states.

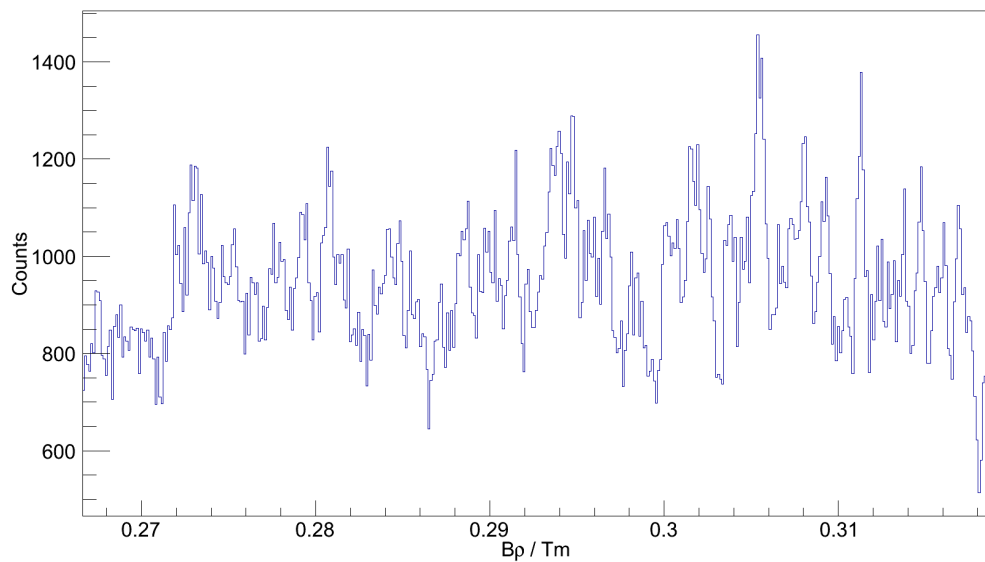
Efficiency

A short simulation code has been written to calculate the efficiency of the array. This code makes the simplistic assumption that the energy of the recoiling ^{27}Al nucleus is 340 keV and that it is emitted at 24° , the final efficiency does not change strongly when different energies and angles are considered as the the ranges of recoil energies and angles are small. Mathematical details on the calculations are given in appendix B. Emission is assumed to be isotropic in the centre-of-mass frame. The system is then transformed to the laboratory

²The cut on differential energy loss is still used but has very little effect in this case as it appears that only protons are reaching the focal plane.



(a) Intensity plot against $B\rho$ for the active region of the focal plane. The background in the Enge spectrometer is obviously high. In addition, as the edge of the plastic scintillator is reached, the number of events recorded drops away as the DAQ is no longer being triggered. Note that the drop is gradual as there is a range of proton trajectories at the focal plane (which is at the centre of the position proportional counter) meaning that some protons miss the plastic scintillator. The field was chosen such that the astrophysically-relevant region is still covered.



(b) Plots of $B\rho$ from the Orsay Enge spectrometer. This plot is the same as that in fig. 9.5a but excludes the edges of the focal plane. The range of the ordinate is limited in order to allow details of the spectrum to be observed.

Figure 9.5: Plots of $B\rho$ from the Orsay Enge spectrometer.

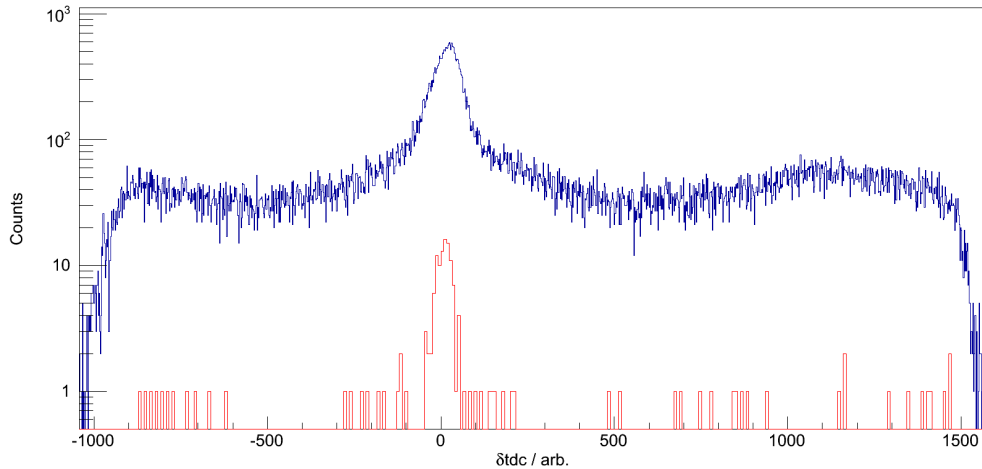


Figure 9.6: δ TDC for focal plane plus silicon coincidence events from detector 3. The blue spectrum is the δ TDC for all events whilst the red spectrum is gated on the p_0 kinematic locus which is discussed below and shown in fig. 9.7b. Each bin is 0.8-ns wide.

frame. Whether this particle hits one of the detectors is then determined along with the position on the detector where the hit took place. The proportion of the total number of events which hit the silicon detectors in a functioning strip is then taken to be the total efficiency of the system. This efficiency is found to be 3.4% for p_0 protons originating from an excitation energy of 13.5 MeV. For α -particles under the same conditions, the efficiency is 3.0%.

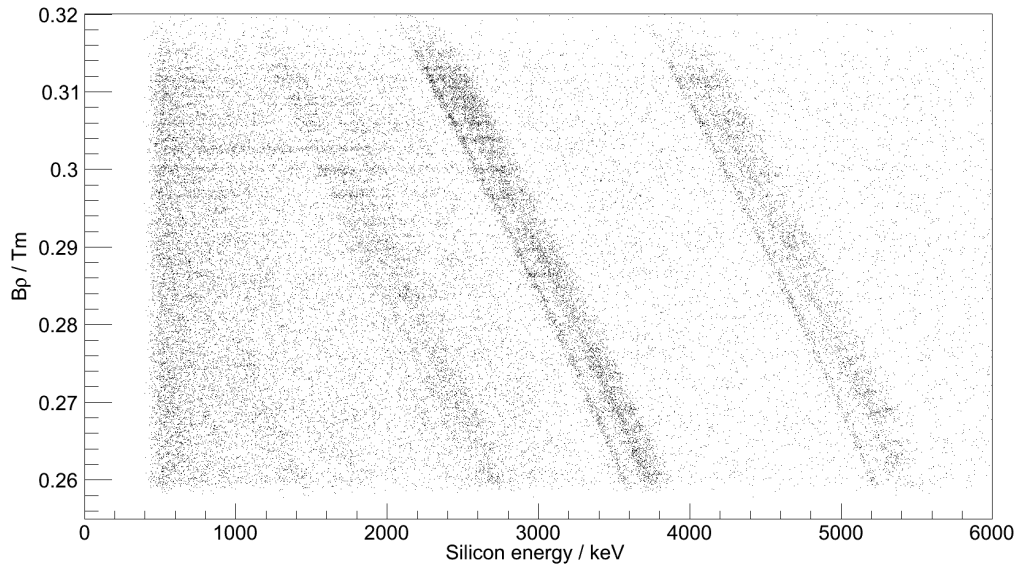
9.4.3 Preliminary results

Preliminary results are now presented from this analysis. Full efficiency calculations are yet to be performed taking into account the hit conditions in the silicon detectors. In addition, the high background in the singles focal plane spectrum makes extraction of absolute branching ratios extremely difficult. For this thesis, therefore, consideration is confined to relative branching ratios between the various channels.

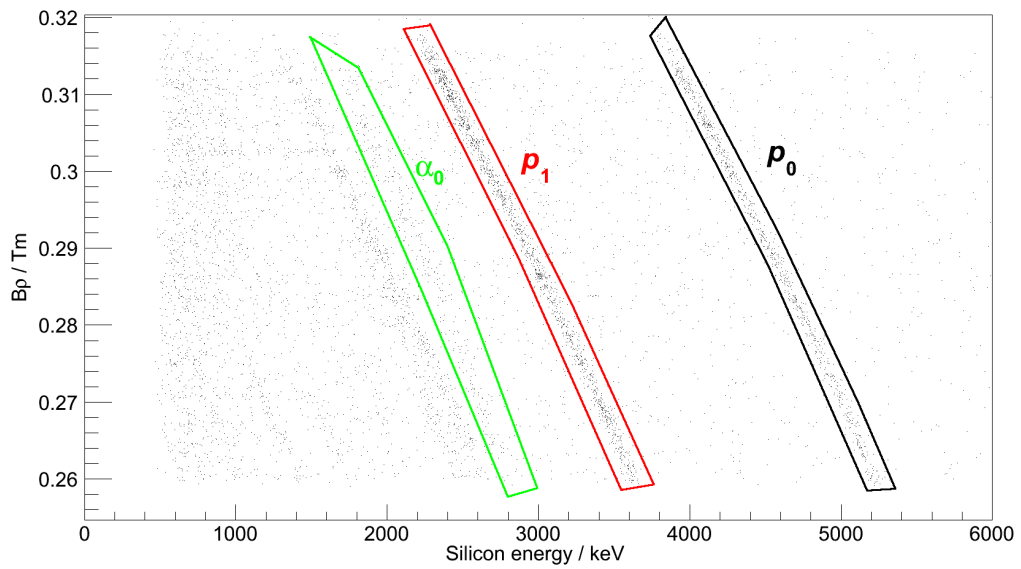
In order to extract relative branching ratios, the yields from each resonance must be extracted. This is done by assuming that all resonances are described by Gaussians of a common width, σ , which is required to be positive. The centroids (μ_i) and peak heights (A_i) are left free (with the condition that the peak height must not be negative). This, combined with a background function $b(B\rho)$ leads to a function of the form:

$$f(B\rho) = \sum_i A_i e^{-\frac{(B\rho - \mu_i)^2}{2\sigma^2}} + b(B\rho). \quad (9.1)$$

When the coincidence focal plane spectra is fitted, the background is low enough that



(a) Silicon energy against $B\rho$ for coincidence events for all silicon detectors. The p_0 , p_1 loci are clearly visible and separated from other charged particle loci. The α_0 and p_2 loci overlap somewhat which makes separation in this plot difficult.



(b) Silicon energy against $B\rho$ for coincidence events for detector 3. The p_0 , p_1 and α_0 loci are all marked on the spectrum.

Figure 9.7: Silicon energy against $B\rho$ for coincidence events for detector 3.

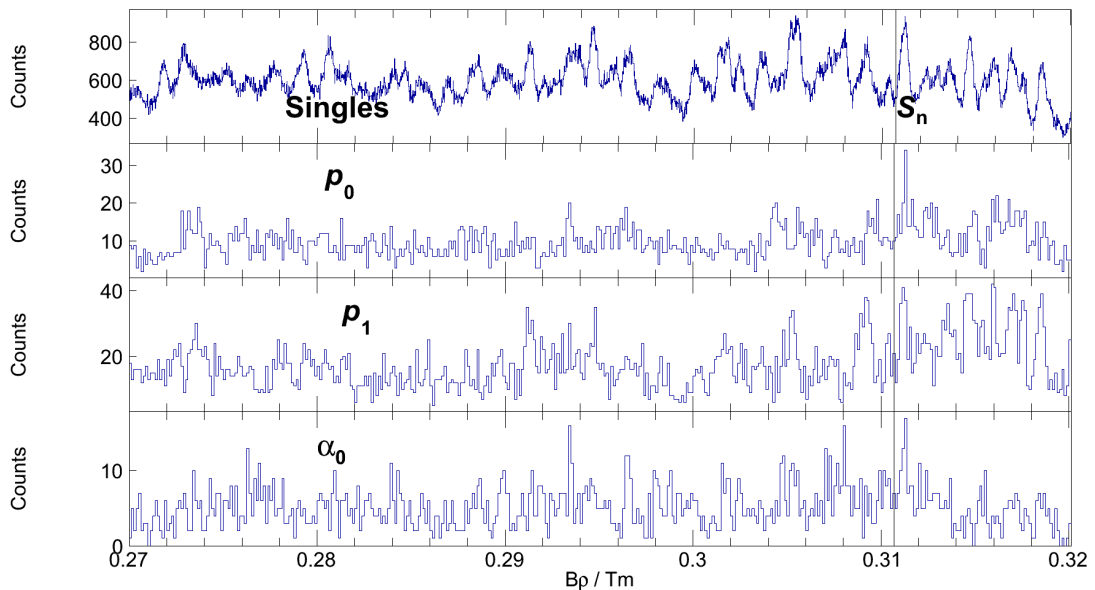


Figure 9.8: Focal plane spectra for gates on the kinematic loci in fig. 9.7. The top plot shows the singles focal plane spectrum, the lower two plots show the focal plane spectra gated on the p_0 , p_1 and α_0 loci. There are a series of clear peaks below the neutron threshold which are caused by proton and α -particle decays of excited but neutron-bound states.

it may be omitted.

The focal plane singles spectrum is fitted in order to extract centroid positions. These centroid positions are then used in the fit function for the p_0 and p_1 spectra. The fit parameters for the various peaks are given in table 9.1.

These results are preliminary and further analysis may result in different yields extracted for different states. In particular, no correction is made for different efficiencies due to angular distributions of products in the outgoing channel which may effect the final branching ratios, hence no corrected yield for each state is given. It should be noted that the analysis in this case bears very little relation to the analysis which will be required for the case discussed in the next section as, in this case, the level density is high and the states are overlapping whilst, in the other case, the level density is low and the states can be separated using the spectrometer and the silicon spectra projected out on the basis of a specific state being selected.

9.5 Summary and applicability to $^{19}\text{F}(^3\text{He},t)^{19}\text{Ne}^*(\alpha)^{15}\text{O}$

While further analysis is required to extract proton and α branching ratios of these states in ^{27}Al , the coincidence plot in fig. 9.7 shows clear kinematic loci for proton and α -particle decays from unbound states in ^{27}Al . In addition, fig. 9.8 shows clear peaks in the p_1 -gated

Peak number	Rigidity / Tm	Peak height (singles)	Peak height (p_0)	Peak height (p_1)
1	0.29579(0.00001)	662.9(35.9)	9.9(1.9)	14.8(2.3)
2	0.29493(0.00004)	570.1(43.2)	9.7(2.7)	9.2(2.6)
3	0.29668(0.00001)	892.5(36.5)	12.2(2.0)	15.3(2.3)
4	0.29751(0.00002)	241.9(31.6)	4.9(1.7)	12.2(2.2)
5	0.29872(0.00004)	306.4(33.3)	1.5(1.9)	3.7(2.2)
6	0.29820(0.00003)	422.3(37.0)	8.3(2.1)	10.0(2.4)
7	0.29921(0.00004)	211.0(36.5)	9.1(2.0)	6.7(1.8)
8	0.30018(0.00001)	789.0(34.7)	6.5(1.6)	9.2(1.9)
9	0.30089(0.00002)	515.6(31.4)	5.3(1.5)	11.9(2.2)
10	0.30171(0.00001)	1089.6(34.3)	9.6(1.8)	18.1(2.5)
11	0.30258(0.00001)	834.7(35.6)	7.0(1.5)	16.6(2.3)
12	0.30374(0.00001)	954.5(35.4)	8.2(1.7)	13.3(2.1)
13	0.30457(0.00001)	691.7(32.7)	16.1(2.4)	13.8(2.4)
14	0.30535(0.00002)	1188.3(76.4)	2.8(1.8)	19.0(3.1)
15	0.30580(0.00003)	687.8(73.4)	8.5(2.1)	10.1(2.6)
16	0.30665(0.00002)	704.6(30.6)	12.2(2.2)	9.6(2.0)
17	0.30807(0.00001)	1219.8(32.8)	8.2(1.9)	8.4(2.1)
18	0.30887(0.00005)	436.2(74.3)	2.2(1.7)	15.2(3.4)
19	0.30929(0.00003)	863.1(65.8)	6.3(2.8)	20.2(4.1)
20	0.30980(0.00006)	310.7(46.8)	12.0(2.8)	2.7(2.4)
21	0.31043(0.00001)	675.6(35.9)	9.0(1.9)	12.3(2.2)
22	0.31132(0.00000)	1440.1(34.5)	13.8(1.7)	27.4(2.8)
23	0.31232(0.00001)	865.6(33.4)	13.5(2.0)	25.3(2.9)
24	0.31305(0.00001)	796.8(32.0)	10.8(1.6)	15.1(2.7)
25	0.31379(0.00001)	1012.5(34.4)	5.3(1.4)	22.1(2.8)
26	0.31478(0.00001)	1324.7(38.2)	11.8(1.9)	30.0(18.1)
27	0.30735(0.00001)	857.1(29.9)	6.7(1.9)	15.9(2.5)

Table 9.1: Table of peak position and height information for the singles spectrum and the p_0 and p_1 spectra. All fits use a common width of 0.000298 Tm. The α_0 spectrum is omitted due to problems separating the kinematic loci for one of the detectors. Work to use the time-of-flight of particles to separate the different species is still on-going. Errors quoted are the uncertainty of the fit and do not include any statistical errors.

focal-plane spectrum. This confirms that the system is functioning correctly. A complete analysis of the data is being carried out in preparation for publication but falls outside the scope of this thesis project. For the purpose of this thesis, the applicability of the setup to the measurement of B_α for states in ^{19}Ne through the $^{19}\text{F}(^3\text{He},t)^{19}\text{Ne}^*(\alpha)^{15}\text{O}$ is of interest.

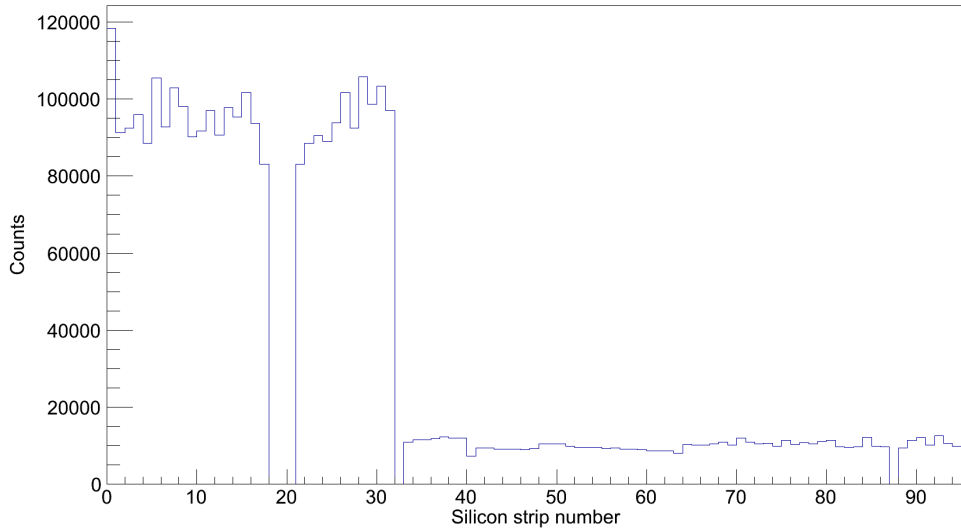
At this point, comparison of this experiment to previous studies should be made. Of the previous studies, only two are capable of separating the doublet [53, 54] - both of these studies use the spectrometer plus silicon setup proposed for this study, and another study claims measurements of the α -particle branching ratio for the 4033-keV state. Ref. [54] suffers from problems with the threshold in the electronics and so normalisation for this experiment is difficult. Ref. [53] used silicon surface barrier detectors, not silicon strip detectors. Silicon strip detectors allow for a better background suppression as front-back coincidences can be required, along with a valid timing event. In addition, no attempt was made in the analysis of Ref. [53] to investigate the α -particle branching ratios of the doublet states. Given these factors, repeating the experiment with a similar experimental setup with a more effective silicon array may allow for a more sensitive result.

A previous study (Tan *et al.* [58]) has claimed measurements of the branching ratios of the astrophysically relevant states. However, in that experiment there are a number of factors that could be improved upon. First of all, the 4140/4197-keV doublet is not resolved; in chapter 3, the argument was made that the identity of the doublet as α -cluster states means that future experiments to measure the branching ratios of these states should endeavour, if possible, to ensure that these states are resolved. Secondly, the background in their data is quite high, which increases the uncertainty in the final result.

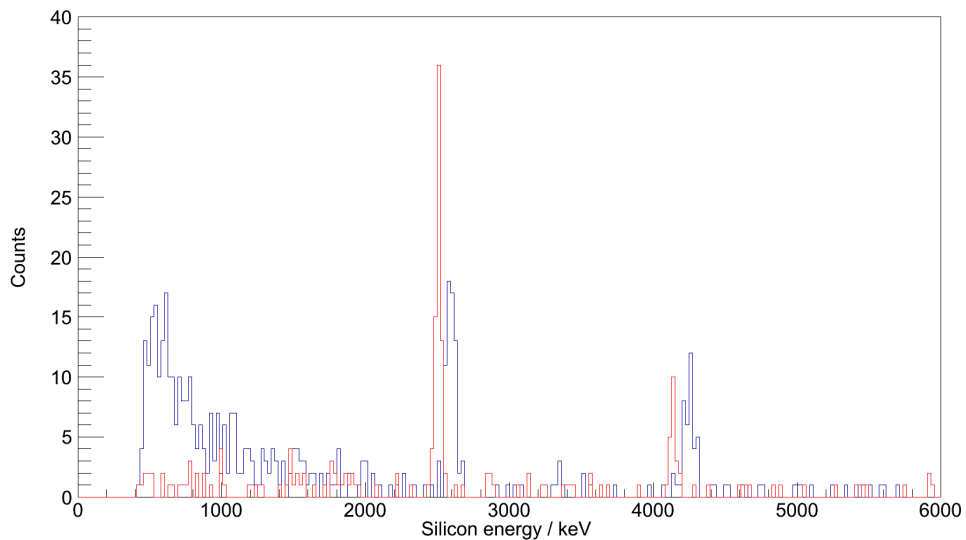
The magnetic spectrometer plus silicon system obviates the first of these issues; the superior energy resolution enables separation of these states.

In Ref. [58], the experiment is performed with six 300- μm thick pad silicon detectors in the target chamber, each of which is split into four pads and covers $4 \times 4 \text{ cm}^2$. The coarse segmentation of these detectors increases the likelihood of background counts compared to a finely segmented double-sided silicon strip detector upon which front-back energy requirements are placed. In addition, thinner silicon detectors have a much lower background due to β -particles or γ rays from the Faraday cup. This is clearly visible in fig. 9.9a; the ADC channels 0 to 31 correspond to the 1-mm thick silicon detector while the higher channels correspond to the 300- μm thick silicon detectors. Figure 9.9b shows the silicon energy spectra for detectors 1 (1-mm thick) and 3 (300- μm thick), again demonstrating the large reduction in background as the thickness of the detector is reduced. The α -particles of interest in this experiment range from around 500 keV to 1000 keV corresponding to ranges of a few μm in silicon [99]; thin silicon detectors should therefore be used to reduce the background from background counts.

However, there is a major penalty to using the spectrometer plus silicon system. The



(a) Silicon ADC hit pattern for the Orsay experiment with a focal plane plastic detector trigger. The channel ordering is 0-15 (all numbers inclusive) is detector 1 (1-mm thick) front, 16-31 detector 1 back, 32-47 and 48-63 are detector 2 (300- μm thick) front and back, 64-71 and 72-95 are detector 3 (300- μm thick) front and back. Channels 18 to 20 and 87 are noisy strips and are removed from the analysis, channel 31 is defective. The background in the 1-mm detector is around 95000 counts per channel. In the 300- μm detectors, the background is 10000 counts per channel. This is a reduction in background of 90% for a reduction of detector thickness of 70%.



(b) Silicon spectra for detectors 1 (blue) and 3 (red) gated on $B\rho$ between 0.3032 Tm and 0.3043 Tm; the choice of rigidity is for illustrative purposes only. The background in the thicker detector 1 is much higher than that for the thinner detector 3. The shifts in energy of the peaks is due to kinematic differences from the differing placement of the detectors.

Figure 9.9: Spectra showing the effect that silicon detector thickness has on the experimental background.

first and most pressing concern is the reduction in the statistics available. The solid angle acceptance of the TwinSol system [100] used in Ref. [58] is 50 msr compared to only 1.4 msr for the Orsay magnetic spectrometer. Other spectrometers have larger acceptances due to a quadrupole at the entrance to the spectrometer; for example, the acceptance of the Munich Q3D can reach up to 13.9 msr if the slits at the entrance to the spectrometer are fully open. This may suggest that the use of another magnetic spectrometer with a larger acceptance is preferable to use of the Orsay spectrometer.

In addition to this, the thresholds on the silicon detectors must be set very low in order to detect the α particles emitted, which can have energies of only 200 keV (depending on the angle of emission). In the current experiment, thresholds were set at around 500 keV. From fig. 9.9b, it is clear that the background in this energy region in the 300- μm thick silicon strip detectors is very low, which allows for a more robust extraction of the signal from the noise.³

Tan *et al.* do not state the beam intensity used during the experiment but do state that the $({}^3\text{He},d)$ cross section is much higher than the $({}^3\text{He},t)$ cross section and that deuterons produced in these reactions hit the silicon detectors used to detect reaction tritons [58]. This may limit the maximum beam current to their apparatus. Previous studies of $({}^3\text{He},t)$ reactions using magnetic spectrometers have used beam currents in the region of 500-600 nA without high deadtimes or problems on the focal plane due to deuterons [102].

The ${}^{19}\text{F}({}^3\text{He},t){}^{19}\text{Ne}$ reaction has been previously studied at the Munich Q3D [103]. In this experiment, the differential cross section for the 6014-keV state in ${}^{19}\text{Ne}$ was found to be around 100 $\mu\text{b}/\text{sr}$ at 30° . Comparing the yield to this state in Ref. [58] to those of the 4033-, 4140 and 4197-keV states suggests that the cross section for the 4033-keV state is around a factor of 5 lower, while those the 4140/4197-keV states suggest around a factor of 10 lower. Assuming a beam current of 100 pA running for five days continuously and a target thickness of 30 $\mu\text{g}/\text{cm}^2$, gives a total experimental yield of around 3500000 counts for the 4033-keV state and 1750000 counts for the 4140- and 4140-keV states. In order to corroborate the results regarding the doublet from Ref. [58], the experiment must be sensitive to branching ratios of around 10^{-3} . With an efficiency of 5% and a branching ratio of 10^{-3} , the total triton plus α yield is 80 counts per state. This may increase by an order of magnitude if a magnetic spectrometer with a higher acceptance is used, such as the Munich Q3D. This is promising as it suggests that a measurement of the B_α for the doublet is possible with the current system. For the 4033-keV state, the branching ratio is thought to be of the order of 10^{-4} , this suggests a total of around 16 counts at 100 pA. If the background in the coincidence spectrum is low, then this should also be measurable.

Additional improvements that should be considered include the use of a 0° spectrom-

³In past experiments of a similar style, including that of Ref. [53] using the Yale Enge spectrometer, the backgrounds observed using $({}^3\text{He},t)$ reactions were lower than those observed in (p,p') reactions, which further strengthens the case that the low-energy background can be successfully suppressed [101].

eter or an external beam-stop. Both of these changes reduce the background within the chamber. However, the Orsay Enge spectrometer and the Munich Q3D cannot run with external beam-stops or in a 0° mode. In this case, shielding the silicon detectors from the Faraday cup is not required and silicon detectors can be placed at more forward angles, increasing the efficiency and thus the sensitivity. A number of spectrometers exist around the world that can operate at 0° , such as BACCHUS at Orsay, the K600 at iThemba [104] and the Grand Raiden spectrometer at RCNP Osaka [105]. ($^3\text{He},d$) reactions may limit the beam intensity which can be used with the spectrometer in a 0° mode. A test experiment would be required to ascertain what the maximum beam intensity usable in this case would be. A proposal to this effect has recently been submitted to iThemba by the author and collaborators.

In summary, from the data analysed on this experiment, it appears promising that a $^{19}\text{F}(^3\text{He},t)^{19}\text{Ne}(\alpha)^{15}\text{O}$ experiment which is able to measure accurate α -branching ratios for states in ^{19}Ne is possible. Uncertainty remains over whether the background will be higher in the lower energy region of the silicon detector spectrum where the reactions α -particles will fall, and whether the background from the ^3He beam significantly differs from that produced by the proton beam.

Chapter 10

Conclusions

Ceterum censeo Carthaginem esse delendam.

Furthermore, I consider that Carthage must be destroyed.

Cato the Elder

In this thesis, three test experiments which help to guide on-going efforts to determine the $^{15}\text{O}(\alpha,\gamma)^{19}\text{Ne}$ reaction rate have been described. Potential plans for future study using these reactions is therefore intrinsic to the discussion of the results from the test reactions and discussed simultaneously to final conclusions.

The first test assists with planning a future measurement of the $^{15}\text{O}(^6\text{Li},d)^{19}\text{Ne}$ reaction from which the Γ_α of the 4033-keV resonances (and 4140- and 4197-keV resonances) can be determined. This experiment will use a radioactive ^{15}O beam at TRIUMF-ISAC in inverse kinematics with the reaction deuterons being detected in SHARC whilst the coincident γ rays resulting from the decay of the states will be detected in TIGRESS.

From the test measurement and the analysis of the resulting data, the author has:

- Confirmed that the new data acquisition event fragment readout mode functions correctly, and that usable data result from the reconstruction. This will enable the experiment to run with the higher data rates that will result from the $^{15}\text{O}(^6\text{Li},d)^{19}\text{Ne}$ experiment.
- Uncovered a serious flaw in the timing algorithm for the data acquisition system which has resulted in a leading-edge system being implemented in the data acquisition system whilst the constant-fraction system is corrected.
- Uncovered a flaw in the preamplifier design which has now been corrected.
- Developed a number of algorithms to aid with the analysis of SHARC/TIGRESS data. The algorithms can perform thickness corrections to separate $dE - E$ loci in silicon detectors, calculate reaction angles and perform Doppler corrections on

detected γ rays on the basis of the detected charged particles. These algorithms are available for use with all modes of SHARC.

- Determined that the number of particles from compound nucleus reactions off fluorine in the target will create a high background for the $({}^6\text{Li},d)$ reaction which may make identification of reaction deuterons difficult. Therefore, the experiment has been redesigned to include a silicon detector downstream of SHARC which will be used to detect the ${}^{19}\text{Ne}$ recoil at small angles to reject background from fusion evaporation reactions.

In light of the knowledge gained from this test, it is now thought that the ${}^{15}\text{O}$ experiment can be carried out.

A second test has provided information on the problems likely to occur in a planned measurement of the J^π of states in ${}^{19}\text{Ne}$ via the ${}^{20}\text{Ne}(d,t){}^{19}\text{Ne}$ reaction using neon-implanted carbon foils. Using the angular distributions of outgoing tritons from resonances just above the α threshold, the ℓ -values of the reaction can be determined, which can resolve which resonance is $\frac{7}{2}^-$ and which is $\frac{9}{2}^-$. A key concern is the effect of unfocussed peaks obscuring certain angle and excitation energies at different angles due to reactions from target contaminants.

The test shows that the states of interest are obscured over a large angular range. The limited range of angles over which an angular distribution may be obtained makes identification of the spins of the states functionally impossible. If this approach is to be used, then a different foil for implantation will be required. This also raises the question of whether the neon implantation will be stable in the host foil under high beam intensities.

A third test experiment suggests that a measurement of the α -particle branching ratio for states in ${}^{19}\text{Ne}$ may be possible by measuring the ${}^{19}\text{F}({}^3\text{He},t){}^{19}\text{Ne}^*(\alpha){}^{15}\text{O}$ reaction using the Orsay Enge magnetic spectrometer with silicon detectors in the reaction chamber. Careful choice of silicon detectors used may help to reduce the uncertainties due to background in the detectors. If background within the reaction chamber remain problematic, a different magnetic spectrometer with a larger acceptance and an external beam-stop would have significantly lower background in silicon detectors and would allow for a higher α -detection efficiency.

Appendix A

Evaluation of the Gamow Factor integral

Evaluating eq. (2.21) is somewhat complex and, for completeness, the mechanics of moving from that equation to eq. (2.22) are set out here. The details are taken from Ref. [15].

The following equation must be solved, with terms as defined previously:

$$\Theta_{total} = \exp \left(-\frac{2}{\hbar} \int_R^{R_c} \sqrt{2m(V(r) - E)} dr \right) . \quad (\text{A.1})$$

From the previous definition of R_c , $E = \frac{1}{4\pi\epsilon_0} \frac{Z_1 Z_2 e^2}{R_c}$. Using this definition, and that $V(r) = \frac{1}{4\pi\epsilon_0} \frac{Z_1 Z_2 e^2}{r}$, the exponent in the above equation can be written as:

$$I = -\frac{2}{\hbar} \int_R^{R_c} \sqrt{2m(V(r) - E)} dr = -\frac{2}{\hbar} \frac{1}{4\pi\epsilon_0} \sqrt{2m Z_1 Z_2 e^2} \int_{R_0}^{R_c} \sqrt{\frac{1}{r} - \frac{1}{R_c}} dr . \quad (\text{A.2})$$

Using integration by substitution, with $z = \frac{r}{R_c}$, this becomes:

$$I = -\frac{2}{\hbar} \sqrt{\frac{2m}{E}} \frac{1}{4\pi\epsilon_0} Z_1 Z_2 e^2 \int_{R_0/R_c}^1 \sqrt{\frac{1}{z} - 1} dz \quad (\text{A.3})$$

which, being evaluated, is:

$$I = -\frac{2}{\hbar} \sqrt{\frac{2m}{E}} \frac{1}{4\pi\epsilon_0} Z_1 Z_2 e^2 \left(\arccos \sqrt{\frac{E}{V_B}} - \sqrt{\frac{E}{V_B} \left(1 - \frac{E}{V_B}\right)} \right) . \quad (\text{A.4})$$

In most astrophysical scenarios, the energy of the colliding particles is much lower than the Coulomb barrier height ($E \ll V_B$), meaning that eq. (A.4) can be approximated as $\frac{\pi}{2}$, to zeroth order in $\frac{E}{V_B}$. Therefore,

$$I \approx -\frac{2\pi}{\hbar} \sqrt{\frac{m}{2E}} \frac{1}{4\pi\epsilon_0} Z_1 Z_2 e^2 \quad (\text{A.5})$$

as was required.

Appendix B

The Orsay system efficiency

There are two main parts to the efficiency calculations: sampling the emission angles with a certain distribution and finding whether the emitted particle hits one of the silicon detectors.

Inelastic proton scattering at 40° to states around 13.5 MeV in excitation in ^{27}Al leaves the recoil with an energy of around 340 keV and going at 24° relative to the beam direction. For the purposes of these calculations, these values are used for all reactions; this does not modify the efficiency calculated significantly.

B.1 Angular distribution of reaction products

For a decay of a certain angular momentum value, ℓ , the probability angular distribution of products is given by $\Xi(\theta)d\theta \propto |P_\ell(\cos\theta)|^2 \sin\theta d\theta$, where the $P_\ell(\cos\theta)$ are the Legendre polynomials of order ℓ . Using the orthogonality condition for Legendre polynomials,

$$\int_{-1}^1 P_\ell(x)P_{\ell'}(x) dx = \frac{2}{2\ell+1}\delta_{\ell\ell'}, \quad (\text{B.1})$$

where $x = \cos\theta$, and the condition that the total probability of emission over all angles is 1:¹

$$\int_0^\pi \Xi(\theta)d\theta = 1 \quad (\text{B.2})$$

from which the normalisation for the probability angular distribution can be found to be $\frac{2\ell+1}{2}$.

If $\Xi(\theta)d\theta = \frac{2\ell+1}{2}|P_\ell(\cos\theta)|^2 \sin\theta d\theta$ is the probability distribution, the matter of sampling a uniform distribution in order to get a distribution of this form must now be performed. This is a well-known problem in which inverse transform sampling is used.

¹In this section, the integration over the uniformly distributed ϕ has been omitted to aid clarity.

The cumulative distribution function,

$$F_{\Theta}(\theta) = \int_{\theta'=0}^{\theta} \Xi(\theta') d\theta' \quad (\text{B.3})$$

gives a uniformly distributed variable $Y = F_{\Theta}(\theta)$ [106]. Therefore, if Y is uniformly distributed in the interval $[0,1]$, (which it must be if it is a cumulative distribution function) then the inverse transform of the variable Y gives F_{Θ} [106], i.e.:

$$\theta = F_{\Theta}^{-1}(Y) \quad (\text{B.4})$$

is distributed according to the cumulative distribution function F_{Θ} .

In order to get this distribution, the cumulative distribution function and its inverse must be computed, then the variable Y is randomly sampled from a uniform distribution in $[0,1]$ and the value converted back to θ . For $\ell = 0$, $P_0(\cos\theta) = 1$ and so $\Xi(\theta)d\theta = \frac{1}{2} \sin\theta d\theta$. Using this in eq. (B.3), $F_{\Theta}(\theta) = \frac{1}{2}(1 - \cos\theta)$; the inverse transform is then $F_{\Theta}^{-1}(Y) = \arccos(1 - 2Y)$, giving a random sample of angles following the correct distribution.

For higher ℓ -values, the same analysis can be performed to randomly sample across the correct probability distribution.

B.2 Reaction products and impact on silicon detectors

In order to determine whether a proton or α particle hits the silicon detector, some vector algebra is required. The momentum of the emitted particle in the laboratory frame is calculated by considering the centre-of-mass emission vector and converting to the laboratory frame. A unit vector, \underline{s} , for the direction of the particle can then be computed.

Planes are represented in vectorial form as those values of \underline{r} that satisfy:²

$$\underline{n} \cdot (\underline{r} - \underline{r}_0) = 0 \quad (\text{B.5})$$

where \underline{n} is a unit normal vector to the plane, \underline{r} is a position vector from the origin to the point being considered, and \underline{r}_0 is a point on the plane. The position vector \underline{r} is some multiple of the unit direction vector \underline{s} , eq. (B.5) becomes the requirement that a solution to the equation $\underline{n} \cdot (\xi \underline{s} - \underline{r}_0) = 0$ is found for ξ ,³ the scaling factor from $\underline{r} = \xi \underline{s}$. Or, equivalently:

$$\xi = \frac{\underline{n} \cdot \underline{r}_0}{\underline{n} \cdot \underline{s}} \quad (\text{B.6})$$

²The author is indebted to Mr. James Smallcombe for noting that the problem could be treated as a infinite planar system in this manner

³Practically, this requirement becomes $\underline{n} \cdot (\xi \underline{s} - \underline{r}_0) < 10^{-8}$ to account for numerical effects in the computation.

This allows the position where the particle crosses the infinite plane of the detector⁴ to be found. Note that negative values of ξ correspond to the particle going away from the detector, these will obviously never hit the detector and can thus be discounted..

With the position where the particle crosses the plane of the detector, it is simple to consider whether this point falls within the physical finite plane of the detector and to compute which strip is hit by using $\underline{r} - \underline{r}_0$.

⁴I.e. the detector is part of an infinite plane that extends to infinity in all directions.

Bibliography

- [1] E. M. Basinska *et al.*, *Astrophysical Journal* **241**, 787 (1980).
- [2] J. Grindlay *et al.*, *Astrophysical Journal* **205**, L127 (1976).
- [3] R. Belian, J. Conner, and W. Evans, *Astrophysical Journal* **206**, L135 (1976).
- [4] S. Woosley and R. Taam, *Nature* **263**, 101 (1976).
- [5] N. Weinberg, L. Bildsten, and H. Schatz, *Astrophysical Journal* **639**, 1018 (2006).
- [6] F. Ajzenberg-Selove, *Nuclear Physics A* **523**, 1 (1991).
- [7] F. Hoyle, D. Dunbar, W. Wenzel, and W. Whaling, *Physical Review* **92**, 1095 (1953).
- [8] E. Salpeter, *Astrophysical Journal* **115**, 326 (1952).
- [9] D. N. F. Dunbar, R. E. Pixley, W. A. Wenzel, and W. Whaling, *Phys. Rev.* **92**, 649 (1953).
- [10] C. W. Cook, W. A. Fowler, C. C. Lauritsen, and T. Lauritsen, *Phys. Rev.* **107**, 508 (1957).
- [11] M. Freer *et al.*, *Physical Review C* **86**, 034320 (2012).
- [12] W. R. Zimmerman *et al.*, *Physical Review Letters* **110**, 152502 (2013).
- [13] H. Fynbo *et al.*, *Nature* **433**, 136 (2005).
- [14] S. Chandrasekhar, *Philosophical Magazine* **11**, 592 (1931).
- [15] C. Iliadis, *Nuclear Physics of Stars* (Wiley-VCH, Weinheim, Germany, 2007).
- [16] D. Tilley, H. Weller, and C. Cheves, *Nuclear Physics A* **564**, 1 (1993).
- [17] F. Ajzenberg-Selove, *Nuclear Physics A* **392**, 1 (1983).
- [18] P. J. C. Salter *et al.*, *Physical Review Letters* **108**, 242701 (2012).

- [19] J. L. Fisker, F.-K. Thielemann, and M. Wiescher, *The Astrophysical Journal Letters* **608**, L61 (2004).
- [20] J. L. Fisker, H. Schatz, and F.-K. Thielemann, *The Astrophysical Journal Supplement Series* **174**, 261 (2008).
- [21] C. M. Deibel *et al.*, *Physical Review C* **84**, (2011).
- [22] H. Schatz *et al.*, *Physical Review Letters* **86**, 3471 (2001).
- [23] V.-V. Elomaa *et al.*, *Physical Review Letters* **102**, 252501 (2009).
- [24] D. K. Galloway *et al.*, *The Astrophysical Journal Supplement Series* **179**, 360 (2008).
- [25] A. M. Levine *et al.*, *The Astrophysical Journal Letters* **469**, L33 (1996).
- [26] D. E. Gruber *et al.*, *Astronomy and Astrophysics Supplement* **120**, C641 (1996).
- [27] K. Jahoda *et al.*, *Proc. SPIE* **2808**, 59 (1996).
- [28] M. E. Bennett *et al.*, *Monthly Notices of the Royal Astronomical Society* **420**, 3047 (2012).
- [29] J. L. Fisker, J. Gorres, M. Wiescher, and B. Davids, *The Astrophysical Journal* **650**, 332 (2006).
- [30] J. L. Fisker *et al.*, *The Astrophysical Journal* **665**, 637 (2007).
- [31] W. P. Tan *et al.*, *Physical Review Letters* **98**, 242503 (2007).
- [32] B. Davids, R. H. Cyburt, J. Jose, and S. Mythili, *Astrophysical Journal* **735**, (2011).
- [33] M. H. Macfarlane and J. B. French, *Rev. Mod. Phys.* **32**, 567 (1960).
- [34] J. Schiffer, *Nuclear Physics* **46**, 246 (1963).
- [35] C. Iliadis, *Nuclear Physics A* **618**, 166 (1997).
- [36] J. Taylor, *Scattering Theory: The Quantum Theory of Nonrelativistic Collisions*, *Dover Books on Engineering Series* (Dover, Mineola, New York, 2006).
- [37] J. P. Schiffer *et al.*, *Physical Review C* **87**, 034306 (2013).
- [38] K. Krane and D. Halliday, *Introductory nuclear physics* (Wiley, Hoboken, New Jersey, 1987).
- [39] I. Naqib and L. Green, *Nuclear Physics A* **112**, 76 (1968).

- [40] I. Thompson and F. Nunes, *Nuclear Reactions for Astrophysics: Principles, Calculation and Applications of Low-Energy Reactions* (Cambridge University Press, Cambridge, UK, 2009).
- [41] D. Tilley, H. Weller, C. Cheves, and R. Chasteler, *Nuclear Physics A* **595**, 1 (1995).
- [42] H. T. Fortune, H. Nann, and B. H. Wildenthal, *Physical Review C* **18**, 1563 (1978).
- [43] R. Middleton, *Report on some lithium reaction studies in Nuclear reactions induced by heavy ions: Proceedings of the International Conference on Nuclear Reactions Induced by Heavy Ions, Heidelberg, 15-18 July 1969* (North-Holland Pub. Co., ADDRESS, 1970).
- [44] K. Kubo, F. Nemoto, and H. Bando, *Nuclear Physics A* **224**, 573 (1974).
- [45] Z. Q. Mao, H. T. Fortune, and A. G. Lacaze, *Physical Review C* **53**, 1197 (1996).
- [46] K. E. Rehm *et al.*, *Phys. Rev. C* **67**, 065809 (2003).
- [47] W. Tan *et al.*, *Physical Review C* **72**, (2005).
- [48] R. Kanungo *et al.*, *Physical Review C* **74**, 045803 (2006).
- [49] S. Mythili *et al.*, *Physical Review C* **77**, 035803 (2008).
- [50] J. D. Garrett, H. G. Bingham, H. T. Fortune, and R. Middleton, *Physical Review C* **5**, 682 (1972).
- [51] F. de Oliveira *et al.*, *Physical Review C* **55**, 3149 (1997).
- [52] Z. Q. Mao, H. T. Fortune, and A. G. Lacaze, *Physical Review Letters* **74**, 3760 (1995).
- [53] P. Magnus *et al.*, *Nuclear Physics A* **506**, 332 (1990).
- [54] D. W. Visser *et al.*, *Phys. Rev. C* **69**, 048801 (2004).
- [55] A. M. Laird *et al.*, *Phys. Rev. C* **66**, 048801 (2002).
- [56] B. Davids *et al.*, *Phys. Rev. C* **67**, 065808 (2003).
- [57] B. Davids *et al.*, *Phys. Rev. C* **67**, 012801 (2003).
- [58] W. P. Tan *et al.*, *Physical Review C* **79**, (2009).
- [59] [http://www.triumf.info/wiki/exp-prog/index.php/ISAC_\(Isotope_Separator_and_ACcelerator\)](http://www.triumf.info/wiki/exp-prog/index.php/ISAC_(Isotope_Separator_and_ACcelerator)), TRIUMF information wiki.

- [60] http://www.triumf.info/wiki/exp-prog/img_auth.php/thumb/6/6a/Test-isacii-06segment.jpg/600px-Test-isacii-06segment.jpg, picture from the TRIUMF information wiki.
- [61] R. Stokes and T. Wangler, *Annual Review of Nuclear and Particle Science* **38**, 97 (1988).
- [62] G. Knoll, *Radiation Detection and Measurement* (John Wiley & Sons, Hoboken, New Jersey, 2010).
- [63] 2012 Catalogue - Micron Semiconductor Limited, 2012, Available from the Micron Semiconductor Limited.
- [64] C. Aa. Diget *et al.*, *Journal of Instrumentation* **6**, P02005 (2011).
- [65] G. L. Wilson, Ph.D. thesis, University of Surrey, 2013.
- [66] XCOM: Photon Cross Sections Database, <http://www.nist.gov/pml/data/xcom/index.cfm>, Accessed on 1st of January 2013.
- [67] H. Scraggs *et al.*, *Nuclear Instruments and Methods in Physics Research Section A: Accelerators, Spectrometers, Detectors and Associated Equipment* **543**, 431 (2005).
- [68] C. Svensson *et al.*, *Nuclear Instruments and Methods in Physics Research Section A: Accelerators, Spectrometers, Detectors and Associated Equipment* **540**, 348 (2005).
- [69] M. Schumaker *et al.*, *Nuclear Instruments and Methods in Physics Research Section A: Accelerators, Spectrometers, Detectors and Associated Equipment* **573**, 157 (2007), *Proceedings of the 7th International Conference on Position-Sensitive Detectors*.
- [70] J. P. Martin *et al.*, *IEEE Transactions on Nuclear Science* **55**, 84 (2008), 15th IEEE/NPSS Real-Time Conference 2007, Batavia, IL, APR 29-MAY 04, 2007.
- [71] Private communication, S. J. Williams.
- [72] http://www.triumf.info/wiki/tigwiki/index.php/TIGRESS_Event_Bank_Format, Accessed on 5th of February 2013.
- [73] TigSortGUI analyser, <http://trshare.triumf.ca/~ulrike/tigress-tigsort.php>, Accessed on 31st of December 2012.

- [74] Private communication from Tom Davinson as part of thesis corrections.
- [75] M. Schumaker and C. Svensson, Nuclear Instruments and Methods in Physics Research Section A: Accelerators, Spectrometers, Detectors and Associated Equipment **575**, 421 (2007).
- [76] J. R. Brown, Ph.D. thesis, University of York, 2009.
- [77] Decay radiation for ^{244}Cm , <http://www.nndc.bnl.gov/chart/decaysearchdirect.jsp?nuc=244CM&unc=nds>, Accessed on 31st of December 2012.
- [78] Decay radiation for ^{241}Am , <http://www.nndc.bnl.gov/chart/decaysearchdirect.jsp?nuc=241AM&unc=nds>, Accessed on 31st of December 2012.
- [79] Decay radiation for ^{239}Pu , <http://www.nndc.bnl.gov/chart/decaysearchdirect.jsp?nuc=239Pu&unc=nds>, Accessed on 31st of December 2012.
- [80] Micron Semiconductor Limited, BB11 Type 7G (Front and Rear), 2012, taken from a technical drawing of BB11 PCBs.
- [81] Private communication, G. Hackman.
- [82] O. Tarasov and D. Bazin, Nuclear Instruments and Methods in Physics Research Section B: Beam Interactions with Materials and Atoms **204**, 174 (2003), 14th International Conference on Electromagnetic Isotope Separators and Techniques Related to their Applications.
- [83] V. Bildstein *et al.*, The European Physical Journal A **48**, 1 (2012).
- [84] B. Davids and C. N. Davids, Nuclear Instruments and Methods in Physics Research Section A: Accelerators, Spectrometers, Detectors and Associated Equipment **544**, 565 (2005).
- [85] Private communication, C. Aa. Diget.
- [86] C. Wiedner *et al.*, Nuclear Instruments and Methods **105**, 205 (1972).
- [87] M. Löffler, H. Scheerer, and H. Vonach, Nuclear Instruments and Methods **111**, 1 (1973).
- [88] H.-F. Wirth *et al.*, Private Communication, H.-F. Wirth, paper in preparation.
- [89] Private communication, B. P. Kay.

- [90] Private communication, C. T. Tsangu.
- [91] A. Dudek and D. Edens, *Physics Letters B* **B 36**, 309 (1971).
- [92] F. X. Timmes, R. Diehl, and D. H. Hartmann, *The Astrophysical Journal* **479**, 760 (1997).
- [93] G. Wasserburg, M. Busso, R. Gallino, and K. Nollett, *Nuclear Physics A* **777**, 5 (2006), [je:title;Special Issue on Nuclear Astrophysics;ce:title;.](#)
- [94] C. Iliadis, A. Champagne, A. Chieffi, and M. Limongi, *The Astrophysical Journal Supplement Series* **193**, 16 (2011).
- [95] Private communication, N. de Sereville.
- [96] H. A. Enge, *Nuclear Instruments and Methods* **162**, 161 (1979).
- [97] H. A. Enge, *Nuclear Instruments and Methods* **162**, 161 (1979).
- [98] Private communication, I. Stefan.
- [99] Stopping-Power and Range Tables for Helium Ions,
<http://physics.nist.gov/PhysRefData/Star/Text/ASTAR.html>, Accessed on 16th of July 2013.
- [100] F. Becchetti *et al.*, *Nuclear Instruments and Methods in Physics Research Section A: Accelerators, Spectrometers, Detectors and Associated Equipment* **505**, 377 (2003), Proceedings of the tenth Symposium on Radiation Measurements and Applications.
- [101] Private communication, A. Parikh.
- [102] A. Parikh *et al.*, *Phys. Rev. C* **83**, 045806 (2011).
- [103] A. M. Laird *et al.*, *Phys. Rev. Lett.* **110**, 032502 (2013).
- [104] R. Neveling *et al.*, *Nuclear Instruments and Methods in Physics Research Section A: Accelerators, Spectrometers, Detectors and Associated Equipment* **654**, 29 (2011).
- [105] M. Fujiwara *et al.*, *Nuclear Instruments and Methods in Physics Research Section A: Accelerators, Spectrometers, Detectors and Associated Equipment* **422**, 484 (1999).
- [106] L. Devroye, *Non-Uniform Random Variate Generation* (Springer-Verlag, New York, ADDRESS, 1986), this book can be downloaded from:
<http://luc.devroye.org/rnbookindex.html>.